UNIVERSITÀ DI PARMA

UNIVERSITA' DEGLI STUDI DI PARMA

DOTTORATO DI RICERCA IN

Scienze Chimiche

CICLO XXXI

Thriving metallacrowns, from the structural description in solution to the assembly of porous materials

Coordinatore,

Chiar.mo Prof. Roberto Corradini

Tutore,

Chiar.mo Dot. Matteo Tegoni

Co-tutore,

Chiar.mo Prof.: Luciano Marchiò

Dottoranda, Vittoria Marzaroli

Anni 2015/2019

The chief enemy of creativity is good sense

Pablo Picasso

"Success is not final,

failure is not fatal.

It is the courage to continue, that counts."

Winston Churchill

"It is the quality of ones convictions, that determine success,

not the number of followers."

R. Lupin,
J. K. Rowling

To my friends,

all of them.

Preface

"Water, water, everywhere,

and all the boards did shrink;

water, water, everywhere,

nor any drop to drink."

T. Coleridge

...except it was pyridine.

The project, from which arises the present dissertation, relates to three years of PhD, being entitled "*Metallacrown-based innovative materials and supramolecular devices*". The aim of the research was to isolate three-dimensional networks, possibly permanently porous, containing functional metallacrowns (MCs) as nodes. Among the variety of chemical-physical properties, very promising in terms of the possible applications are those metallacrowns that show luminescent brightness and single-molecule magnetic behavior. These properties are desirable to be incorporated into porous materials, since may lead to magnetic and luminescent probes, which can find application especially as sensors and in the field of bioimaging.

An extensive investigation of the state of the art, for what concern the principles of crystal engineering, molecular design and the metal organic frameworks synthetic approaches, have been carried out, allowing to lighten the landscape of possible procedures, brighten those that seemed more promising, and sometimes even giving rise to novel strategies, having the purpose to create multidimensional assembly of metallacrowns.

Thus, metallacrowns were investigated as potential secondary building units (SBUs), which, if properly connected via organic linkers, would perhaps result in MOF-like architectures, containing potential voids.

Define a MC-based SBU, means refers to polymetallic clusters, that shows the inorganic motif characterizing metallacrown [*M-N-O*], instead of the organic sequence [*M-(O/N)-C*] typical of a traditional SBU.

Metallacrowns were discovered in 1989 by Professor V. L. Pecoraro and have been deeply investigated in the last two decades, thanks to the variety of structures achievable, the tunability of their properties, the wide pool of building blocks to choose from, a pinch of serendipity and of course the great input to the personal creativity which follows this huge number of variables to deal with.

Because the metallacrown scaffolds form by self-assembly in solution, the investigation of the structure in the solid state and of the strategies to achieve metallacrown based coordination polymers, was anticipated by that of the structure, behavior and features in solution.

Hence, in Chapter 2 is reported the ^{1}H NMR studies of two isostructural series of heterotrimetallic metallacrowns. The species that were investigated are the $Na^{I}Ln^{III}(OAc)_4[12\text{-}MC_{Mn(III),(O)H3Shi\text{-}3H}\text{-}4]$ series of complexes, where Ln stays for La, Pr, Nd, Sm, Eu, Gd, Tb, Dy, Ho, Er, Tm, Yb and Y, and the analogue $Na^{I}Ln^{III}(OBz)_4[12\text{-}MC_{Ga(III),(O)H3Shi\text{-}3H}\text{-}4]$ one, where Ln stays for Pr, Nd, Sm, Eu, Gd, Tb, Dy, Ho, Er, Tm, Yb, Lu and Y. In these metallacrowns the ring of the metallamacrocycle is made by four salicylhydroxamate ligands (Shi^{3-}) and four Mn^{III}/Ga^{III} ring metals. The Y and Lu derivatives were analyzed as diamagnetic references, while overall the other complexes show a remarkable paramagnetic behavior. Despite their paramagnetic nature due to the unpaired electrons of the lanthanides ions (and of the manganese(III) in case of the first series), well resolved and narrow resonances were found. The ^{1}H NMR investigation and the application of the "*all lanthanides*" calculations for the data treatment, allowed to correlate the structure in solution with that in the solid state confirming the stability upon dissolution of all the molecules and the isostructurality of the molecular structures in solution. Furthermore, the "*all lanthanides*" approach provided the values of the Fermi contact and pseudocontact paramagnetic contributions to the chemical shift and the possibility to unambiguously assign the resonances of the spectra.

Metallacrowns-based coordination polymers have finally been prepared. That was possible by choosing the appropriate starting building blocks (i.e. metal ions, ligands and linkers). Indeed, the design of the SBU was found as a crucial factor for obtaining the desired three-dimensional network of MCs. Different MC-shaped SBUs were investigated (i.e. plates, dimers, spheres, …). Among these,

only the sphere-like joint has been found capable to drive the self-assembly in solution, leading to the formation of three-dimensional coordination polymers with the MC topology.

The present work reports the most interesting results, that were found by combining manganese acetate with H_3*p*-RShi derivatives and different alkali-metal ions linkers. Among the five networks, that will be discussed in Chapter 3, the most promising is that obtained from the combination of manganese acetate with the new *p*-pyShi^{3-} ligand, which is the para-pyridyl derivative of the salicylhydroxamic acid. The resultant network is a three-dimensional MOF-like architecture, that shows channels in all the three crystallographic dimensions. The endless honeycomb-shaped channels give rise to potential voids, partially occupied by solvent molecules, which correspond to 55% of the unit cell.

The research, leading to these results, was carried out thanks to the collaboration of both Bachelor and Master students. Their names are: Clarissa Salviati, Giulia Fattori, Luca Sergi, Giuseppe Lococciolo, Rosy Polisicchio, Lucia Corti, Tommaso Nicolò Zani, Federica Cester, Alex Falco, Gisella Giorgetti and Davide Seletti. Moreover, the crystal structures of the $Na^{I}Ln^{III}$[12-$MC_{Mn(III),(O)H3Shi-3H}$-4] compounds (Chapter 2) were previously reported by our collaborator Prof. Curtis Zaleski from the Shippensburg University (M. R. Azar et al., Inorg. Chem. **2014**, *53*, 1729–1742), the ^{1}H NMR spectra of the $Na^{I}Ln^{III}$ [12-$MC_{Mn(III),(O)H3Shi-3H}$-4] series of compounds (Chapter 2) were collected by Corrado Atzeri, who anticipated some preliminary analysis in his PhD thesis. The Na-$Mn_{11}Shi_6$ cage (Chapter 3) was firstly isolated by Martina Quaretti and a preliminary purpose of discussion was anticipated by Corrado Atzeri in his PhD thesis. The H_3*p*-pyShi ligand (Chapter 3) was prepared by Giulia Spigolon, from the group of our collaborator Giulia Licini at the University of Padova. The

My personal contribution to the experimental data, which will be reported and discuss within the present dissertation includes:

- the definition of thestrategies and approaches to be followed;

- the optimization of the synthetic procedures for the preparation of the $Na^{I}Ln^{III}(OBz)_4$[12-$MC_{Ga(III),(O)H3Shi-3H}$-4] series of complexes (Chapter 2), the H_3*p*-aShi ligand (Chapter 3), and the five new coordination polymers (Chapter 3);
- the X-Ray data collection, solution and refinement of the new crystal structures;
- the collection of the 1H NMR data, their analysis and discussion.

The results related to the study of the ^{1}H NMR behaviour of the $Na^{I}Ln^{III}(OAc)_4$[12-$MC_{Mn(III),(O)H3Shi-3H}$-4] series of compounds (Chapter 2) gave rise to the article entitled: *"Elucidation of 1H NMR Paramagnetic Features of Heterotrimetallic Lanthanide(III)/Manganese(III) 12-MC-4 Complexes".* Ref.: Atzeri C, Marzaroli V, Quaretti M, Travis J. R., Di Bari L., Zaleski C. M. and Tegoni M. Inorg Chem. 2017;*56*(14):8257-8269.

The synthesis of the two new salicyhydroxamate derivatives, and three to the five new manganese three-dimensional networks, led to the article entitled *"Three-dimensional porous architectures based on $Mn^{II}/^{III}$ three-blades paddlewheel metallacryptates"*, prepared by Marzaroli V.; Spigolon G.; Lococciolo G., Quaretti M., Salviati C., Kampf J., Licini G., Marchio' L., Pecoraro V., and Tegoni M., and submitted to Crystal Growth and Design Journal, on 28 December 2018.

The remaining results will be published within articles, that are now under preparations.

The following coworkers must be acknowledged: Dr. Domenico Acquotti and Centro Interdipartimentale Misure "G. Casnati" (University of Parma), for the assistance in the collection of some of the NMR spectra; Dr. Jeff Kampf form the University of Michigan, the staff (in the person of Nicola Demitri) and the facilities of Elettra X-Ray Diffraction 1 (XRD1) beamline, for assistance in X-Ray data collection of some crystals, Dr. Beatrice Bonati, for the assistance in the ESI-MS data collections at the University of Parma.

Moreover, I am particularly grateful to Prof. Igor Fritsky, Prof. Vincent L. Pecoraro, Prof. Luciano Marchiò and Dr. Tegoni for precious advices, wise suggestions and useful teachings.

Finally the research leading to the results, collected over the three years of PhD program have received funding from Italian Ministry of Foreign Affairs and International Cooperation for financial support through a bilateral Italy-USA project and from the European Community's Seventh Framework Programme (FP7/2013-2017) under grant agreement n° 611488 (FP7 Marie Curie IRSES “Metallacrowns” project).

Index

Chapter 1

GENERAL INTRODUCTION

"Fatti non foste per viver come bruti,

ma per seguir virtute e canoscenza"

Dante Alighieri
Inferno

1.1 Metallacrowns

Metallacrowns (MCs) are an exceptional class of coordination compounds, that result from the self-assembly in solution of metal ions, bischelating organic ligands (e.g. hydroxamate) and organic linkers (e.g carboxylates). This class of inorganic compounds was discovered by Prof. Vincent L. Pecoraro in 1989, at the University of Michigan (Ann Arbor, MI, USA). One of the first metallacrown complexes that has been synthesized and characterized in his laboratory is the $Mn^{II}[12\text{-}MC_{MnIII,\ (O)H_3Shi\text{-}3H}\text{-}4]$ species, reported in Figure 1.1 X-Ray structure of the MnII[12-MCMnIII, $_{(O)H3Shi\text{-}3H\text{-}4}$] species: one of the first metallacrown complexes isolated by L. V- Pecoraro.[1]

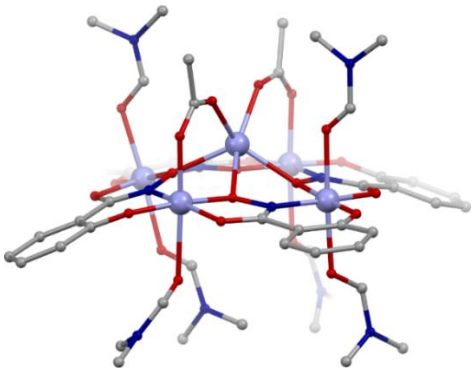

Figure 1.1 X-Ray structure of the $Mn^{II}[12\text{-}MC_{MnIII,\ (O)H3Shi\text{-}3H}\text{-}4]$ species: one of the first metallacrown complexes isolated by L. V- Pecoraro.[1] Colour code: Mn-light blue, O-red, N-blue, C-grey.

In the last thirty years a plethora of metallacrowns were discovered, isolated and characterized. Different architectures were found, and interesting chemical-physical properties were investigated. The large variability of structures and the tunability of the chemical-physical properties are a direct consequence of the high density of metal atoms, encapsulated in their small molecular volume. Moreover it is possible to choose within a wide variety of building blocks (i.e. metal ions, organic ligand and linkers), and wisely design

mono- and multi- functional system, which were investigated firstly as recognition agents (both for cations and anions),[2,3] then as building blocks for mesoporous solids [4,5] and more recently functional MCs are largely investigated as luminescent[6] or magnetic[7,8] probes in application for environmental sensing, bioimaging (e.g. as contrast agents)[9,10] and catalysis.[5,11]

1.1.1 General properties

Metallacrowns are generated using bischelating ligands (e.g. hydroxamate) and transition-metal ions that assemble in solution to give peculiar macrocyclic motifs. In MCs, the macrocycle is characterized by the repetition of the following sequence of atoms: M-N-O, which is a consequence of the metal ions coordination by preorganized ligands such as hydroxamates and oximes.

The metal ions, which form the scaffold are called *ring metals* and are usually from the first or second transition series. The oxygen donor atoms of the characteristic cycle in regular MCs point toward the inner cavity and enable the binding of additional cations, defined *core metals* (Figure 1.2).[12–15]

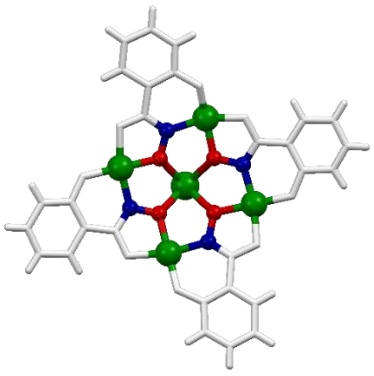

Figure 1.2 Structure of the Cu^{II}[12-$MC_{CuII,\ (O)H3Shi-3H}$-4] species. The characteristic scaffold of MCs is reported. The macrocyclic topology and the typical M-N-O structural motif are highlighted.[16] Colour code: Cu-green, O-red, N-blue, C-grey.

The central cavity, the size and the shape of the various scaffolds of MCs resembles that of crown ethers. This feature led to define MCs as the inorganic analogs of crown ethers and many studies were dedicated to the comparison of these two classes of macrocycles. Hence 12-MC-4, 15-MC-5 and 18-MC-6 are the metallacrowns analogs respectively of 12-crown-4, 15-crown-5 and 18-crown-6. The Figure 1.2 and the respective schematic representation reported in Figure 1.3 show how MCs may result by ideally substituting the C-C-O organic sequence typical for crown ethers, with the inorganic one typical for MCs (i.e. M-N-O).[1,17,18]

The inorganic nature and the typical set-up of MCs result in an exceptional metal-rich topology, which widely enlarge the possibilities in designing highly responsive MCs with peculiar chemical and physical properties.

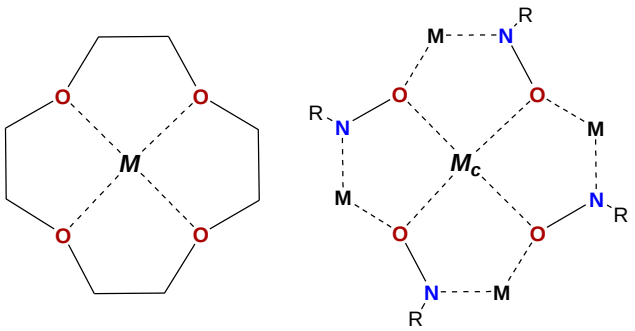

Figure 1.3 Left: structural motif of the organic 12-C-4 encapsulating the cation M within the cavity. **Right:** structural motif of a generic 12-MC-4 with the core metal (M_c) coordinated within the central cavity. The N and O heteroatoms are colored in blue and red respectively. R- indicate a generic organic ligand.

1.1.2 Nomenclature

Two nomenclatures for metallacrowns can be found over the literature: the first resembles that of crown ethers and is the one most commonly used. The second one is

usually found in thermodynamic studies for the description of self-assembly equilibria, speciation plots and host-guest reactivity. In the present dissertation the first nomenclature will be used. Its definition follows, by describing the $Cu^{II}[12MC_{CuII,(O)H3Shi-3H}-4]^{2-}$ formula referred to the species reported in Figure 1.2. Just as an example, the same complex would have been named as $\{Cu[Cu_4(L)_4]\}^{2-}$, by following the second notation. Hence, $Cu^{II}[12MC_{CuII,(O)H3Shi-3H}-4]^{2-}$is the inorganic analogue of the 12-crown-4 and the formula means that the cycle is formed by 12 atoms, four of which are oxygens donor atoms pointing toward the central cavity. The first metal ion is the core metal (M_c), while the ring metals (M_r) and the ligand (L) are subscript after the MC acronym.[1,14,19,20] The complete notation follows:

$$\{M_c(A')[R\text{-}MC_{Mr,(X)L}\text{-}Z]\}(A)\cdot xH_2O$$

where:

- R: number of atoms forming the macrocyclic ring;
- MC: metallacrown acronym;
- Z: number of oxygen atoms;
- M_c^{n+}: core metal and oxidation state superscript in Roman numeral;
- M_r^{n+}: ring metal and oxidation state superscript in Roman numeral;
- H_nL-mH: ligand and deprotonation grade (where, n is the number of acid protons and m are the deprotonated sites);
- X: heteroatom, that coordinates the ring metal outside the central cavity;
- A': counterions/water molecules coordinated to the scaffold;
- A: counterions/water molecules not coordinated to the scaffold.

1.1.3 The MCs building blocks

As anticipated at the beginning of paragraph 1.1, MCs form by self-assembly in solution of organic ligands and metal ions. Indeed, those are the two main building blocks necessary to prepare those metallamacrocycles, but a third component is commonly found and is reported in this dissertation as linker. The description of the building blocks, their features and their implications follow here after.

1.1.4 The hydroxamic ligands

If looking at Figure 1.3, the idea of preparing MCs by combining metal ions and hydrazine may arise. However, more elaborate ligands are necessary to simultaneously chelate two metal ions and to saturate their coordination spheres. Hence, functionalized hydroxamates and oximes are traditionally used for the preparation of MCs, thanks to their capability to coordinate two transition metals at the same time and to their pre-organized shape, which result in a template effect and helps the self-assembly in solution.

Metallacrowns formed by hydroxamic acids RC(O)N(OH)R', (R and R' as alkyl/aryl/H substituents and CO as a carbonyl group) are certainly the most investigated. This class of organic molecules are commonly obtained from the related carboxylic acids by condensation with hydroxylamine (Figure 1.4).[21–23]

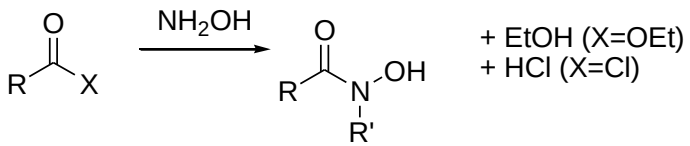

Figure 1.4 Scheme of the classical synthesis of hydroxamic acids

Hydroxamic acids are weak acids, deeply investigated over the literature, thanks to their attitude of forming stable complexes with transition metal ions. The coordination system is given by the two oxygen atoms and gives rise to a penta-coordination-ring (Figure 1.5, bottom).

Hydroxamic acids can be exploited for the preparation of metallacrowns by the introduction of a fourth coordinative function (X in Figure 1.5) in α, β, or γ position with respect to the carbon atom in α position to the hydroxamate function (Cα, Figure 1.5). This leads to the three α-, β-, and γ- hydroxamate classes of ligands. Overall these functionalized hydroxamates are bischelating ligands, indeed they are capable to coordinate a second metal ion by forming a second penta-, hexa- or hepta- chelation ring respectively for α-, β-, and γ- hydroxamates. (Figure 1.5) This feature is in charge of the X heteroatom shown in Figure 1.5, which can be both a nitrogen or an oxygen atom, leading respectively to a (N,N) or (N,O) chelation ring.[19,24]

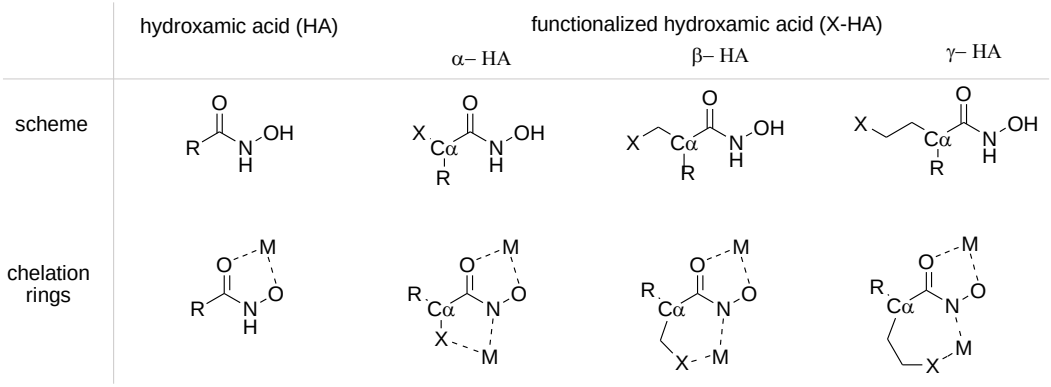

Figure 1.5 Top: structures of a generic hydroxamic acid (HA) and of the three functionalization ways (X-HA), which give rise to the three classes of hydroxamic ligands capable to form metallacrowns. Bottom: chelation rings resulting from the coordination of one (HA) or two (X-HA) metal ions; overall the hydroxamate conjugate base side form a first (O,O) chelation ring on the hydroxamic side and a second (N,X) chelation while on the X functionalized side.

When hydroxamates form metallacrowns the carboxylic oxygen points toward the central cavity, while the second chelation ring allows the formation of the cyclic scaffold (further details will be provided in paragraph 1.1.6).

1.1.5 The linkers

Additional organic molecules are usually found coordinated at the axial positions of both the core and the ring metals (both above or below with respect of the macrocyclic plane). These molecules can be solvents or counterions, but more interesting is to exploit this feature for the construction of dimers, chains, layers, extended architectures and solids, having MCs as joints. Those organic compounds capable to connect metallacrowns will be here named linkers. Hence, both ligands and linkers are organic molecules, with coordinative functions, but if the first class of compounds are in charge on the formation of the MC-macrocycle, the second one decorates it and possibly acts as joint, connecting two or more MCs units. In Figure 1.6 two examples of occupied axial positions are reported. The structure on the left shows two nitrates counterions coordinated to the lanthanides core metal and water molecules coordinated to the ring metals. On the right a dimeric structure is reported: here, two 12-MC-4 rings are connected thanks to the presence of four isophthalate dicarboxylic linkers. The 12-MC-4 reported in Figure 1.1 is also an example of the presence of organic linkers decorating both the top and the bottom of the MC scaffold (i.e. two acetates carboxylates and DMF molecules). [6,25–27] Further details and examples will be provided in chapter 3.[21,26,28]

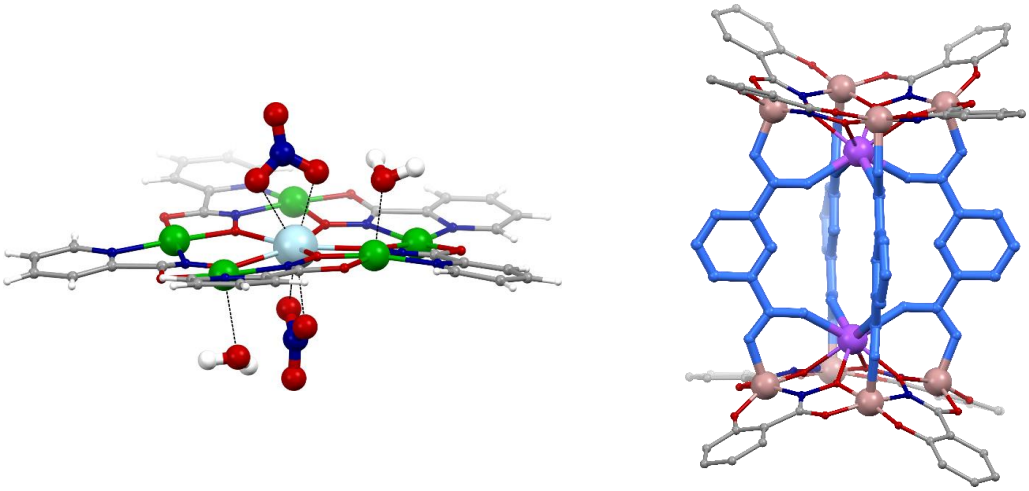

Figure 1.6 Left: $Nd^{III}[15\text{-}MC_{Cu^{II},(N)picHA}\text{-}5](NO_3)_3(H_2O)_2$ complex, where picHA is the picolinhydroxamate ligand.[25,29] The nitrates counterions and water molecules are coordinated both above and below the macrocycle, occupying axial positions of both ring (Cu^{II}) and core (Nd^{III}) metal ions. **Right:** $Dy_2[12\text{-}MC_{Ga^{III},(O)H3Shi\text{-}3H}\text{-}4]_2(Isoph)_4$ metallacrown, where shi^{3-} is the salicylhydroxamate ligand and Ipsoh is the Isophthalate linker.[26] This compound shows a dimeric architecture, where two 12-MC-4 rings are linked by four dicarboxilic linkers. Colour code: Ln-light green/purple, Cu-green, Ga-light pink, O-red, N-blue, C-grey.

1.1.6 The metallacrowns structural paradigm

The geometry of the metallacrown scaffold, which results from the self-assembly in solution of the overall building blocks can be predicted to some extent. As far as it concerns the scaffold, the final geometry can be predicted by considering the "*metallacrowns structural paradigm*", that explains how the geometry of the MC ring follows that of the chosen ligand. The Figure 1.7 shows an example of two different geometries, which follow the choice of the ligand. The second coordination ring in the case of α-hydroxamates is 5-membered, thus the resulting angle formed by the directions passing through the ring metals is about 108°, leading to the assembly of the pentagonal scaffold typical for the 15-MC-5 complexes.

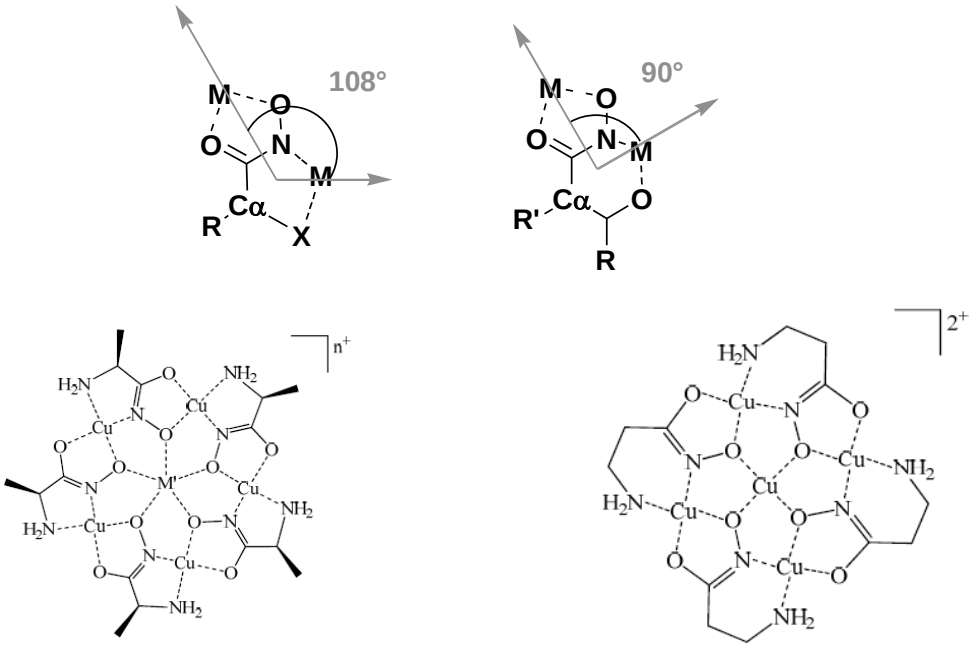

Figure 1.7 Top: Comparison of the α- (left) and β- (right) hydroxamate bischelating geometry, obtained by considering the hydroxamate ligand as a rigid block. The chelation angles are reported. Bottom: the M[15-MC$_{CuII\ (N)\alpha\text{-}alaHA\text{-}2H}$-5.] and the Cu^{II}[12-MC$_{CuII(N)\beta\text{-}alaHA\text{-}2H}$-4], examples of the different geometries, which follows the choice of the ligand.[19]

In case of β-hydroxamic acids, the second chelation ring is 6-membered, resulting in an angle of 90° degrees between the directions passing through the ring metals. This topology leads to the square shaped scaffolds, typical for the 12-MC-4 compounds. Hence, the larger the angle, the bigger the metallacrown, the larger the central cavity. Thus, 12-MC-4 scaffolds are capable to encapsulate in the central cavity transition metal atoms, while larger core metals like calcium or lanthanides can be coordinated only above the cavity, thanks to the presence of additional organic linkers (i.e. carboxylates), witch bridge a ring metal on one side and the core metal on the other one (Figure 1.8 Right).[27,30,31] The larger cavity of the 15-MC-5 complexes is capable to fit large ions, without additional linkers and, to the best of knowledge, no examples of small cation like copper(II) or zinc(II) has ever been found bound to the central cavity.(Figure 1.8 Left). [19]

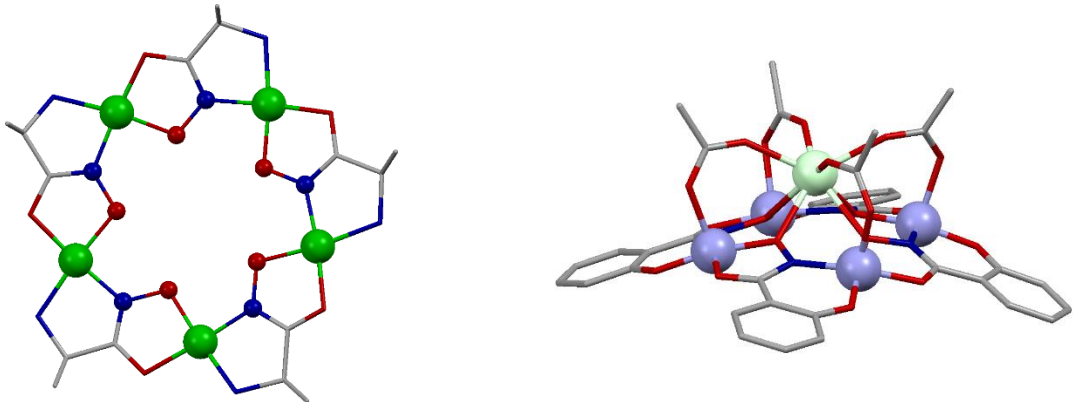

Figure 1.8 Structures of the pentagonal and square-shaped scaffolds of the 15-$MC_{CuII,\ (N)\alpha\text{-}alaHA\text{-}2H}$-5 (left) and Dy^{III}[12-$MC_{MnIII,\ (O)H3Shi\text{-}3H}$-4](OAc)$_4$ metallacrowns respectively.[27,31] Colour code: Cu-green, Mn-light blue, Dy-light green, O-red, N-blue, C-grey.

It is worth focusing on the salicylhydroxamic acid (H_3Shi) molecule. This compound belongs of the class of the β-hydroxamic acids: it derives from salicylic acid and it is one of the most investigated ligands for the synthesis of metallacrowns. Being a β-hydroxamate, the deprotonated form shi^{3-} was found capable to form 12-MC-4 with a huge number of metal ions (see paragraph 1.1.7) and its coordination mode is reported in Figure 1.9.

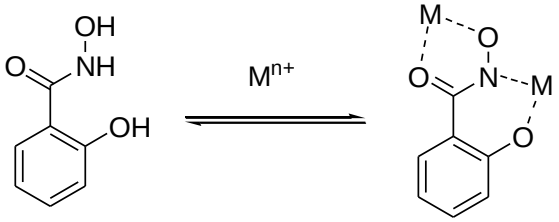

Figure 1.9 Coordination equilibrium of the salicylhydroxamic acid (H_3Shi) as ligand. The protonated form (H_3Shi) is reported on the left and the conjugated base (Shi^{3-}) set on the right coordinated to the M metal ion.

Either H_3Shi or its functionalized derivatives have been extensively used for the preparation of the metallacrowns discussed within the present dissertation.

1.1.7 Ring and core metal ions

As far as it concerns the choice of the metal ions, the ring metals (M_r) are usually transition metals from the first 3d series, while more variability is found for the core metal (M_c), which can be either from the transition metal series or from the alkali, alkali-earth or rare earth ones.

Both homo- and hetero- metallacrowns has been found, widening the possibility of choices and combinations. Also, both homogeneous and mixed valence metallacrowns can form. These features of metallacrowns are not only charming and enhancing the creativity of synthetic chemists, but also give access to a multitude of possible metal-dependent features and chemical-physical properties (e.g. luminescence and single molecule magnetism). An example of homo-metallic metallacrown and with homogeneous valence is provided by the Cu^{II}[12-$MC_{CuII,\ (O)H3Shi-3H}$-4], which has already been mentioned above and whose X-Ray structure is reported in Figure 1.10. The Mn^{II}[12-$MC_{MnIII,\ (O)H3Shi-3H}$-4]$(OAc)_2$ complex, reported in Figure 1.1, is an example of homo-metallic and mixed-valence metallacrown. Figure 1.6 provide an example of a hetero-metallic and homogeneous-valence metallacrown (i.e. the Dy_2[12-$MC_{GaIII,\ (O)H3Shi-3H}$-4]$_2$$(Isoph)_4$ spices on the right) and of a hetero-metallic and mixed-valence complex (i.e. the Nd^{III}[15-$MC_{CuII,(N)picHA}$-5]$(NO_3)_3(H_2O)_2$ spices on the left).

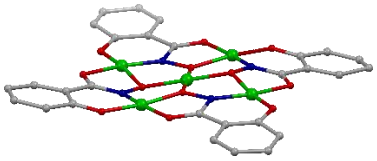

Figure 1.10 X-Ray structure of the homo-metallic Cu^{II}[12-$MC_{CuII,\ (O)H3Shi-3H}$-4] metallacrown.[16]

As described in chapter 1.1.6, the geometry of the final complex is determined by the choice of the ligand and linkers, while the metal ions have a minor influence. Indeed, the ionic radius, the charge and the preferential coordination geometries may tune the architecture of the final metallacrown, inducing distortions that may be significant and that depend by the chosen metal.

Two different M_c[12-$MC_{Mr,\ (O)H3Shi-3H}$-4] hetero-metallic complexes reported in literature can be considered as an example: the Dy^{III}[12-$MC_{GaIII,\ (O)H3Shi-3H}$-4]$(OBz)_4$ (**MC1**) and the Cu^{II}[12-$MC_{FeIII,\ (O)H3Shi-3H}$-4]Cl_2 (**MC2**), both reported in Figure 1.121. [1,6,8,16]

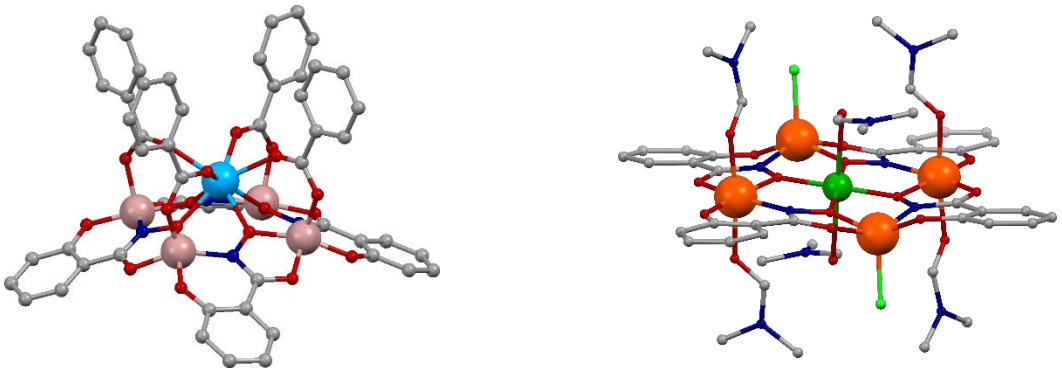

Figure 1.11 –Structures of the {Dy^{III}[12-$MC_{GaIII,\ (O)H3Shi-3H}$-4]$(OBz)_4$}$^{-1}$ (left)[6] and the Cu^{II}[12-$MC_{FeIII,\ (O)H3Shi-3H}$-4]Cl_2 (right).[8] Colour code: Cu-green, Ga-light pink, Ln-light blue, Fe-orange, Cl-light green, O-red, N-blue, C-grey.

The MC1 contains gallium(III) as M_r and a lanthanide ion as M_c, resulting in a domed architecture, where M_c is coordinated above the central cavity, and encapsulated thanks to four bridging benzoate linkers, that act also as counterions. Whereas the MC2 is formed by iron(III) as M_r and copper(II) as M_c, resulting in a pseudo planar scaffold.

1.1.8 The inverse metallacrowns (*inv*MC)

Beside the regular metallacrowns, back in 1995 Ann J. Stemmler, Jeff W. Kampf, and Vincent L. Pecoraro described the first *Inverse Metallacrown* (*inv*MC).[32] They purposed the idea that if a regular metallacrown is capable to recognise cation thanks to the oxygen rich central cavity, whose diameter is fixed and depend from the geometry of the scaffold, then it should have been possible to obtain the opposite as well. In other words, the presence of a cation-rich cavity, reached by inverting the classical connectivity of MCs, should result in a macrocycle capable to recognise anions by hosting them within the central cavity.

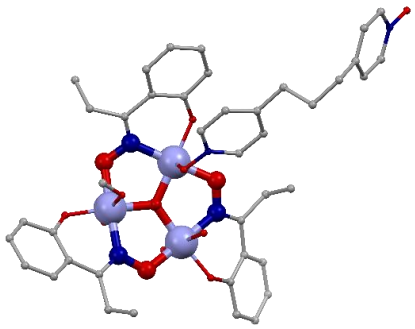

Figure 1.12 Structure of the 9-invMC-3 inverse metallacrown having formula ((μ$_3$-Oxo)-tris(μ$_2$-2-(N-oxypropanimidoyl)phenolato)-(μ$_2$-4,4'-propane-1,3-diylbis(pyridin-1-olato))(H$_2$O)$_3$(CH$_3$OH)Mn$_3$hemikis(N-(hydroxypropanimidoyl) phenolate) hemikis(NO$_3$)). Colour code: Mn-light blue, O-red, N-blue, C-grey.[33]

Literature shows that the preparation of *inv*MCs is straightforward, when the classical hydroxamate ligands are substituted by an oxime ligand and result in structures like the one reported in Figure 1.12. In this complex Mn^{III} cations, rather than oxygens point toward the central cavity and an oxide ion is encapsulated within it. *inv*MCs were investigated in the last two decades because of their interesting magnetic properties. Indeed, several manganese based 9-*inv*MC-3 were reported in the recent years showing peculiar single molecular magnetic features (SMM).[33–37]

1.2 Reticular Chemistry

The definition of "reticular chemistry" was purposed by Omar Yaghi in 2007, during his presentation for the *MRS Medal* in Boston. He defined "reticular chemistry" that chemistry, where all extended structures are composed entirely of joints and linkers, which correspond to vertices and edges of a net. The words of O. Yaghi are here reported:[38]

<< The meaning of the word reticular is "net-like". I define reticular chemistry as the chemistry concerned with the linking of molecular building blocks—these can be organic molecules, inorganic clusters, dendrimers, peptides, and proteins—into predetermined structures in which such units are repeated and are held together by strong bonds. The most brief definition is that reticular chemistry is "stitching molecules together by strong bonds">>.

In this respect reticular chemistry is a useful way to describe porous coordination networks, which are formed by the copolymerization of metal ions with organic linkers and result in extended solids with peculiar features. The last two decades saw an explosive increase in synthesis and characterization of such materials, that consist in frameworks, where building blocks are joined by covalent bonds. This class of coordination complexes resembles the *GEOMAG™* buildings, appearing as nets, which result from the interaction of discrete units (i.e. balls and spheres, which resembles respectively metal ions/ clusters and linkers, as shown in FIgure 1.13).[39–41]

One of the reasons that makes coordination networks so attractive is the ideally endless series of accessible new materials, that follows the possibility to select metal ions (joints) and organic linkers within a very wide range of atoms/molecules. Also, it is intriguing the

possibility to tune and to predict the structures, the features and the chemical-physical properties of the final materials. Indeed, coordination frameworks find applications in the most diverse sectors (e.g., gas storage/separation/sequestration, catalysis, sensing, magnetism, non-linear optics, drug delivery, biosensing, ...). [40]

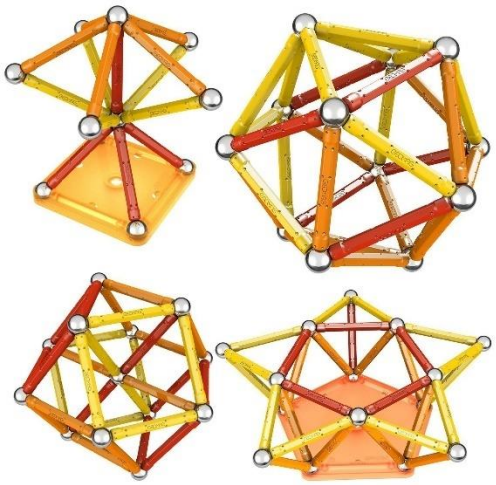

Figure 1.13 – Structures variability provided by the *GEOMAG*™ toys, which resembles the idea behind "reticular chemistry"

Within reticular chemistry different classes of coordination frameworks can be distinguished. The IUPAC Inorganic Chemistry Division, published in 2013 a set of terms, definitions, and recommendations , which consist in a guideline for the classification of coordination frameworks. The document focuses on three classes of compounds: (I) coordination polymers (CPs), (II) coordination networks, and (III) metal–organic frameworks (MOFs). We recall here some lines of that publication, highlighted here after by *Italic* style.

Within the recommendations the term coordination polymer refers to a *coordination compound with repeating coordination entities extending in 1, 2, or 3 dimensions.* IUPAC clarifies that such compounds *do not need to be crystalline*, can be sometimes *regarded as*

salts and that *the prefix 1D-, 2D-, or 3D- is acceptable for indicating the degree of extension of the coordination polymer*.

As for Metal Organic Frameworks, the document defines as MOF *a coordination network with organic ligands containing potential voids*. The term coordination network is not intended by IUPAC as a synonymous, but as a subset of coordination polymer. Indeed, a coordination network is intended a *coordination compound extending, through repeating coordination entities, in 1 dimension, but with cross-links between two or more individual chains, loops, or spiro-links, or a coordination compound extending through repeating coordination entities in 2 or 3 dimensions*. [37]

Following the 2013 IUPAC recommendations, MOFs seems differ from CPs mostly because of the presence of potential voids, but the line between these two terms is thin and not well defined nor within the IUPAC publication or by the general inorganic community.[37] Indeed, within the landscape of coordination arrays, many definitions of both CPs and MOFs have been reported over the years. These are sometimes incomplete, specific and even subjective. Also, while the first definition of CPs was reported by Shibata in 1916, such compounds were discovered much earlier, since the first synthesis of the Prussian blue type pigments in 1704. However, the real breakthrough within the field of coordination extended networks was the isolation of the MOF-5 in 1999 by Prof. O. Yaghi and co-workers: the MOF-5 shows a high thermal stability, robustness and a high surface area (2900 m^2g^{-1}), being unambiguously defined and accredited by the scientific community as the first real MOF.[38,41]

Indeed, the father of MOFs, Prof. Yaghi, provided in 2009 a widely detailed description of the features, which allow (in his opinion) to classify a material as a coordination polymer

or as a metal organic framework. To this purpose, Prof. Yaghi considered: (I) the energy associated with the M-N(O) bond in coordination networks compared to that of C-C in regular polymers, (II) the joint composition, (III) the overall charge of the chain, and (IV) the filling of the interstitial space. Hence, he suggested that: (I) the energy bond is close to that of coordination compounds in CPs, while more energetic (close to a covalent bond) in MOFs; (II) the joint is a single metal ion in case of CPs and a polymetallic cluster in case of MOFs; (III) CPs chains are usually charged, while MOFs are neutral; (IV) finally interstitial spaces are filled by counterions and solvent in case of CPs, while MOFs cavities can be completely evacuated. [41]

These guidelines will be used within the present dissertation (and in particular in Chapter 3), to classify the new synthetized materials.

In addition, back to MOF-5, Prof. Yaghi and co-workers were capable to isolate a series of isoreticular networks by maintaining the same joint of MOF-5 (which means the same Zn_4O cluster and dicarboxylic functions) and by changing the length of the carboxylate linkers. These experimental considerations gave rise to the concept known under the name of *Secondary Building Unit* (SBU).

SBUs are molecular complexes or polymetallic clusters in which the coordination modes of the ligand and the coordination environment of the metal can be exploited for the transformation of these fragments into extended porous networks by taking advantage of polytopic linkers. Overall the considerations upon the geometry and the chemical features of SBUs and linkers allow the researches to predict the framework topology and to design and synthesise new porous materials with robust structures and high porosity.

This SBU wording provides an organizing concept for the classification of MOF structures into their underlying topology. Thus, once classified the SBUs on the basis of their geometries and directionalities (i.e. the topology induced by each SBU), becomes easy to prepare MOFs and robust frameworks, whose structures and features are close to those predicted [41,42]

1.3 ^{1}H NMR characterization of paramagnetic compounds

Monodimensional ^{1}H-NMR is in general a very useful technique to characterize molecules in solution. Paramagnetic systems, though, show a peculiar NMR behaviour, leading NMR not to be always a suitable technique to their characterization in solution. The reason concerns the presence of unpaired electrons within paramagnetic systems. Indeed, the magnetic nucleus of a paramagnetic centre senses a magnetic moment, which arises from the electron motion on itself and across the space. Such magnetic moment is the result of both direct delocalization of unpaired electrons and spin polarization.[43–45] Hence, in case of paramagnetic metal complexes, the unpaired electrons enhance relaxation rates of those of the magnetic nuclei, that are surrounded by both d- and f- paramagnetic metal ions. As a result, the signals of the ^{1}H NMR spectrum show characteristic broadening, intensity reduction and a paramagnetic contribution to the chemical shift that markedly move the overall resonances from their diamagnetic position. For those reasons, the ^{1}H NMR is not a suitable technique for many paramagnetic compounds, however, lanthanides derivatives represent commonly an exception. Lanthanide ions, indeed, show a strong spin-orbit coupling of the *4f* electrons, leading to short electronic relaxation times, compared to the NMR times scale. This is reflected in a moderate "paramagnetic effect" induced by lanthanide ions, that commonly does not preclude high-resolution NMR for the characterization of the compounds of interest. Many examples are reported, over the literature, of Ln-based complexes characterized by ^{1}H NMR, whose spectra show deeply shifted but truly narrow proton signals.[46,47]

When the "paramagnetic effect" is due only to the presence of lanthanides ions, the chemical shift experienced by protons is commonly defined as Lanthanide Induced Shift (LIS_{Ln}). The LIS_{Ln} value is a result of two components: the Fermi contact shift and the pseudocontact shift.[46,47] The first, referred to as $\delta^{FC}(i)$, arises from the electrons density experienced by the i proton, when the unpaired electrons of the lanthanide ion are delocalized onto the nucleus being probed (i). Since this delocalization must occur through bonds, it is usually considered to be insignificant beyond four bonds. The pseudocontact shift ($\delta^{PC}(i)$) is the effect of the lanthanide unpaired electrons density interacting with the nucleus being probed (i) through space. This contribution to the shift is also reported as dipolar contribution and provides both structural and magnetic anisotropy information about the compound, being significantly dependent on physical variables correlated to these features.[48–52]

Beside moderate, the lanthanides "paramagnetic effect" markedly shifts the resonances and broaden the bandwidths, thus the interpretation of ^{1}H NMR spectra of lanthanides derivatives is not often straightforward. Nevertheless, understanding the ^{1}H NMR paramagnetic spectra, through an accurate assignment of the resonances, would provide very useful information about both the structure in solution of the complex and the magnetic anisotropy of the paramagnetic centres, giving a chance to finely characterize such compounds in solutions and correlate their features in solution to those in the solid state (when known).

1.3.1 Determination of the paramagnetic contribution to the chemical shift (δ^{para})

The chemical shift (δ^{obs}), that is observed, when the ^{1}H NMR spectrum of a paramagnetic species is collected, is made by the sum of a paramagnetic (δ^{para}) and a diamagnetic (δ^{dia}) contributions[43,44,53]:

$$\delta^{obs} = \delta^{dia} + \delta^{para} \quad (1.1)$$

When the unpaired electrons are that of a lanthanide ion, the observed chemical shift (δ^{obs}) becomes as given by the eqn. (1.2), since the lanthanide induced shift (LIS_{Ln}) was defined above as the paramagnetic contribution (δ^{para}) induced by a paramagnetic lanthanide ion.

$$\delta^{obs}_{Ln} = \delta^{dia} + LIS_{Ln} \quad (1.2)$$

For the determination of the value of the paramagnetic contribution to the observed chemical shift, the following conditions are necessary:

- the compound must belong to a series of at least one or more paramagnetic complexes plus a diamagnetic compound, that acts as reference;
- the overall complexes along the series must have the same geometrical and electronic structure;
- the structure must be characterized by axial symmetry, related to a C_n (n>3) axis.

The Ln-based paramagnetic series of isostructural complexes will be furthermore referred to as **Ln-C**. As for the diamagnetic reference, it is very common to take advantage of the Yttrium(III) analogue (Y-C). Indeed, beside the Yttrium(III) ion is not a lanthanide, its ionic radius and the chemical-physical properties of its derivatives are commonly close

to those of the isostructural Ln-C compounds. This consideration suggest that the diamagnetic behaviour of the Y-C should be the same experienced by the Ln-C.

When the conditions listed above are obeyed, the LIS_{Ln}(i) value is calculated for each i proton of the ^{1}H NMR spectrum, by following the eqn. 1.2 or the explicit version of eqn. 1.3.

$$LIS_{Ln}\ (i) = \delta^{obs}_{Ln} - \delta^{dia}_{Y} \qquad (1.3)$$

1.3.2 Detemrination of the Fermi contact (δ^{FC}) and pseudocontact (δ^{PC}) contribution to the LIS_{Ln}

As already mentioned above, the LIS_{Ln} result from the sum of two contributions: the Fermi contact shift and the pseudocontact shift.[46,47,54] Hence, the LIS_{Ln}(i) can be defined for each i resonance of the spectrum:

$$LIS_{Ln}\ (i) = \delta^{FC}(i) + \delta^{PC}(i) \qquad (1.4)$$

The Fermi contact shift, δ^{FC}_{Ln}(i), of each i resonance is a result of the electron density due to the unpaired electrons of the lanthanide ion being delocalized onto the i nucleus and is given by the product of $\langle S_z \rangle_{Ln}$, which is a magnetic constant and correspond to the expectation value of the *z*-component of the total spin angular momentum for the Ln^{III} ion (Chapter 2, Supplementary Materials, Table S1), and F(i), which is the hyperfine coupling constant, related to the electronic features of the specific Ln ion.[54,55]

$$\delta^{FC}(i) = \langle S_z \rangle_{Ln}\ F(i) \qquad (1.5)$$

As mentioned above, because this delocalization occurs through bonds, can be accurately considered insignificant beyond four bonds.

The pseudocontact shift δ^{PC}_{Ln} (i), of each i proton, sometimes reported also as dipolar contribution, is the result of the lanthanide unpaired electron density interacting with the i nucleus through the space and is a consequence of the molecular structure of the complex. The structural information gleaned from the pseudocontact shifts are particularly interesting:, providing information about the structure of the complex in solution, and can be correlated with the structure in the solid state obtained by the X-Ray diffraction analysis. Hence an accurate determination of the δ^{PC}_{Ln}(i) contribution might confirm or refute if the solid-state structure is retained in solution or if a series of molecules made with the same ligand set but different lanthanide ions are isostructural in solution.[48–52]

Starting from these considerations, many methods were developed over the years for an accurate determination of the δ^{FC}(i) and δ^{PC}(i) contributions to the LIS(i)$_{Ln}$. Detailed descriptions can be found in literature, including the Bleaney's theory, which has be seen a key reference for over 40 years. [48–52]

The δ^{PC}_{Ln}(i) can be determined, following Bleaney's theory, as the product of three terms as follows:[56]

$$\delta^{PC}(i) = C_J B \frac{3cos^2\theta - 1}{r_i^3} = C_J B\, G(i) \qquad (1.6)$$

C_J(Ln) is the Bleaney's constant, which is a magnetic term characteristic of each lanthanide and correlated with the anisotropic (oblate or prolate) *4f*-shell electron distribution (Chapter 2, Supplementary Materials, Table S1).[57,58] B_{Ln} is a constant which gathers all the crystal field splitting parameters of various orders. Finally, the $\frac{3cos^2\theta-1}{r_i^3}$ term is the geometric term: it contains the information related to the structure of the compound in solution and will be here after indicated as G(i).[57] Theta (ϑ_i) is the angle formed by the

Ln^{III}-H_i direction with the molecular axis (along *z*), while r_i is the Ln^{III}-H_i distance. A schematic representation of these two measurements is provided by Figure 1.14. **Error! Reference source not found.**

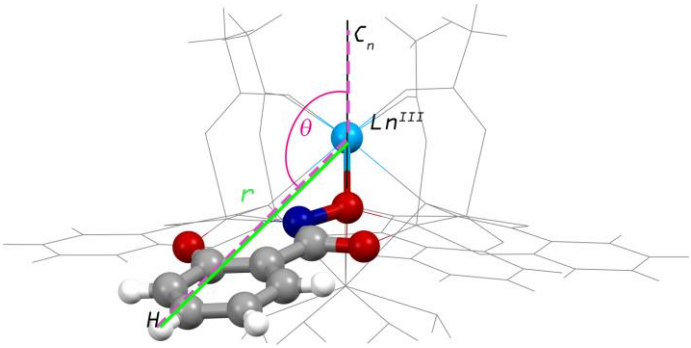

Figure 1.14 Schematic representation of the theta angle (ϑ_i pink) and of the radius (r_i, green) measurements in a Ln-derivative. The X-Ray structure is related to the $\{Ln^{III}(OAc)_4[12\text{-}MC_{Mn^{III}(N)shi}\text{-}4]\}^{-1}$ isostructural series of Ln-metallacrowns. One Shi^{3-} ligand (O-red, N-blue, C-grey, H-white) and the core Ln^{III} metal ion (light blue) are highlighted by ball-and-sticks style.[27]

Having (I) an isostructural series of Ln-C compounds, (II) an isostructural Y-C reference, and (III) H-atoms more than four bonds far from the Ln paramagnetic center, the $\delta^{FC}(i)$ can be assumed negligible. Thus, the observed $LIS_{Ln}(i)$ (eqn. 1.4) correspond to the pseudocontact shift (eqn. 1.7).

$$LIS_{Ln}(i) = \delta^{FC}(i) + \delta^{PC}(i) \sim \delta^{PC}(i) \qquad (1.7)$$

Thus, thanks to the definition of G(i), stated in eqn. 1.6, together with the approximations just listed above, it is possible to extrapolate the $G(i)^{NMR}_{Ln}$ term from the ^1H NMR data (eqn. 1.8). Each of the $G(i)^{NMR}_{Ln}$ values depend by the molecular structure of the complex in solution.

$$G(i)^{NMR}_{Ln} = \delta^{PC}_{Ln}(i)/C_{Ln}B_{Ln} \qquad (1.8)$$

A second geometrical term can be calculated: it is the $G(i)^{XRD}_{Ln}$ term, determined by the ϑ_i and r_i values, extracted from the X-Ray diffraction data. The $G(i)^{XRD}_{Ln}$ values depend by the molecular structure in the solid state.

The correlation of the $G(i)^{NMR}_{Ln}$ and $G(i)^{XRD}_{Ln}$ values would directly set out information upon the stability of the complexes in solution and upon the retention of the molecular structure after dissolution. However, it must be accounted that the calculation of the Bleaney's theory (eqn. 1.6) relies on many assumptions, in addition to the approximations already mentioned.In between these, the Bleaney's theory states that the crystal field parameters are small compared to *kT*, which may be at least questionable, when not incorrect. Hence, the C_J (Ln) constants should be regarded just as first approximation values, rather than accurate terms. Also, both minor and major variations of the B_{Ln} term may occur along the series, due to the lanthanide radius contraction and the differences in the number of axial coordinated solvents. Indeed, the Bleaney's theory has been recently criticized.[47,59]

Nevertheless, beside the overall issues accounted to the Bleaney's theory, the information gleaned from the paramagnetic ^{1}H NMR are still very interesting and accurate evaluations of both the δ^{PC}_{Ln} and the $G(i)^{NMR}_{Ln}$ terms, would still allow to correlate the structure in solution to that in the solid state.

Several alternative methods for the ^{1}H NMR paramagnetic data treatment were, therefore, developed in the last two decades. Among these, one of the most accurate approach is provided by the "*all lanthanides*" method, which leads to determine both the δ^{FC}_{Ln} and the δ^{PC}_{Ln} contributions to the LIS_{Ln}, avoiding any explicit reference to the C_J constants or to the crystal field parameters which may bias the results.[46,55,60] Moreover, the

paragraph 1.3.4 will show how this powerful method provides an indirect way to accurately correlate the molecular structure in solution to the one in the solid state.

1.3.3 The "*all lanthanides*" method

The "*all lanthanides*" method is a data treatment of the LIS_{Ln}(i), purposed by L. Di Bari et al. in 2011,[46] which can be applied to isostructural series of Ln-derivatives, that obey the same boundary conditions listed at the beginning (paragraph 1.3.1). In addition, the Fermi contact contribution to the paramagnetic shift has to be negligible, which means that the experimental LIS_{Ln} can be determined as reported in eqn. 1.7.

The "*all lanthanides*" calculations must be applied by following these four steps:

I- selection of a *reference compound*:

It has to be the best characterized one (with the largest set of unambiguously assigned resonances) and has to be endowed with a large C_J and $C_J/\langle S_z\rangle_{Ln}$, ratio. Usually the best choice for Ln-based isostructural series is the Yb-C.

II- determination of *plot-I*:

The LIS_{Ln}(i) is reported as a function of the $LIS_{reference}$(i), which is usually Yb^{III}-derivative for each **i** proton. The linear regression forced through the origin is calculated for each **i** proton and the resulting best fits are included in *plot-I* as well. The linear regression gives the $\mathbf{m}_{Ln}$ values of the slopes for each resonance of the spectrum. If these lines deviate from linearity, it means that:

- the specific Ln-C is not isostructural to the Yb-C (reference)
- if this occurs along the overall series, it means that the Fermi contact contribution is not negligible.

Deviations from linearity have been previously ascribed to structural changes along the series (variation of $G(i)^{NMR}_{Ln}$), but variations in the hyperfine coupling or in the crystal-field due to some electronic effects have been recently accounted as significative alternatives. In both cases the method cannot be applied. [46,55,61]

If the calculated-fits are linear (which means that the Fermi contact contribution is negligible) and no significant changes in the B and C_J values take place along the series, then the $\mathbf{m}_{Ln}$ correspond to the $C_{J,Ln}/C_{J,Yb}$ ratio.

III- <u>determination of the *plot-II*</u>:

For those complexes, that show linear trends in *plot-I*, the $\delta^{para}_{Ln}(i)/(S_z)_{Ln}$ ratio is plotted as a function of the $m_{Ln}/(S_z)_{Ln}$ δ^{PC}_{Mn} ratio. The equation which describes this function follows:

$$\frac{\delta^{para}{}_{Ln}(i)}{< Sz >_{Ln}} = m\frac{m_{Ln}}{< Sz >_{Ln}} + q = F(i) + G(i)BC_J^{ref}\frac{m_{Ln}}{< Sz >_{Ln}} \qquad (1.9)$$

Here, the slopes and the intercepts of what shall be another set of straight lines are defined as follows:

$$M(i) = G(i)BC_{J,Yb} \qquad (1.10)$$

$$Q(i) = F(i) \qquad (1.11)$$

IV- <u>determination of the δ^{FC}_{Ln} and δ^{PC}_{Ln} contributions</u>:

If the *plot-II* gives straight lines, the two δ^{FC}_{Ln} and δ^{PC}_{Ln} contributions to the LIS_{Ln} can be calculated, as follows:

$$M(i) = \delta^{PC}_{Yb} \qquad (1.12)$$

$$m_{Ln} \times M(i) = \delta^{PC}_{Ln} \qquad (1.13)$$

$$Q(i) \times (S_z)_{Ln} = \delta^{FC}_{Ln} \qquad (1.14)$$

The "true values" of the pseudocontact contribution to the LIS_{Ln} can be determined only experimentally, nevertheless examples of applications of the *"all lanthanides"* method, reported in literature, confirm that the δ^{PC}_{Ln} calculated compare well with sets of geometrical factors arising from the structural optimization calculations.[46]

Thus, the "*all lanthanides*" method can be confirmed as a "*model-free*" method, since it provides the opportunity to calculate the Fermi contact and pseudocontact contributions by only considering the ^1H NMR experimental data and without any involvement of magnetic and electronic approximation and assumptions, which are required (for example), if following the Bleaney's theory. This result in the possibility to easily characterize the structure in solution of lanthanide-based isostructural series of compounds. Moreover, the "*all lanthanide*" method can be used even in the case that only a few (at least two) numbers of Ln-C derivatives of a certain complex are known, independently of the position of the Ln ions within the series.

Another interesting feature of this method is that it is possible to mix and treat together heterogeneous data. This becomes relevant in some specific cases, for example when it is difficult to accurately know the nature of the species observed in solution.

1.3.4 Correlation of the structure in solution to the one in the solid state

When the crystallographic data related to molecular structure in the solid state are known, the parameters provided by the "*all lanthanides"* calculations, can be correlated to the X-Ray data. More specifically, each M(i) term can be correlated with the correspondent $G(i)^{XRD}$ term, as becomes evident by recalling the M(i) definition, reported in eqn. 1.10.

The eqn. 1.1 allows to observe that, when the molecular structure in the solid state is retained after dissolution, the $G(i)^{XRD}$ is proportional to the M(i) related to the same Ln ion. The simplest way to correlate the M(i) values to the $G(i)_{XRD}$ is to divide them by the smallest. This procedure allows to directly compare the two resulting parameters, by simplifying any B or C_J contributions, and by cancelling out any scaling factor and dimension. In terms of equations, for two different i and j protons in the same complex:

$$\frac{M(i)}{M(j)} = \frac{G(i)_{NMR} BC_{Yb}}{G(j)_{NMR} BC_{Yb}} \quad \text{vs} \quad \frac{G(i)_{XRD}}{G(j)_{XRD}} \tag{1.15}$$

If the M(i)/M(j) ratio corresponds to the $G(i)_{XRD}/G(j)_{XRD}$ ratio, it means that the molecular structure in solution perfectly matches the one in the solid state and that the i (or j) resonance corresponds to the Hi (or Hj) atom. Deviations from this ideal situation can be evaluated, and in principle they provide information upon rearrangements or fluxionality processes, occurring in solution.

Finally, from the calculation of these ratios it is possible to unequivocally assign the resonances of the ^{1}H NMR spectrum. Indeed, the $\mathbf{i}^{NMR}$ resonance will provide a M(i), which will correspond only to the $G(i)^{XRD}$ related to the $\mathbf{H_i}^{XRD}$ atom.

As a result, the “all lanthanides” calculations provide information, which can be used for the determination of the Fermi contact contribution, the pseudocontact shift and to confirm the overall resonances assignment of the paramagnetic spectra.

Bibliography

1. Lah MS, Pecoraro VL. Isolation and Characterization of (Mnii[Mniii(Salicylhydroximate)]4(Acetate)2(Dmf)6).2DMF - an Inorganic Analog of M2+ (12-Crown-4). J Am Chem Soc. 1989;111(18):7258-7259. doi:10.1021/ja00200a054
2. Pecoraro VL, Stemmler AJ, Gibney BR, et al. Metallacrowns: A New Class of Molecular Recognition Agents. In: Progress in Inorganic Chemistry. Vol 45. ; 2007:83-177. doi:10.1002/9780470166468.ch2
3. Bodwin JJ, Cutland AD, Malkani RG, Pecoraro VL. The development of chiral metallacrowns into anion recognition agents and porous materials. Coord Chem Rev. 2001;216-217:489-512. doi:10.1016/S0010-8545(00)00396-9
4. Atzeri C, Marchiò L, Chow CY, Kampf JW, Pecoraro VL, Tegoni M. Design of 2D Porous Coordination Polymers Based on Metallacrown Units. Chem - A Eur J. 2016;22(19). doi:10.1002/chem.201600562
5. Ostrowska M, Fritsky IO, Pavlishchuk A V. Metallacrown-based compounds: Applications in catalysis, luminescence, molecular magnetism, and adsorption. Coord Chem Rev. 2016;327:304-332. doi:10.1016/j.ccr.2016.04.017
6. Chow CYCY, Eliseeva SVS V, Trivedi ERER, et al. Ga3+/Ln3+Metallacrowns: A Promising Family of Highly Luminescent Lanthanide Complexes That Covers Visible and Near-Infrared Domains. J Am Chem Soc. 2016;138(15):5100-5109. doi:10.1021/jacs.6b00984
7. Deb A, Boron TT, Itou M, et al. Understanding spin structure in metallacrown single-molecule magnets using magnetic compton scattering. J Am Chem Soc. 2014;136(13). doi:10.1021/ja501452w
8. Happ P, Plenk C, Rentschler E. 12-MC-4 metallacrowns as versatile tools for SMM research. Coord Chem Rev. 2015;289-290(1):238-260. doi:10.1016/j.ccr.2014.11.012
9. Martinić I, Eliseeva S V, Nguyen TN, Pecoraro VL, Petoud S. Near-Infrared Optical Imaging of Necrotic Cells by Photostable Lanthanide-Based Metallacrowns. J Am Chem Soc. 2017;139(25):8388-8391. doi:10.1021/jacs.7b01587
10. Lutter JC, Eliseeva S V, Kampf JW, Petoud S, Pecoraro VL. A Unique LnIII{[3.3.1]GaIIIMetallacryptate} Series That Possesses Properties of Slow Magnetic Relaxation and Visible/Near-Infrared Luminescence. Chem - A Eur J. 2018;24(42):10773-10783. doi:10.1002/chem.201801355
11. Grant JT, Jankolovits J, Pecoraro VL. Enhanced guest affinity and enantioselectivity through variation of the Gd3+ [15-metallacrown-5] side chain. Inorg Chem. 2012;51(15):8034-8041. doi:10.1021/ic300110g

12. Gibney BR, Wang H, Kampf JW, Pecoraro VL, Bldg R. Structural Evaluation and Solution Integrity of Alkali Metal Salt Complexes of the Manganese 12-Metallacrown-4 (12-MC-4) Structural Type. 1996;89(1):6184-6193. doi:10.1021/ic960371+
13. Lah M Pecoraro V. Isolation and characterization of {MnII[MnIII(salicylhydroximate)]4(acetate)2(DMF)6}.cntdot.2DMF: an inorganic analog of M2+(12-crown-4. J Am Chem Soc. 1989;111(18):7258-7259. doi:10.1021/ja00200a054
14. Gibney BR, Wang H, Kampf JW, Pecoraro VL, Bldg R.) Pedersen. Vol 89. American Chemical Society; 1996. doi:10.1021/ic960371+
15. Lah MS, Pecoraro VL. Isolation and Characterization of (Mnii[Mniii(Salicylhydroximate)]4(Acetate)2(Dmf)6).2Dmf - an Inorganic Analog of M2+ (12-Crown-4). J Am Chem Soc. 1989;111(18):7258-7259. doi:10.1021/ja00200a054
16. Gibney BR, Kessissoglou DP, Kampf JW, Pecoraro VL. Copper(II) 12-Metallacrown-4: Synthesis, Structure, Ligand Variability, and Solution Dynamics in the 12-MC-4 Structural Motif. Inorg Chem. 1994;33(22):4840-4849. doi:10.1021/ic00100a006
17. Lah MS, Pecoraro VL. A functional analogy between crown ethers and metallacrowns. Inorg Chem. 1991;30(5):878-880. doi:10.1021/ic00005a002
18. Arnaud-Neu F, Delgado R, Chaves S. Critical evaluation of stability constants and thermodynamic functions of metal complexes of crown ethers (IUPAC Technical Report). Pure ApplChem. 2003;75(1):71-102.
19. Tegoni M, Remelli M. Metallacrowns of copper(II) and aminohydroxamates: Thermodynamics of self assembly and host-guest equilibria. Coord Chem Rev. 2012;256(1-2):289-315. doi:10.1016/j.ccr.2011.06.007
20. clathrate H. Figure 1.1 The structures of (a) Prussian Blue 2 and (b) the View Online. 2008. doi:10.1039/9781847558862-00001
21. Atzeri C, Marchiò L, Chow CY, Kampf JW, Pecoraro VL, Tegoni M. Design of 2D Porous Coordination Polymers Based on Metallacrown Units. Chem - A Eur J. 2016;22(19):6482-6486. doi:10.1002/chem.201600562
22. Jankolovits J, Kampf JW, Pecoraro VL. Insight into the structural versatility of the Ln(III)[15-metallacrown-5] platform by comparing analogs with Ni(II), Cu(II), and Zn(II) ring ions. Polyhedron. 2013;52:491-499. doi:10.1016/j.poly.2012.08.046
23. Lim C-S, Jankolovits J, Zhao P, Kampf JW, Pecoraro VL. Gd(III)[15-metallacrown-5] recognition of chiral α-amino acid analogues. Inorg Chem. 2011;50(11). doi:10.1021/ic102579t
24. Marchiò L, Marchetti N, Atzeri C, Borghesani V, Remelli M, Tegoni M. The peculiar behavior of Picha in the formation of metallacrown complexes with Cu(II), Ni(II) and Zn(II) in aqueous solution. Dalt Trans. 2015;44(c):3237-3250. doi:10.1039/C4DT03264K

25. Golenya IA, Gumienna-Kontecka E, Boyko AN, Haukka M, Fritsky IO. Collapsed Cu(II)-Hydroxamate Metallacrowns. Inorg Chem. 2012;51(11):6221-6227. doi:10.1021/ic300387e
26. Nguyen TN, Chow CY, Eliseeva S V., et al. One-Step Assembly of Visible and Near-Infrared Emitting Metallacrown Dimers Using a Bifunctional Linker. Chem - A Eur J. 2018;24(5):1031-1035. doi:10.1002/chem.201703911
27. Azar MR, Boron TT, Lutter JC, et al. Controllable Formation of Heterotrimetallic Coordination Compounds: Systematically Incorporating Lanthanide and Alkali Metal Ions into the Manganese 12-Metallacrown-4 Framework. Inorg Chem. 2014;53(3):1729-1742. doi:10.1021/ic402865p
28. Mengle KA, Longenecker EJ, Zeller M, Zaleski CM. One-Dimensional Coordination Polymers of 12-Metallacrown-4 Complexes: {Na2(L)2[12-MCMnIIIðNÞshi-4]}n, where L is Either -O2CCH2CH3 or -O2CCH2CH2CH3. J Chem Crystallogr. 2015;45(1):36-43. doi:10.1007/s10870-014-0560-0
29. Jankolovits J, Kampf JW, Pecoraro VL. Insight into the structural versatility of the Ln(III)[15-metallacrown-5] platform by comparing analogs with Ni(II), Cu(II), and Zn(II) ring ions. 2013. doi:10.1016/j.poly.2012.08.046
30. Shannon RD. Revised Effective Ionic Radii and Systematic Studies of Interatomie Distances in Halides and Chaleogenides. Acta Cryst. 1976;32.
31. Zaleski CM, Lim C-S, Cutland-Van Noord AD, Kampf JW, Pecoraro VL. Effects of the central lanthanide ion crystal radius on the 15-MCCu II(N)pheHA-5 structure. Inorg Chem. 2011;50(16). doi:10.1021/ic200740h
32. Stemmler AJ, Kampf JW, Pecoraro VL. Synthesis and Crystal Structure of the First Inverse 12-Metallacrown-4. Inorg Chem. 1995;34(9):2271-2272. doi:10.1021/ic00113a005
33. Feng P-Y, Yang C-I, Huang P-J, Lee G-H, Tsai H-L. A helical salicyladoxime-based manganese triangle chain with single-molecule magnet behavior. Inorg Chem Commun. 2015;55:112-115. doi:10.1016/j.inoche.2015.03.034
34. Liu M-H, Yang C-I, Lee G-H, Tsai H-L. A new dodecanuclear manganese single-molecule magnet from the arrangement of manganese triangles. Inorg Chem Commun. 2011;14(7):1136-1139. doi:10.1016/j.inoche.2011.04.007
35. Low DM, Brechin EK, Helliwell M, Mallah T, Rivière E, Mcinnes EJL. New routes to high nuclearity cages: dimerisation of a manganese triangle via solvothermal synthesis. doi:10.1039/b305245a
36. Milios CJ, Wood PA, Parsons S, et al. The use of methylsalicyloxime in manganese chemistry: A ½Mn. 2007. doi:10.1016/j.ica.2007.06.031

37. Batten SR, Champness NR, Chen X-M, et al. Terminology of metal–organic frameworks and coordination polymers (IUPAC Recommendations 2013)*. Pure Appl Chem. 2013;85(8):1715-1724. doi:10.1351/PAC-REC-12-11-20
38. Yaghi OM, Li Q. Reticular chemistry and metal-organic frameworks for clean energy. MRS Bull. 2009;34(9):682-690. doi:10.1557/mrs2009.180
39. Zhou H-C, Long JR, Yaghi OM. Introduction to Metal–Organic Frameworks. Chem Rev. 2012;112(2):673-674. doi:10.1021/cr300014x
40. Furukawa H, Cordova KE, O'Keeffe M, Yaghi OM. The Chemistry and Applications of Metal-Organic Frameworks. Science (80-). 2013;341(6149):1230444. doi:10.1126/science.1230444
41. Tranchemontagne DJ, Mendoza-Cortés JL, O'Keeffe M, Yaghi OM. Secondary building units, nets and bonding in the chemistry of metal–organic frameworks. Chem Soc Rev. 2009;38(5):1257. doi:10.1039/b817735j
42. Eddaoudi M, Moler DB, Li H, et al. Modular chemistry: Secondary building units as a basis for the design of highly porous and robust metal-organic carboxylate frameworks. Acc Chem Res. 2001;34(4):319-330. doi:10.1021/ar000034b
43. Bertini I. LC. Chapter 2 The hyperfine shift. Coord Chem Rev. 1996;150:29-75. doi:10.1016/0010-8545(96)01242-8
44. Bertini I, Luchinat C. Chapter 1 Introduction. Coord Chem Rev. 1996;150:1-28. doi:10.1016/0010-8545(96)01241-6
45. Bertini I, Capozzi F, Luchinat C, Nicastro G, Xia Z. Water proton relaxation for some lanthanide aqua ions in solution. J Phys Chem. 1993;97(24):6351-6354. doi:10.1021/j100126a007
46. Di Pietro S, Piano S Lo, Di Bari L. Pseudocontact shifts in lanthanide complexes with variable crystal field parameters. Coord Chem Rev. 2011;255(23-24):2810-2820. doi:10.1016/j.ccr.2011.05.010
47. Blackburn OA, Edkins RM, Faulkner S, et al. Electromagnetic susceptibility anisotropy and its importance for paramagnetic NMR and optical spectroscopy in lanthanide coordination chemistry. Dalt Trans. 2016;45(16):6782-6800. doi:10.1039/C6DT00227G
48. Di Bari L, Pintacuda G, Salvadori P, Dickins RS, Parker D. Effect of axial ligation on the magnetic and electronic properties of lanthanide complexes of octadentate ligands. J Am Chem Soc. 2000;122(38):9257-9264. doi:10.1021/ja0012568
49. Valencia L, Martinez J, Macías A, Bastida R, Carvalho RA, Geraldes CFGC. X-ray diffraction and 1H NMR in solution: Structural determination of lanthanide complexes of a Py2N6Ac4 ligand. Inorg Chem. 2002;41(20):5300-5312. doi:10.1021/ic0257017
50. Di Bari L, Lelli M, Pintacuda G, Pescitelli G, Marchetti F, Salvadori P. Solution versus Solid-State Structure of Ytterbium Heterobimetallic Catalysts. J Am Chem Soc. 2003;125(18):5549-5558. doi:10.1021/ja0297640

51. Fernández-Fernández MDC, Bastida R, Macías A, Pérez-Lourido P, Platas-Iglesias C, Valencia L. Lanthanide(III) complexes with a tetrapyridine pendant-armed macrocyclic ligand: 1H NMR structural determination in solution, X-ray diffraction, and density-functional theory calculations. Inorg Chem. 2006;45(11):4484-4496. doi:10.1021/ic0603508
52. Di Bari L, Di Pietro S, Pescitelli G, Tur F, Mansilla J, Saá JM. [Ln(binolam)3]·(OTf)3, a New Class of Propeller-Shaped Lanthanide(III) Salt Complexes as Enantioselective Catalysts: Structure, Dynamics and Mechanistic Insight. Chem - A Eur J. 2010;16(47):14190-14201. doi:10.1002/chem.201001683
53. Peters JA, Huskens J, Raber DJ. Lanthanide induced shifts and relaxation rate enhancements. Prog Nucl Magn Reson Spectrosc. 1996;28(3):283-350. doi:10.1016/0079-6565(95)01026-2
54. Bertini I, Luchinat C. Chapter 3 Relaxation. Coord Chem Rev. 1996;150:77-110. doi:10.1016/0010-8545(96)01243-X
55. Rigault S, Piguet C. Predictions and assignments of NMR spectra for strongly paramagnetic supramolecular lanthanide complexes: The effect of the “gadolinium break” [5]. J Am Chem Soc. 2000;122(38):9304-9305. doi:10.1021/ja000958u
56. Bleaney - J. Magn. Res. 1972.pdf. J Magn Reson. 1972;8:91-100.
57. Bleaney B. Nuclear magnetic resonance shifts in solution due to lanthanide ions. J Magn Reson. 1972;8(1):91-100. doi:10.1016/0022-2364(72)90027-3
58. Rinehart J, Long J. Exploiting single-ion anisotropy in the design of f-element single-molecule magnets. Chem Sci. 2011;2(11):2078-2085. doi:10.1039/c1sc00513h
59. S. Dickins R, Parker D, I. Bruce J, J. Tozer D. Correlation of optical and NMR spectral information with coordination variation for axially symmetric macrocyclic Eu(III) and Yb(III) complexes: axial donor polarisability determines ligand field and cation donor preference. Dalt Trans. 2003;127(7):1264-1271. doi:10.1039/b211939k
60. Funk AM, A Finney K-LN, Harvey P, et al. Critical analysis of the limitations of Bleaney’s theory of magnetic anisotropy in paramagnetic lanthanide coordination complexes. Chem Sci. 2015;6:1655-1662. doi:10.1039/c4sc03429e
61. Dixon WT, Ren J, Lubag AJM, et al. A concentration-independent method to measure exchange rates in PARACEST agents. Magn Reson Med. 2010;63(3):625-632. doi:10.1002/mrm.22242

Chapter 2

STUDY OF HETEROBIMETALLIC Ln^{III}/Mn^{III} AND Ln^{III}/Ga^{III} 12-MC-4 COMPLEXES IN THE SOLID STATE AND IN SOLUTION

"Imagination is not only the uniquely human capacity to envision that which is not, and therefore the fount of all invention and innovation. In its arguably most transformative and revelatory capacity, it is the power to that enables us to empathize with humans whose experiences we have never shared"

J. K. Rowling

Introduction

The use of coordination complexes of lanthanide ions is of wide interest in areas such as biomedical analysis, catalysis, magnetic resonance imaging, luminescence, and single-molecule magnetism.[1–18] In the study of these complexes, it is often useful to correlate the structural features of such compounds in the solid state (e.g. from crystallographic data) with their properties in solution. One common technique used to characterize the lanthanide coordination complexes in solution is monodimensional ^{1}H NMR: The lanthanide unpaired electrons influence the NMR features which are strongly related to the structure of the Ln^{III} complex in solution. Although broader than those of diamagnetic species, the resonances in the NMR spectra of Ln^{III} complexes are observable (with the general exception of the Gd^{III} derivatives). In fact, the spin-orbit coupling of the unpaired *4f* electrons leads to short electronic relaxation times, hence, ligand proton signals are commonly observable.[19,20] The presence of unpaired electrons, also, induces a paramagnetic shift (δ^{para}) to the protons signals of the lanthanide-based compounds. This effect is defined Lanthanide Induced Shift (LIS_{Ln}), which, as described in paragraph 1.3, is made of two components: the Fermi contact shift and the pseudocontact shift (vide eqn.s 1.4-6).[19–21] The structural information gleaned from the pseudocontact shifts can confirm or refute if the solid-state structure is retained after dissolution or if a series of molecules made with the same ligand set but different lanthanide ions are isostructural in solution along the series.[22–26]

The structures in the solid state of the M^{n+}[12-$MC_{M(III),(O)H3Shi-3H}$-4] class of MCs have been extensively studied over the years.[27–35] Many examples and features, indeed, are reported in literature.[35–38] Moreover, the first metallacrown that has been isolated from the Pecoraro group is the $Mn^{II}(OAc)_2$[12-$MC_{Mn^{III}(O)H3Shi-3H}$-4], and belongs to this class (Fig 1.1).[27] The single-

molecule magnetic properties of this species both in the solid state and in solution have been described by Pecoraro and Lah in 2011.[39] In addition, the solution state integrity of this molecule and its stability have been studied through ^{1}H NMR experiments.[30]

Here the investigation of the ^{1}H NMR behavior of two isostructural series of paramagnetic Ln^{III}-metallacrowns is reported. Those are:

- the $Ln^{III}Na^{I}(OAc)_4[12\text{-}MC_{Mn^{III}(O)H3Shi\text{-}3H}\text{-}4](H_2O)_4 \cdot 6DMF$ series, were Ln = Pr, Nd, Sm, Eu, Gd, Tb, Dy, Ho, Er, Tm, Yb and Y (**$LnMn_4$**);

- the $Ln^{III}Na^{I}(OBz)_4[12\text{-}MC_{Ga^{III}(O)H3Shi\text{-}3H}\text{-}4](H_2O)_4 \cdot xDMF$ series, were Ln = La, Pr, Nd, Sm, Eu, Gd, Tb, Dy, Ho, Er, Tm, Yb, Lu and Y (**$LnGa_4$-2**).

The previously reported $Ln^{III}(OBz)_4[12\text{-}MC_{Ga^{III}(O)H3Shi\text{-}3H}\text{-}4](Hpy)(py)(CH_3OH)$ (Ln = Sm, Eu, Gd, Tb, Dy, Ho, Er, Tm, Yb) series of compounds, further on reported as **$LnGa_4$-1**, is isostructural to the $LnGa_4$-2 one. The $DyGa_4$-1 crystal structure can be found in literature too. It will be recalled here and compared with the polymorphic one found for $LnGa_4$-2.[40]

All these complexes show the typical 12-MC-4 structural motif, which result from the self-assembly in solution of four salicylhydroxamate ligands (shi^{3-}) and four Mn^{III}/Ga^{III} ions (**Figure 2.1**, left). The lanthanide ions are too large to fit the central cavity; hence they are coordinated above it and are kept in that position thanks to four carboxylate molecules which bridge between the ring metals and the lanthanide core ion (more details will be described further on).

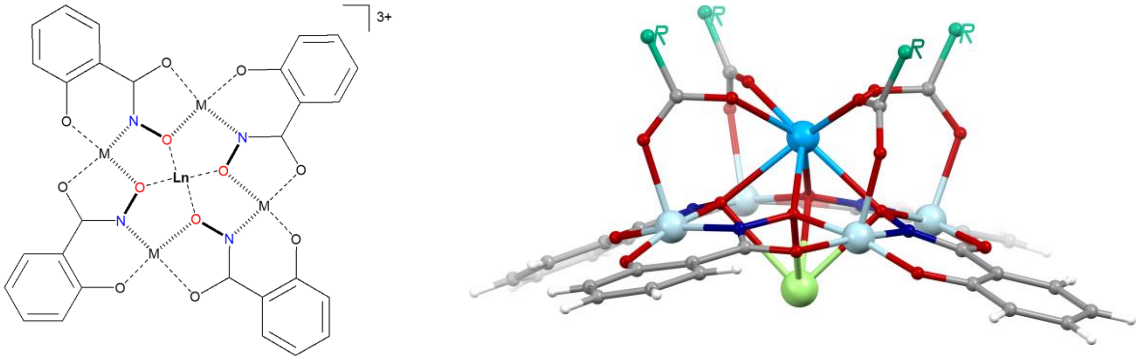

Figure 2.1 Schematic representation of: (**left**) the Ln^{III}[12-$MC_{M,\ (O)H3Shi-3H}$-4] scaffold; (**right**) the Ln^{III} ion encapsulation above the MC-ring, thanks to the presence of four R-COO^- carboxylic bridges. Colors code: Ln-cyan, M-light blue, O-red, C-grey, R-emerald.

The $LnMn_4$ complexes were previously reported and investigated for their SMM behavior,[41] while the $LnGa_4$-1 molecules have been recently reported as promising luminescent probes.[40] Moreover, the $LnMn_4$ solid-state crystal structures were extensively investigated through single-crystal X-Ray diffraction analysis, and recently it was shown that it is possible to crystallize isostructural scaffolds by replacing the acetate linkers, which bridge the central Ln^{III} to the ring Mn^{III} ions, with other carboxylate ligands (i.e. benzoate, salicylate, and trimethylacetate).[33,42,43] As for the $LnGa_4$ series, it might be interesting to characterize their behavior in solution, to understand the molecules integrity after dissolution and to investigate if they retain their isostructural nature in the solution state.

The ^1H NMR study gives the opportunity to investigate the features in solutions of these two series of molecules, and to correlate the metallacrown features in solution with those in the solid state, once the crystal structures have been determined by X-Ray analysis.

The presence of lanthanide ions, as core metal of the 12-MC-4 scaffold, results in the possibility to calculate the pseudocontanct contribution to the chemical shift and the related geometrical term by following the "*all lanthanide*s" approach (vide paragraph 1.3.3). Indeed, these calculations provide information upon the stability of the molecules in solution and upon their molecular structure, which can be compared (since in this case are available) with the respective crystal structure.

Overall these considerations follow the possibility to accurately assign the ^{1}H NMR resonances. However, the "*all lanthanide*s" method can serve to this purpose either.

Thus, the present discussion provides a more complete understanding of the properties and characteristics of this class of molecules. The solid state data are correlated to the those resulting from the ^{1}H-NMR investigation in solution. Bandwidths and chemical shifts have been analyzed, by following the "*all lanthanides*" calculations.

In addition, the study of the $LnMn_4$ complexes relates on a compound which bears five paramagnetic centers (i.e. four Mn^{III} ions and one Ln^{III} ion); our results demonstrate that the pseudocontact and Fermi contact contributions to the LIS_{Ln} can be determined with good precision even in the presence of multiple paramagnetic centers. Part of these results, including the crystal structures of the $Ln^{III}Na^{I}(OAc)_4[12\text{-}MC_{MIII(O)H3Shi\text{-}3H}\text{-}4](H_2O)_4\cdot(DMF)_6$, where Ln = Pr, Nd, Sm, Eu, Gd, Tb, Dy, Ho, Er, Tm, Yb and Y ($LnMn_4$), and the analysis of the ^{1}H-NMR data, have been recently reported in the literature by Atzeri, Marzaroli, Zaleski, Tegoni et al.[33,44]

Results and discussion

2.1. The structures in the solid state

The structures in the solid state have been collected for an accurate understanding and interpretation of the ^{1}H-NMR data. The present section highlights those aspects that are useful to support the discussion carried out in section 3.2. The analytical description of the crystal structures of the complete series of $LnGa_4$-2 compounds will be reported in a follow-up work.

2.1.1 Solid state structures of the $Ln^{III}Na^{I}(OAc)_4[12\text{-}MC_{Mn^{III}(O)H3Shi\text{-}3H}\text{-}4]$ complexes

The crystal structures of the $Ln^{III}Na^{I}(OAc)_4[12\text{-}MC_{MIII(O)H3Shi\text{-}3H}\text{-}4](H_2O)_4(DMF)_6$, where Ln stays for Pr, Nd, Sm, Eu, Gd, Tb, Dy, Ho, Er, Tm, Yb and Y (**$LnMn_4$**), have been obtained by our collaborators, in the group of Prof. Zaleski, at the Shippensburg University (PA, USA).[33] The overall twelve $LnMn_4$ molecules, crystallize in the P-1 space group and are isostructural within the series. The $LnMn_4$ structures show the classical 12-MC-4 motif with the lanthanide and sodium ions bound on opposite faces of the central cavity.

The $DyMn_4$ crystal structure can be described as representative for all the others of the series (Figure 2.2, top). The $DyMn_4$ macrocyclic scaffold is domed with the lanthanide ion captured on the convex side of the cavity, while the Na^{I} is coordinated on the concave side (underside) of it. Moreover, four acetate linkers allow the lanthanide ion to be encapsulated, by coordinating the Dy on one side and the Mn^{III} on the other one. The 4-fold symmetry axis, typical for 12-MC-4 molecules, is here only a pseudo-C_4 axis. Indeed, the distortions, which undergo the periphery of the MC-ring and the four acetate linkers (Figure 2.2, top-right) lead the four slices not to be equivalent by symmetry.

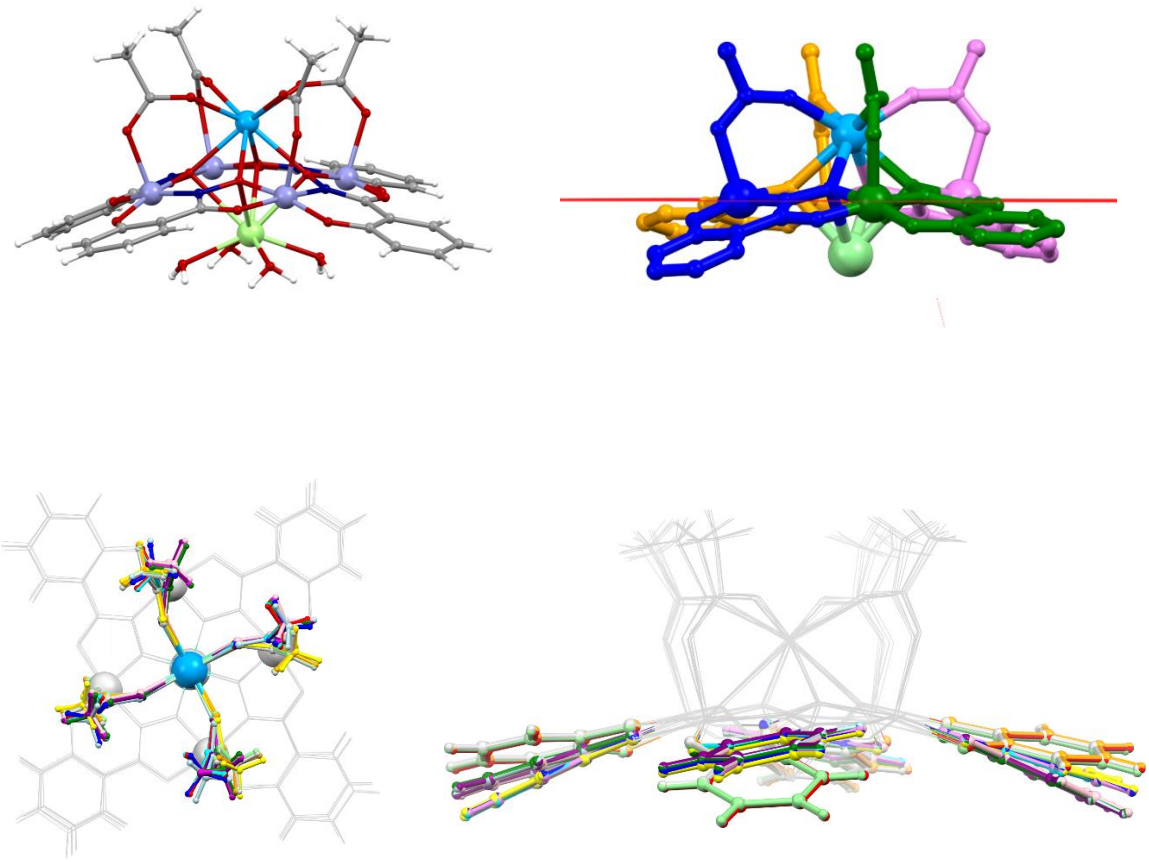

Figure 2.2 Top-left: X-Ray crystal structure of the $Dy^{III}Na^{I}(OAc)_4[12\text{-}MC_{MIII(O)H3Shi\text{-}3H}\text{-}4](H_2O)_4$ species. **Top-right:** X-Ray crystal structure of the $DyMn_4$ spices, highlighting (I) the four slices resulting from the pseudo-C_4 axis (each has a different color: green, blue, pink and orange), (II) the Mn mean plane is marked in red and (III) how the acetate linkers and the shi^{3-} ligands are slightly twisted one respect to the others, leading the molecular axis to be a pseuco-C_4. **Bottom:** overlay of the 12 crystal structures of the $Ln^{III}Na^{I}(OAc)_4[12\text{-}MC_{Mn^{III}(O)H3Shi\text{-}3H}\text{-}4]$ (Ln = Pr, Nd, Sm, Eu, Gd, Tb, Dy, Ho, Er, Tm, Yb and Y) compounds. The top (left) and side (right) views are reported, highlighting how the acetate linkers and the shi^{3-} ligands slightly twist along the series.[33]

The overlap of the 12 $LnMn_4$ structures (Figure 2.2, bottom) provides the evidence, that the cores of the metallacrown scaffolds (i.e. metal ions and heteroatoms) perfectly superimpose along the series. Small differences in the periphery are in charge of the aromatic rings and acetates linkers, especially at the external methyl groups.

A closer inspection of the crystallographic data makes evident that the smaller the lanthanide, (I) the shorter the distance between the Ln and the cavity oxygen mean plane (Ln-O_{ox}MP), (II) the longer the O_{ac}-Ln bonds, and (III) the smaller the angle about the axial coordination of the Mn^{III} ions (i.e. $Centroid_{ox}$-Mn^{III}-O_{ac} average angles). This means that from Pr^{III} to Yb^{III}, the lanthanide ion becomes closer to the cavity and the overall scaffold is less domed. The position of Na^{I} with respect to the cavity is constant along the series and as a result, from Pr^{III} to Yb^{III}, the Ln^{III}-Na^{I} distance becomes shorter. Overall distances and angles, which support these considerations are reported in Table S2 (Chapter 2, Supplementary Materials). Overall these considerations allow to attribute the structural small differences, that arise along the series, to the change of the ionic radius of the encapsulated lanthanide ion.

Interestingly, when La^{III} and Ce^{III} (the largest and lightest of the lanthanides) or Lu^{III} (the smallest and heaviest one) were used to assemble the metallacrown, the $Na^{I}_2(OAc)_2$[12-$MC_{Mn^{III}(O)H3Shi-3H}$-4](DMF)$_6$ species was isolated instead. One important consideration follows: the stability of the $LnMn_4$ seems depend on the ionic radius of the lanthanide. This has been previously proven for 15-$MC_{Cu,L}$-5 complexes.[45,46] and implies that the $GdMn_4$ (which is at the center of the series) and of YMn_4 (which has an ionic radius close to that of Gd^{III}) are expected to be stable in solution. The relevance of the YMn_4 is related to the fact that it can acts as diamagnetic reference for the $LnMn_4$ series.

The Na_2Mn_4 spices offers the opportunity to discuss how the presence of a second Na^{I} ion coordinated above the cavity, instead of a lanthanide one, results in a pseudo-planar scaffold (Figure 2.3). This suggests that the presence of the lanthanide ion is crucial for the molecular doming conformation. The superimposition of the X-Ray-structures of the $Na^{I}_2(OAc)_2$[12-

$MC_{MnIII(O)H3Shi-3H}$ -4](DMF)$_6$ (grey), the $Mn^{II}_2(OAc)_2$[12-$MC_{MnIII\ (O)H3Shi-3H}$-4](DMF)$_6$ (purple) and the $Dy^{III}Na^{I}(OAc)_4$[12-$MC_{MnIII(O)H3Shi-3H}$-4](DMF)$_6$ (green) species shows the structural differences between the scaffolds of the three species (**Figure 2.3**).

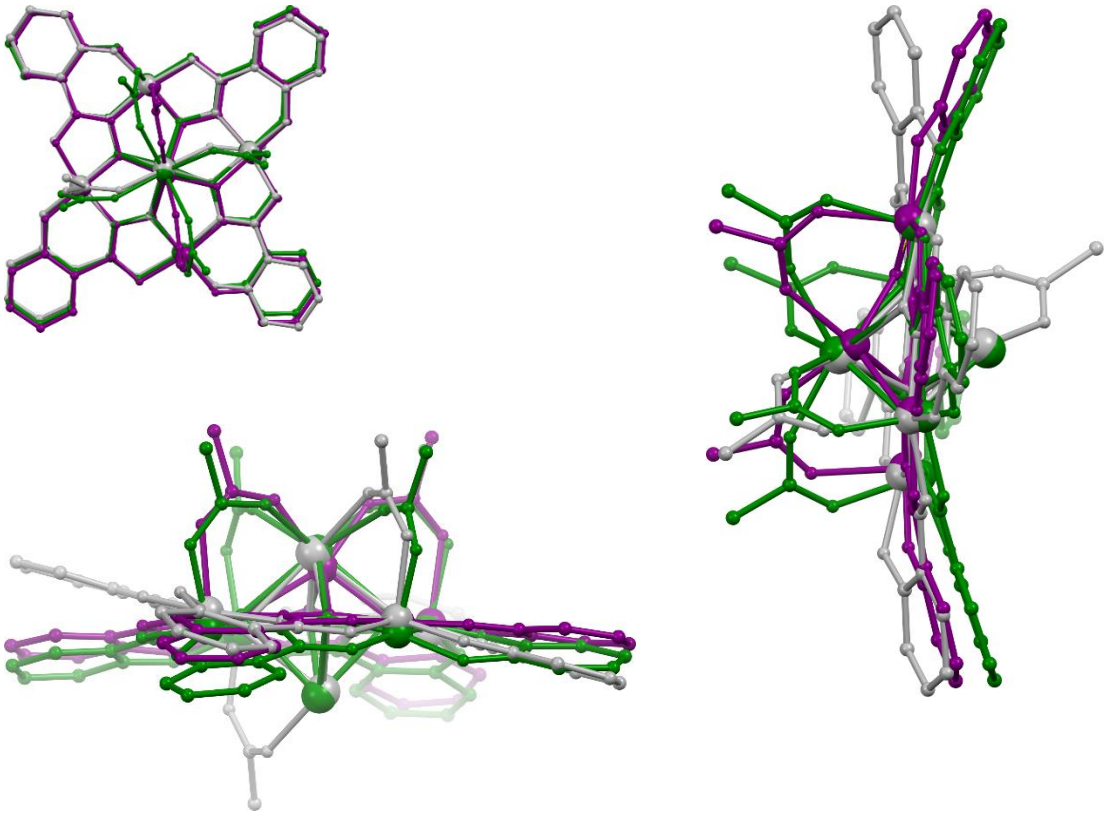

Figure 2.3 Overlay of the $Na^{I}_2(OAc)_2$[12-$MC_{MnIII\ (O)H3Shi-3H}$-4] (grey), $Mn^{II}_2(OAc)_2$[12-$MC_{MnIII\ (O)H3Shi-3H}$-4] (purple) and the $Dy^{III}Na^{I}(OAc)_4$[12-$MC_{MnIII\ (O)H3Shi-3H}$-4] (green) X-Ray-structures. The Na_2Mn_4 species is much less domed than the other two. The most domed scaffold is the one where the lanthanide ion is encapsulated.[33,47]

2.1.2 Solid state structures of the $Ln^{III}Na^{I}(OBz)_4$[12-$MC_{GaIII(O)H3Shi-3H}$-4] complexes

We found and here report how the $Ln^{III}Na^{I}(OBz)_4$[12-$MC_{MnIII\ (O)H3Shi-3H}$-4]$(H_2O)_4(DMF)_x$ series of complexes ($LnGa_4$-2) crystallize with the same architecture of the $LnMn_4$ one, having the Na^{I} counterion coordinated at the concave face of the 12-MC-4 scaffold.

The $LnGa_4$ species have firstly been isolated by Pecoraro et al., which reported the crystal structure of $Dy^{III}(OBz)_4[12\text{-}MC_{Mn^{III}\ (O)H3Shi\text{-}3H}\text{-}4](Hpy)(py)(H_2O)_2$ ($DyGa_4$-1), determined by single crystal X-Ray diffraction analysis. The $LnGa_4$-1 MCs (where Ln stays for Sm, Eu, Gd, Tb, Ho, Er, Tm and Yb) were characterized by X-Ray powder diffraction analysis and were found isostructural to the $DyGa_4$-1 derivative.[40] Compared with $Ln^{III}Na^{I}(OBz)_4[12\text{-}MC_{Ga^{III}(O)H3Shi\text{-}3H}\text{-}4]$, the $LnGa_4$-1 spices differ in the counterion. Pecoraro et al. found the underside of the central cavity empty and a pyridinium counterion co-crystallized about the molecule (Figure 2.4-Left).

Here the $Ln^{III}Na^{I}(OBz)_4[12\text{-}MC_{Mn^{III}\ (O)H3Shi\text{-}3H}\text{-}4](H_2O)_4(DMF)_x$ isostructural series, where Ln stays for La, Pr, La, Nd, Sm, Eu, Gd, Tb, Dy, Ho, Er, Tm, Yb, Lu and Y (excluded the Ce and Pm) is reported. Single crystal X-Ray diffraction complete data collections were carried out for Dy, Ho, Er, Lu and Y derivatives (crystallographic tables are reported in Table S3, Chapter 2, Supplementary Materials). It is worth notice that $LuGa_4$-1 complex has been isolated, and that it might be used in principle as a diamagnetic reference, even if, for a uniformity, YGa_4-1 has been chosen as diamagnetic reference.

Beside the molecular architectures are the same, the $DyGa_4$-1 crystallizes in the monoclinic $P2_1/n$ space group, and for the $LnGa_4$-2 complexes two more packing behaviors have been found: $DyGa_4$-1 crystallizes in the Pn monoclinic space group, while the other five $LnGa_4$-2 crystallize in the P4nc one (Figure 2.4), showing a higher symmetry.

The overall 12-MC-4 assembly of these compounds consists of four Ga^{III} ions bridged by four Shi^{3-} ligands in a bowl-shaped scaffold. The central Ln^{III} ion is coordinated to the convex face of the macrocycle and is bridged to the central ring by four benzoate linkers. The overall formula of the complexes is: $\{Ln^{III}(OBz)_4[12\text{-}MC_{Ga^{III}(O)H3Shi\text{-}3H}\text{-}4]\}^{-1}$. As already mentioned, the

negative charge is balanced by a pyridinium counterion in case of the $DyGa_4$-1 compound, while the $LnGa_4$-2 complexes have a Na^I coordinated at the concave face of the MC-ring, the same as in the case of the $LnMn_4$ analogs (Figure 2.2, top-left).

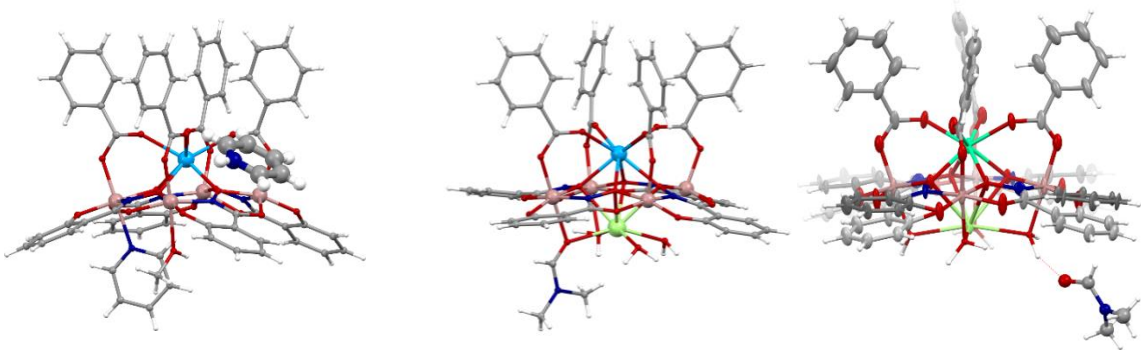

$DyGa_4$-1 $DyGa_4$-2 $HoGa_4$-2

(P21/c) (Pn) (P4nc)

Figure 2.4 X-Ray structures of: (**left**) $DyGa_4$-1 metallacrown, highlighting the HPy^+ counterion. A second Pyridine molecule is coordinated to one Ga^{III} at the concave face, together with a MeOH solvent molecule); (**center**) $DyGa_4$-2 polymorph, showing the Na^I ion coordinated to the concave face of the MC ring; (**right**) $HoGa_4$-2 molecular structure, represented by ellipsoid style to highlight the disorder along the C_4 axis, and of the aromatic rings of the ligands. The two disordered positions are respectively colored in light (60% occupancy) and dark (40% occupancy) grey. General color code: Dy-light blue, Ho-green, Na-light green, Ga-pink, O-red, N-blue C-grey and H-white.

From the crystallographic point of view, the two $DyGa_4$ compounds are characterized by a pseudo-C_4 axis due to not negligible distortions of the MC-ring. On the other hand, the other four $LnGa_4$-2 compounds show a higher crystallographic symmetry, that lead the molecule to be characterized by a C_4 crystallographic axis. These four Ln derivatives (i.e. Ln = Ho, Er, Lu and Y), whose space group is P4nc, show elongated thermal ellipsoids in the direction of the C_4 axis, which are represented in Figure 2.4 (right). This positional disorder affects especially the Shi^{3-}

ligands. Indeed, the Shi^{3-} aromatic rings were refined by splitting them in two main positions, which are respectively 60 and 40% occupied. The situation is represented in Figure 2.4 (right) for the Ho derivative by coloring the 60% occupied positions in light grey and the 40% occupied positions in dark grey.

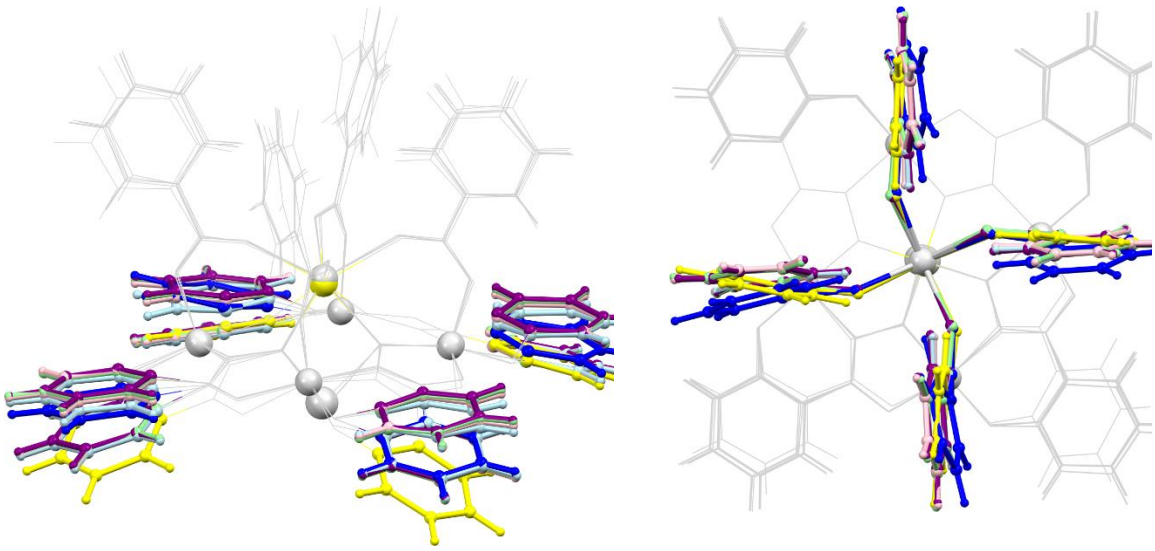

Figure 2.5 Overlay of the 6 crystal structures of the $LnGa_4$ complexes: $DyGa_4$-1 (yellow), $DyGa_4$-2 (blue), $LnGa_4$-1 (Ln = Ho (light-blue), Er (light pink), Lu (purple) and Y(light green). The distortions and the positional disorder of the Shi^{3-} aromatic rings are highlighted in the representation on the left, while differences in the arrangement of the benzoate linkers are shown on the right.

The overlap of the 6 $LnGa_4$ crystal structures (Figure 2.5) results close to that of $LnMn_4$; indeed, the cores of the metallacrown cycle (i.e. metal ions and heteroatoms) perfectly match, while in the periphery are accounted small distortions of the aromatic rings and benzoates linkers. These differences, which occur at the periphery of the architecture will be taken into account, later, to discuss the interpretation of NMR data.

The graphical observations are supported by the evaluation of the following distances: (I) the Ln-O_{ox} mean plane, (II) the Ln-Mn mean plane, (III) the O_{ac}-Ln bond lengths, and (IV) the

bowing terms. Overall these measurements are listed in Table S4 (Chapter 2, Supplementary materials). A careful analysis of these parameters allows to conclude that by changing the lanthanide ion from Dy to Lu in $LnGa_4$-2, no consistent variation of the distances takes place. The only significant change can be accounted by considering the $DyGa_4$-1 structure versus the $DyGa_4$-2 one and, as already found for the $LnMn_4$ spices, can be ascribed to the coordination of the Na^I ion, which bring the MC-ring more planar.

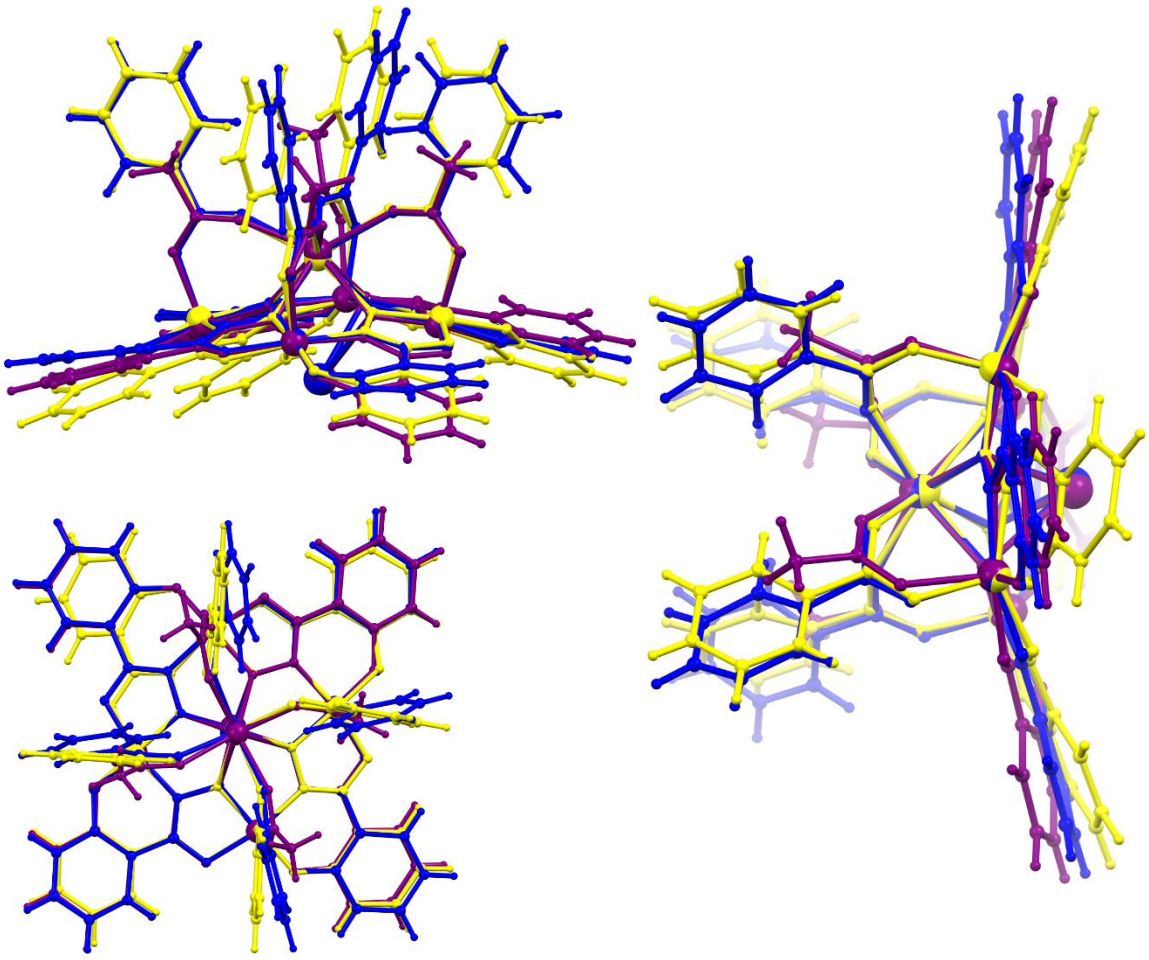

Figure 2.6 Overlay of the $DyMn_4$ (purple), the $DyGa_4$-1 (yellow) and the $DyGa_4$-2 (blue) X-Ray crystal structures. Despite the architecture is the same, and that the positions of both metal ions and heteroatoms perfectly match, the peripheries do not match completely and in particular the vacant coordination site at the underside of the cavity of Dy-Ga_4-1, result in a more domed MC-scaffold.

Finally, the overlay reported in Figure 2.6 shows the comparison between the $DyMn_4$ (purple), the $DyGa_4$-1 (yellow) and the $DyGa_4$-2 (blue) crystal structures, remarking that the absence of the counterion to the underside of the MC-ring result in the more domed scaffold of the $DyGa_4$-1 complex.

2.2. ^{1}H NMR studies

Monodimensional ^{1}H-NMR in deuterated methanol (CD_3OD) of the twelve $LnMn_4$ complexes, and monodimensional and bidimensional ^{1}H-NMR in deuterated dimethylsulfuxide (DMSO d_6) of the 13 $LnGa_4$-2 compounds were collected. In the case of both the $LnMn_4$ and the $LnGa_4$-2 series of molecules, ^{1}H-NMR signals are in general sharp enough to discuss their positions and integrals. As mentioned before, this was actually expected for both manganese(III) and lanthanides(III) derivatives, since are both known as paramagnetic nuclei, that allow high resolution NMR experiments, thanks to their short electronic relaxation times (except Gd^{III}).[21]

As already anticipated, the ^{1}H NMR analysis of these compounds allowed to investigate the structure of these molecules in solution and to compare it with those in the solid state.

2.2.1 General description of the ^{1}H NMR spectra of $LnMn_4$

Due to the diamagnetic nature of the encapsulated metal, the monodimensional ^{1}H NMR spectrum of YMn_4 was collected first (Figure 2.7). In this spectrum, besides the solvent signals (i.e. DMF at 2.86, 2.99, 7.97 ppm; MeOH at 3.31 ppm; and H_2O at 4.87 ppm) five relatively broad resonances are present: four of them at +10.4, -24.3, -20.6, and -16.9 ppm (resonances 1-4) account for one proton each, and have been assigned to the four protons of the Shi^{3-} ligands (labelled as A-D, Figure 2.7, right). Conversely, the broader signal at +27.9 ppm (Me),

has been assigned to the acetate methyl group, which has an integral three times higher than the former one.

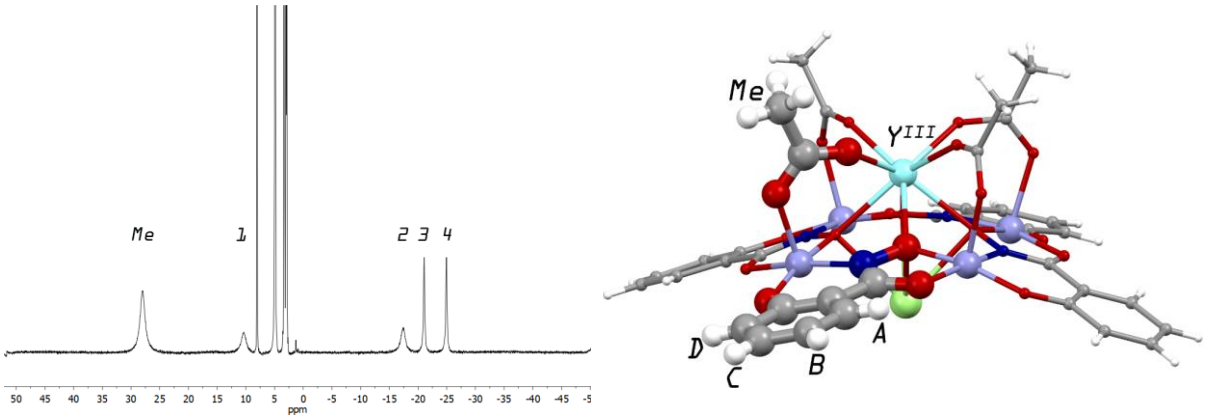

Figure 2.7 ^{1}H-NMR spectrum of the YMn_4 species in CD_3OD. Inset: molecular structure of YMn_4. The NMR resonances are labelled with numbers, while protons in the structure are indicated with letters. Non-labelled resonances are related to DMF and solvents.

Beside the distortions of the intrinsic 4-fold symmetry typical for 12-MC-4 complexes, which was found in the crystal structure of the YMn_4 molecule (Figure 2.2) and the absence of a C_4 crystallographic symmetry element, the NMR pattern is consistent with the presence of an actual 4-fold axial symmetry of the complex. Therefore, the NMR data suggest that on the NMR time scale the complex presents an average C_4 symmetry in solution. This is probably due to small structural rearrangements and possible fluxionality, that take probably place in solution. The NMR data are also consistent with (I) the integrity of the MC scaffold in solution, (II) the encapsulation of the Ln^{III} ion, and (III) the presence of coordinated acetate ions. However, no information is provided either on the presence of a coordinated sodium ion on the concave face of the metallacrown, or conversely on its possible dissociation.

The monodimensional ^{1}H-NMR spectra for $LnMn_4$ (where Ln stays for Y, Pr, Nd, Sm, Eu, Gd, Tb, Dy, Ho, Er, Tm, Yb) are reported in Figure 2.8. The pattern of the resonances observed for the YMn_4 is in general maintained along the overall Ln^{III} series. All the spectra present a broad 3-protons resonance in the +15 to +45 ppm region attributed to the methyl groups of the four equivalent acetate linkers (Me resonances).

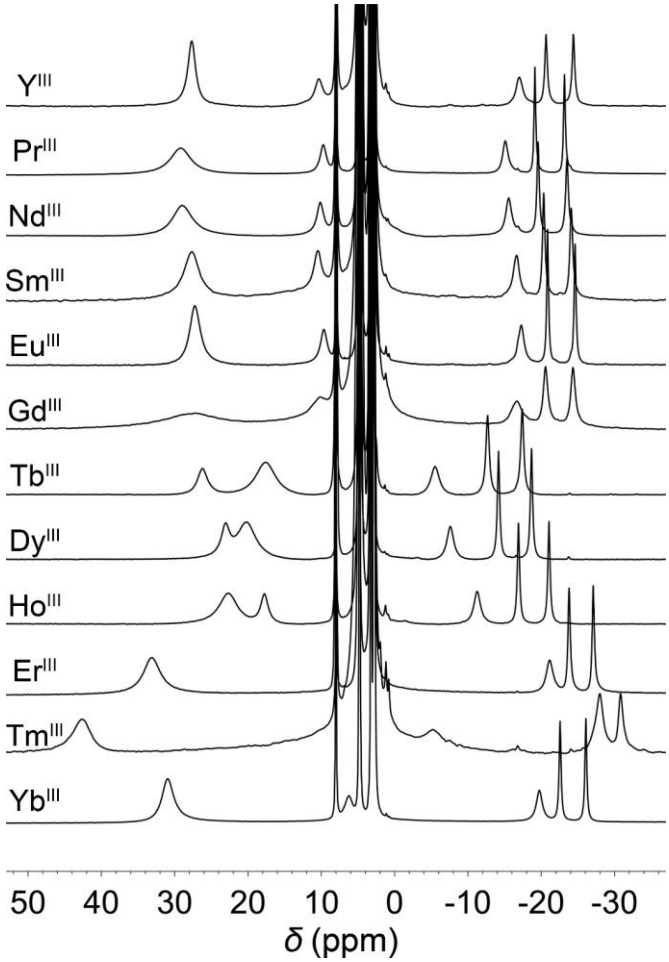

Figure 2.8 ^{1}H-NMR spectra of the twelve heterobimetallic $LnMn_4$ in CD_3OD. The encapsulated Ln^{III} ion is indicated on the left. All spectra were recorded in CD_3OD at 298.2 K

Three narrower Shi^{3-} resonances (marked 2-4 in Figure 2.7, and integrating 1 proton each) are found in the -5 to -30 ppm region. The $TmMn_4$ is an exception as in the latter region it presents one signal accounting for 2 protons and one resonance accounting for 1 proton. Resonance 1 (Figure 2.7) is significantly broad in all spectra and spans from -5 (Tm^{III}) to +27

ppm (Tb^{III}) depending on the $LnMn_4$. In the $ErMn_4$ spectrum, this resonance 1 of the Shi^{3-} signal is not observed, because it is covered by the solvent signals.

Looking at the complete Pr-Yb series of spectra (and at YMn_4), two relevant observations can be done. First, the line broadening brought about by Mn^{III} was in the low boundary for this paramagnetic cation,[21,48–51] and the paramagnetic shift was reasonably large even in the YMn_4 compound. An extended magnetic coupling between the paramagnetic ions in the $[Mn^{III}]_4$ system is expected to be at the origin of the significantly narrow signals in the spectrum of YMn_4.

Second, a well resolved spectrum of the $Gd^{III}Na^{I}(OAc)_4[12\text{-}MC_{Mn^{III}(O)H3Shi\text{-}3H}\text{-}4]$ complex was recorded. The spectrum displays an unprecedented observation in a small-sized Gd^{III} complex, of the ligand (acetate and shi^{3-}) proton resonances only slightly broader than the other Ln^{III} ions. The electronic relaxation time (τ_e) of Gd^{III}, which is usually reported in the 10^{-8}-10^{-9} s range,[52–57] is expected to become considerably shorter (down to 10^{-10} s, vide Table S5, Chapter 2, Supplementary Material) due to the coupling with the Mn^{III} ions active at room temperature. These aspects are elucidated in the literature, [58] while here are simply recalled those conclusions, following which it is possible to include the Gd^{III} compound in the "*all lanthanides*" data treatment.

The signals in the first six spectra of Figure 2.8 (Y-$GdMn_4$) are closely similar in terms of chemical shifts, although with visible differences in terms of signal broadening. The spectra of the heavier lanthanides (Dy-$YbMn_4$) exhibit markedly different chemical shifts with respect to those observed for the light lanthanides, with signals shifted up to 15 ppm with respect to YMn_4. The largest shifts with respect to the signals of YGa_4 were observed in the spectrum of

$TmMn_4$, which also presents two Shi^{3-} signals overlapped (signals 2 and 3, at ca. -27 ppm). A similar situation is observed in the spectrum of $DyMn_4$ where the Me and 1 resonances are partially overlapped (ca. +18 to +24 ppm). For both compounds the chemical shift of the overlapped signals were obtained by deconvolution of the spectrum using the MestReNova program (Figure S1, Chapter 2, Supplementary Materials).[59]

The remarkably different chemical shift shown by the heavier lanthanides, compared with that of the light one is actually not surprising and well known in literature under the name of *"Gadolinium break"*, [60] Despite these differences, overall these spectra are consistent with the presence of a stable, undissociated 4-fold symmetrical MC scaffold in solution.

2.2.2 Determination of the lanthanide induced shift (LIS_{Ln})

Since all the spectral features shown through the analysis of Figure 2.8 are consistent with the integrity of the $\{Ln^{III}(OAc)_4[12\text{-}MC_{Mn^{III}(O)H3Shi\text{-}3H}\text{-}4]\}^{-1}$ complexes, the LIS_{Ln} was calculated. Both Ln^{III} and Mn^{III} are paramagnetic ions and should be treated as coupled systems. However, even a quick look to the spectra gives rise to the idea that the paramagnetic contribution to the chemical shifts (δ^{para}) is dominated by that of the Mn_4 system, whose predominant effect is evident in the YMn_4 spectrum (note the Y^{III} is diamagnetic, hence no lanthanide paramagnetic effect affects its chemical shift), while the contribution of the Ln^{III} are second order perturbations. These MC complexes can, then, be described as the overlap of two independent paramagnetic systems, namely the *$[Mn^{III}]_4$ system* of the scaffold, and the *Ln^{III} system* within the cavity. This procedure for the treatment of such type of data has been previously used in the literature for the study of complexes with two different paramagnetic centers, one of which is Ln^{III}.[61] The overall paramagnetic shift experienced by a proton (δ^{para}) can be therefore described

as the sum of the paramagnetic shift operated by the two independent spin centers δ^{para}_{Mn} and δ^{para}_{Ln}. Thus, the δ^{obs} defined in eqn. 1.1, becomes as reported in eqn. 2.1, where the term δ^{para}_{Ln} consist in the Lanthanide Induced Shift (LIS_{Ln}):

$$\delta^{obs} = \delta^{dia} + \delta^{para} \quad (1.1)$$

$$\delta^{obs} = \delta^{dia} + \delta^{para}_{Mn} + LIS_{Ln} \quad (2.1)$$

The chemical shift experienced by the protons of the YMn_4 complex (δ^{obs}_{Y}), is therefore:

$$\delta^{obs}_{Y} = \delta^{dia} + \delta^{para}_{Mn} \quad (2.2)$$

Since the compounds in this series are isostructural, the paramagnetic contribution to the shift due to the $[Mn^{III}]_4$ system is expected to remain reasonably constant. Thus, the LIS_{Ln} can be calculated for each **i** proton of each $LnMn_4$ spectra as follows:

$$LIS_{Ln}(i) = \delta^{obs}_{Ln}(i) - (\delta^{dia} + \delta^{para}_{Mn}) \approx \delta^{obs}_{Ln}(i) - \delta^{obs}_{Y}(i) \quad (2.3)$$

The eqn. 2.3 highlights how this data treatment considers the LIS_{Ln} as a perturbation to the paramagnetic shift provided by the $[Mn^{III}]_4$ system, which is considered predominant and constant along the $LnMn_4$ series. The complete list of $\delta^{obs}_{Ln}(i)$ and LIS_{Ln} are reported in Table 2.1 here below. The numbering of the proton signals follows the labelling reported in Figure 2.7. The signal marked by [a] is not observed since it falls in the diamagnetic (0-10 ppm) range, and therefore is covered by the solvent signals. The resonances values marked by * are the result of the deconvolutions mentioned before and whose spectra are reported in Figures S1, (Chapter 2 Supplementary Materials).

Table 2.1 Observed chemical shift and calculated LIS_{Ln} related to the spectra reported in Figure 2.8

$LnMn_4$	δ^{obs}_{Ln} | $LIS_{Ln}(i)$									
	Me		H1		H2		H3		H4	
Y	27.79	-	10.51	-	-16.92	-	-20.56	-	-24.3	-
Pr	29.25	*1.46*	9.79	*-0.72*	-15.02	*1.89*	-19.06	*1.49*	-23.1	*1.19*
Nd	29.09	*1.3*	10.17	*-0.35*	-15.54	*1.37*	-19.56	*0.99*	-23.5	*0.77*
Sm	27.67	*-0.13*	10.55	*0.04*	-16.6	*0.31*	-20.23	*0.32*	-24	*0.29*
Eu	27.38	*-0.41*	9.77	*-0.75*	-17.19	*-0.27*	-20.77	*-0.2*	-24.5	*-0.2*
Gd	27.56	*-0.24*	10.33	*-0.18*	-16.69	*0.22*	-20.5	*0.05*	-24.3	*0.03*
Tb	17.67	*-10.1*	26.22	*15.7*	-5.47	*11.44*	-12.65	*7.91*	-17.4	*6.91*
Dy	20.23*	*-7.56*	23.02*	*12.5*	-7.63	*9.29*	-14.19	*6.36*	-18.7	*5.6*
Ho	22.77	*-5.02*	17.83	*7.32*	-11.19	*5.73*	-16.82	*3.74*	-21	*3.31*
Er	33.1	*5.31*	ND[a]	*ND*[a]	-21.14	*-4.23*	-23.79	*-3.2*	-27.1	*-2.8*
Tm	42.8	*15.01*	-5.09	*-15.6*	-27.42*	*-10.5*	-27.94*	*-7.4*	-30.7	*-6.5*
Yb	31.06	*3.27*	6.33	*-4.18*	-19.62	*-2.71*	-22.46	*-1.9*	-26	*-1.7*

2.2.3 Determination of the Fermi contact (δ^{FC}_{Ln}) and Pseudocontact (δ^{PC}_{Ln}) contribution to the LIS_{Ln}, using the "*all lanthanides*" method

The Fermi contact and pseudocontact contributions were determined using the "*all lanthanides*" method, whose steps were listed and discussed in detail in Paragraph 1.3.3. Once the $YbMn_4$ was selected as reference compound and the δ^{FC}_{Ln} contribution was considered negligible, the *plot-I* was determined (Figure2.9). The *plot-I* displays the $LIS_{Ln}(i)$ of each **i** proton versus the respective $LIS_{Yb}(i)$. Overall the $LnMn_4$ were investigated. However, the linear trend is more evident for heavier lanthanides. The straight lines reported in the plot (Figure 2.9) are the best fit of the experimental data, which result from the linear regression (forced through the origin) The slopes of these lines are indicated as m_{Ln} and are reported in Table 2.2.

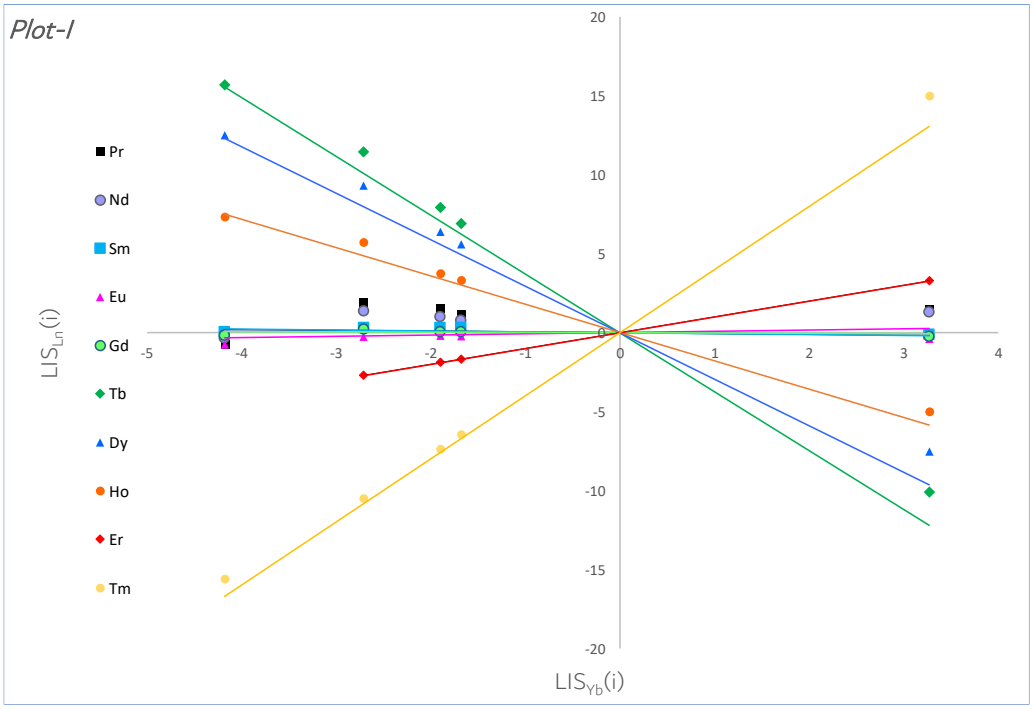

Figure 2.9 "*All lanthanides*" calculations, *Plot-I*. The graph displays the $LIS_{Ln}(i)$ values versus the related $LIS_{Yb}(i)$. All the calculated $LIS_{Ln}(i)$ were considered. The best fit was traced as straight lines, as a result of the linear regression forced through the origin.

It can be demonstrated that the m_{Ln} values are proportional to the anisotropy of the magnetic susceptibility tensor, which is expected to be larger for the heavier lanthanides, as here observed.

Table 2.2 m_{Ln} slope values fot the $LnMn_4$ complexes, related to the *plot-I*

$LnMn_4$	Pr	Nd	Sm	Eu	Gd	Tb	Dy	Ho	Er	Tm	Yb
m_{Ln}	-0.05 (8)	-0.03 (3)	-0.06 (3)	0.08 (6)	-0.02 (2)	-3.7 (2)	-2.9 (2)	-1.79 (10)	1.62 (3)	4.00 (18)	1
R^2	0.011	0.006	0.512	0.332	0.124	0.984	0.981	0.987	0.999	0.992	1

In addition, m_{Ln} is expected to be positive for prolate lanthanide ions, negative for oblate ones and consistent with the slopes of *Plot-I*. In particular, if (I) the complexes are strictly isostructural, (II) the overall Ln^{III} ions experience the same crystal field splitting effect (B_{Ln}), and

(III) the $\delta^{PC}_{Ln}(i)$ term is predominant over the $\delta^{FC}_{Ln}(i)$ one, then the m_{Ln} parameter would ideally reduce to the $C_i(Ln)/C_i(Yb)$ ratio of the Bleaney's constants, within the limits of validity of the Bleaney's theory mentioned in Paragraph 1.3.2 and detailed elsewhere [20,62] This explains why the slopes are larger for heavier lanthanides than for lighter ones, as the lanthanides within Tb^{III}-Yb^{III} have larger Bleaney's constants (Table S1, Chapter 2, Supplementary Materials).[63]

The standard deviations of m_{Ln} and the R^2 values, reported in Table 2.2, demonstrate that deviations from the linearity in *plots-I* are experienced by the lighter lanthanides for which a small $LIS_{Ln}(i)$ is observed. This behavior is accounted for a non-negligible Fermi contact $\delta^{FC}_{Ln}(i)$ contribution which affects in particular the Shi^{3-} resonances. As a consequence, the determination of the m_{Ln} values with statistical significance could not be carried out for the Pr^{III}-Eu^{III} series. Thus, the *plot-II* was drawn only for the heavier lanthanides (Gd^{III}-Yb^{III}) and the $\delta^{PC}_{Ln}(i)$, $\delta^{FC}_{Ln}(i)$ contributions were calculated. The different behavior of the heavier lanthanides (i.e. Gd-Yb), compared with that of the lighter (Pr-Eu) is not surprising and it is often found in literature under the name of *"Gadolinium break"*.

The *plot-II* reports the $LIS_{Ln}(i)/\langle S_z\rangle_{Ln}$ values as a function of $m_{Ln}/\langle S_z\rangle_{Ln}$. and straight lines were obtained from the linear regression of the data. (Figure 2.10)

The slopes (M(i)) and the intercepts (Q(i)) were calculated, the values are reported in. Table 2.3. It is worth noting here that to each proton, a M(i) value can be calculated. These M(i) values will be used here below to provide the assignments of the resonances to the different protons of the Gd-$YbMn_4$ complexes.

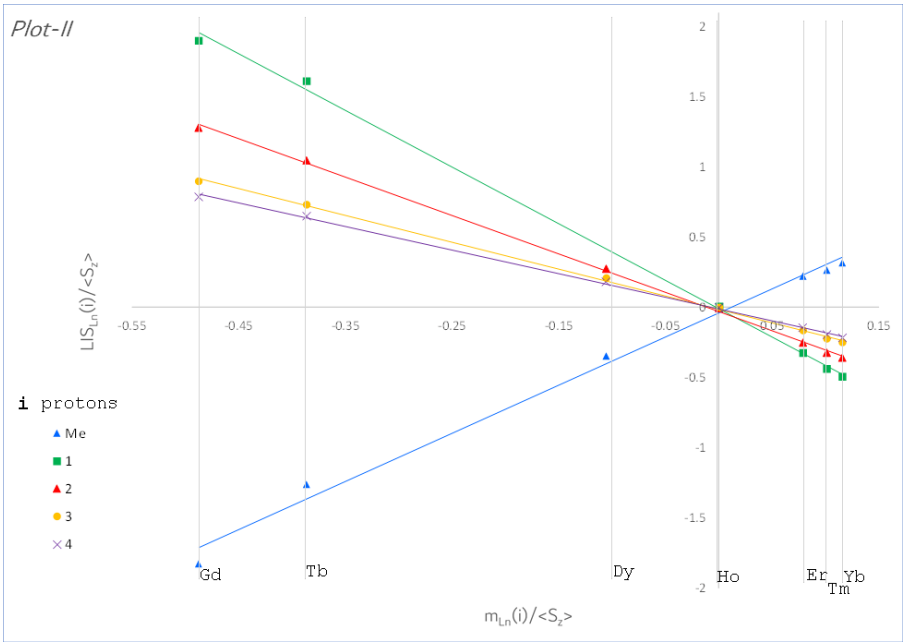

Figure 2.10 *"All lanthanides"* calculations, *Plot-II*. The graph displays the $\delta^{para}_{Ln}(i)/\langle S_z\rangle_{Ln}$ for each lanthanide versus the $m_{Ln}/\langle S_z\rangle_{Ln}$ ratio. Only the Gd-YbMn$_4$ derivatives of where considered.

Table 2.3 Slopes, Intercept and R^2 values related to the *Plot-II*, **Figure 2.10**

	M(i)	Q(i)	R^2
Me	3.4(1)	-0.07(3)	0.992
H1	-0.6(2)	0.01(2)	0.722
H2	-2.74(3)	-0.01(2)	0.999
H3	-1.91(3)	-0.00(2)	0.999
H4	-1.68(3)	-0.00(2)	0.999

Finally, the calculations of the fourth step of the "*all lanthanides*" method were done and the $\delta^{PC}_{Ln}(i)$ contributions were determined for the Gd-YbMn$_4$ complexes, through the eqns. 1.12-13, discussed in Paragraph 1.3.3 and here below recalled for clarity.

$$M(i) = \delta^{PC}_{Yb} \quad (1.12)$$

$$m_{Ln} \times M(i) = \delta^{PC}_{Ln} \quad (1.13)$$

$$Q(i) \times (S_z)_{Ln} = \delta^{FC}_{Ln} \quad (1.14)$$

As far as it concerns the $\delta^{FC}_{Ln}(i)$ contributions, it has to be noticed that the intercepts Q(i) can't be determined with significant precision. (see Table 2.3) Under these circumstances the $\delta^{FC}_{Ln}(i)$ parameters can be better estimated, rather than from eqn. 1.14, but by subtraction of the $\delta^{PC}_{Ln}(i)$ from the the $LIS_{Ln}(i)$ values as follows:

$$\delta^{FC}_{Ln}(i) = LIS_{Ln}(i) - \delta^{PC}_{Ln}(i) \quad (3.4)$$

Table 2.4 $\delta^{PC}_{Ln}(i)$, $\delta^{FC}_{Ln}(i)$ and related standard deviations, calculated for the Gd-$YbMn_4$ complexes by means of the eqns. 1.12-13.

	Me		1		2		3		4	
	δ^{FC}_{Ln}	δ^{PC}_{Ln}	δ^{FC}_{Ln}	δ^{PC}_{Ln}	δ^{FC}_{Ln}	δ^{PC}_{Ln}	δ^{FC}_{Ln}	δ^{PC}_{Ln}	δ^{FC}_{Ln}	δ^{PC}_{Ln}
Gd	-0.17 (6)	-0.06 (6)	-0.25 (7)	0.07 (7)	0.17 (5)	0.05 (5)	0.02 (4)	0.04 (4)	0.00 (3)	0.03 (3)
Tb	2.65 (7)	-12.77 (7)	0.64 (6)	15.06 (6)	1.25 (7)	10.19 (7)	0.78 (7)	7.12 (7)	0.66 (7)	6.25 (7)
Dy	2.54 (8)	-10.10 (8)	0.60 (7)	11.91 (7)	1.23 (8)	8.06 (8)	0.73 (8)	5.63 (8)	0.65 (8)	4.94 (8)
Ho	1.12 (7)	-6.14 (7)	0.08 (6)	7.24 (6)	0.82 (7)	4.90 (7)	0.31 (7)	3.42 (7)	0.30 (7)	3.01 (7)
Er	-0.24 (4)	5.55 (4)	ND[a]	-6.54 (3)[b]	0.20 (4)	-4.43 (4)	-0.15 (5)	-3.09 (5)	-0.08 (5)	-2.71 (5)
Tm	1.32 (6)	13.69 (6)	0.54 (5)	-16.14 (5)	0.42 (6)	-10.93 (6)	0.25 (7)	-7.63 (7)	0.25 (7)	-6.70 (7)
Yb	-0.16 (4)	3.42 (4)	-0.14 (2)	-4.04 (2)	0.02 (4)	-2.73 (4)	0.01 (4)	-1.91 (4)	0.00 (4)	-1.68 (4)

[a] signal not visible, as covered by solvent resonances; [b] signal alculated through linear regression.

The overall values of $\delta^{PC}_{Ln}(i)$ and $\delta^{FC}_{Ln}(i)$ calculated for the Gd-$YbMn_4$ complexes by means of eqns. 1.12-13 and 3.4, respectively, are reported here below in Table 2.4

2.2.4 Correlation of the crystal structures with the information in solution: assignments of ^{1}H NMR resonances

The values of the $<G(i)_{XRD}>$ terms are reported for each **i** proton in Table 2.5. And represent the average values of the four geometrical terms $G(i)_{XRD}$ related to the same H(i) for the four shi^{3-} ligand forming each $LnMn_4$ molecule. These average values become statistically necessary, after the consideration, that the crystal data show the four Shi^{3-} ligands not being equivalent by symmetry. The $G(i)_{XRD}$ was calculated, for each Shi^{3-} proton, through the eqn. 1.6 as reported in Figure 1.14. For the sake of completeness, the average Ln-H distances (r_i) and angles (ϑ_i), defined in paragraph 1.3.2 and in Figure 1.14, of the Gd-$YbMn_4$ complexes are reported in Table S6 (Chapter 2, Supplementary Materials).

Table 2.5 G(i) terms and G(i)/G(j) ratios calculated for the H(A-D) protons from the r_i and ϑ_i values related to the X-Ray crystal structures of the $LnMn_4$ series.

$LnMn_4$	$<G(i)_{XRD}>$ (10^{20} cm^{-3})				$<G(i)_{XRD}>$ / $<G(B)^{XRD}>$			
	HA	HB	HC	HD	HA	HB	HC	HD
Gd	-9.64	-6.66	-8.16	-16.1	1.45		1.23	2.42
Tb	-10.2	-7.16	-8.22	-16.3	1.42		1.15	2.28
Dy	-9.89	-6.79	-8.29	-16.5	1.46		1.22	2.43
Ho	-10	-6.85	-8.35	-16.7	1.46	1	1.22	2.44
Er	-10	-6.86	-8.39	-16.7	1.46		1.22	2.43
Tm	-10.1	-6.91	-8.42	-16.8	1.46		1.22	2.43
Yb	-10.1	-6.89	-8.42	-16.9	1.47		1.22	2.45

The M(i) slopes (**i** = H1-H4, Figure 2.7, left) obtained from the "*all lanthanides*" method, and the $<G(i)_{XRD}>$ terms (**i** = HA-HD, Figure 2.7, right) calculated from the crystal structures, both referred to the Shi^{3-} protons, were used to confirm and support the assignment of the resonances in the ^{1}H NMR spectrum as described in paragraph 1.3.4 and previously reported in

literature.[30] The M(i)/M(j) ratios were calculated, where M(j) is the smallest slope found from *plot-II* (vide Figure 2.10 and Table 2.3). The resulting values were compared to those obtained from the $<G(i)_{XRD}>/<G(j)_{XRD}>$ ratios.

Table 2.6 The M(i)/M(j) for the H1-4 resonances and the correlations with the related H(A-D) protons.

correlation | assignements	$H(i)_{Shi3}$-		
	$M(i)_n$	M(i)/M(4)	$<G(i)_{XRD}>$
	H1	2.4	*HD*
	H2	1.6	*HA*
	H3	1.1	*HC*
	H4	1	*HB*

By comparing the $<G(i)_{XRD}>/<G(j)_{XRD}>$ parameters obtained from the X-Ray crystal structure with the M(i)/M(4) parameters, obtained from the NMR data and related with the structure in solution (vide $G(i)_{NMR}$ definition in eqn 1.8 and its application in eqn. 1.10) we could unambiguously assign the NMR resonances to the four Shi^{3-} protons. These assignments are in agreement with those reported in the literature for similar [12-$MC_{Mn^{III}(O)H3Shi-3H}$-4] scaffolds encapsulating Na^{I}, Li^{I}, K^{I} or Mn^{II} in their cavities.[30] Very interesting is that, contrary to what reported in literature, these assignments have been carried out without any *a-priori* assumption based on the resonances of the previously known 12-MC-4 species. Rather, the approach here applied was based solely on the evaluation of the Lanthanide Induced Shifts. Therefore the assignments reported in Table 2.6 represent a proof of consistency of the present applied method and of the hypothesis, on which it stands.

2.2.5 General description of the ^{1}H NMR spectra of $LnGa_4$-2

The $LnGa_4$-2 series was analyzed and treated, by applying the same procedure of the $LnMn_4$ one. Hence the monodimensional ^{1}H NMR spectrum of YGa_4-2 and $LuGa_4$-2 (Figure 2.11) were collected, as purely diamagnetic compounds. We report here both the Y and Lu ^{1}H NMR spectra, to demonstrate the correspondence between the two set of signals, however, for the sake of consistency, the Y derivative was considered as diamagnetic reference.

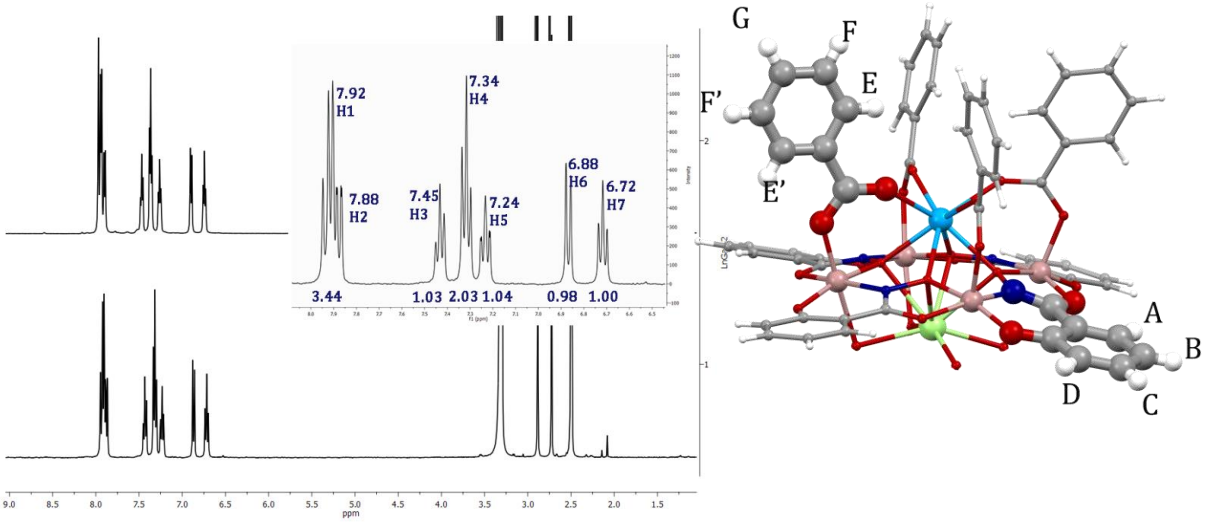

Figure 2.11 ^{1}H-NMR spectra of the YGa_4-2 and Lu Ga_4-2 species in DMSO-d_6. Inset: expansion of the 6-8.5 ppm area of the YGa_4-2 spectrum, where are marked chemical shifts and integrals. The molecular structure of YGa_4-2 is reported on the right. NMR resonances are labelled with numbers, while protons of the structure are indicated with letters. Resonances in the 2-4 ppm range are related to DMF and solvents.

The Y ans Lu - Ga_4-2 spectra present seven narrow resonances, besides the solvent signals (i.e. DMF at 2.73, 2.89, 7.97 ppm; H_2O at 3.33 ppm; and DMSO at 2.50 ppm). The overall resonances were assigned by taking into account: (I) signals multiplicity, (II) integrals analysis

and (III) the bidimensional COSY spectrum, that was collected for the YGa_4-2 compound and is reported in Figure S2 (Chapter 2, Supporting Materials).

The resonances at 7.95, 7.92 and 7.88 ppm (signals $H_{DMF,}$ H1 and H2) were integrated together and, thanks to their multiplicity and the bidimensional COSY spectrum, were assigned respectively to the DMF amidic proton (i.e. 7.95 ppm), to the benzoate HE (7.92 ppm) and to the shi^{3-} HA (7.88 ppm) protons. The H6 signal (7.34 ppm) was assigned to HF (benzoate), thanks to its integral value. Finally, the analysis of the COSY couplings allowed to distinguish between the remaining signals: the one at 7.44 ppm was assigned to HG (benzoate) and the resonances at 7.24, 6.88, 6.72 ppm was attributed respectively to the C, D, B protons (Shi^{3-}).

The seven resonances, their multiplicity, the integral values and the assignments related to Figure 2.11 are summarized for YGa_4-2 in Table 2.7. From the left to the right of the spectrum, the sequence of the 1-7 signals results: E, A, G, F, C, D, B, C. This 1-7 sequence of resonances will be referred further on in lowercase (i.e. e-a-g-f-c-d-b-c).

Table 2.7 ^{1}H NMR data of the YGa_4-2 diamagnetic reference compound

$Labels^{NMR}$	H_{dmf}	H1	H2	H3	H4	H5	H6	H7
δ^{oss} (ppm)	7.95	7.92	7.88	7.45	7.34	7.24	6.88	6.72
multiplicity	s	d	dd	t	t	dt	d	t
Integrals	3.56			1.03	2.04	1.04	0.98	1.00
$Labels^{XRD}$	DMF	E	A	G	F	C	D	B

Both the Y and Lu -Ga_4-2 ^{1}H NMR patterns are consistent with the presence of a 4-fold axial symmetry related to the molecular structure of the complexes. Moreover, the resonances referred to the Shi^{3-} ligand are characterized by narrow linewidth (c.ca. 20 Hz), suggesting that

the disorder of the peripheral aromatic rings, accounted in the solid state (vide **Figure 2.4**) should correspond to a fluxionality in solution, which is fast compared with the NMR times scale. Overall these spectral features are also consistent with the integrity of the MC scaffold in solution, the encapsulation of the Ln^{III}, and the presence of four coordinated benzoate ions. However, like for $LnMn_4$, no information is provided either on the presence of a coordinated sodium ion on the concave face of the metallacrown, or conversely on its possible dissociation.

Finally, the the correspondence between the two set of signals in Y and Lu -Ga_4-2 derivatives, demonstrate, the two molecular structures in solution are isostructural.

The monodimensional ^{1}H-NMR spectra of the $LnGa_4$-2 (where Ln stays for Y, La, Pr, Nd, Sm, Eu, Gd, Tb, Dy, Ho, Er, Tm, Yb and Lu) are reported in Figure S3 (Chapter 2, Supporting Materials), the visualization in stack is reported in Figure 2.12. Here the weak signals were enhanced and marked by a grey star, in addition the resonances of the solvents (except that of DMF at 7.95 ppm) were omitted for clarity.

The observed chemical shifts related to the spectra are reported in **Table 2.8**. Looking at the complete series of spectra, it is possible to observe what follows: first and unlike the $LnMn_4$ compounds, the pattern of the resonances of those of the $LnGa_4$-2, which are paramagnetic (i.e. for Ln = Pr, Nd, Sm, Eu, Gd, Tb, Dy, Ho, Er, Tm, Yb), are extremely different than those of the three diamagnetic compounds (i.e. YGa_4-2, $LuGa_4$-2 and $LaGa_4$-2). This is not surprising, and even more is a confirmation, that the LIS_{Ln}, in the $LnMn_4$ series, is a perturbation of the predominant paramagnetic effect induced by the $[Mn^{III}]_4$ paramagnetic system, while in the case of $LnGa_4$-2, the LIS_{Ln} is the only paramagnetic contribution to the observed chemical shift. Second, the presence of a predominant $[Mn^{III}]_4$ paramagnetic system allowed to be able to

collect an informative $GdMn_4$ spectrum, while the spectrum of the $Gd^{III}Na^{I}(OBz)_4$[12-$MC_{Ga^{III}(O)H3Shi-3H}$-4] complex, reported both in **Figure 2.12** and in Figure S3 (Chapter 2, Supplementary Materials), displays only a large broaden band in the 5-10 ppm region. This means that in case of $GdGa_4$-2, the protons of the metallacrown, which contains only the Gd paramagnetic system, experience the expected relaxation effects traditionally induced by the Gd^{III} ion and that commonly prevents the observation of the NMR signals.

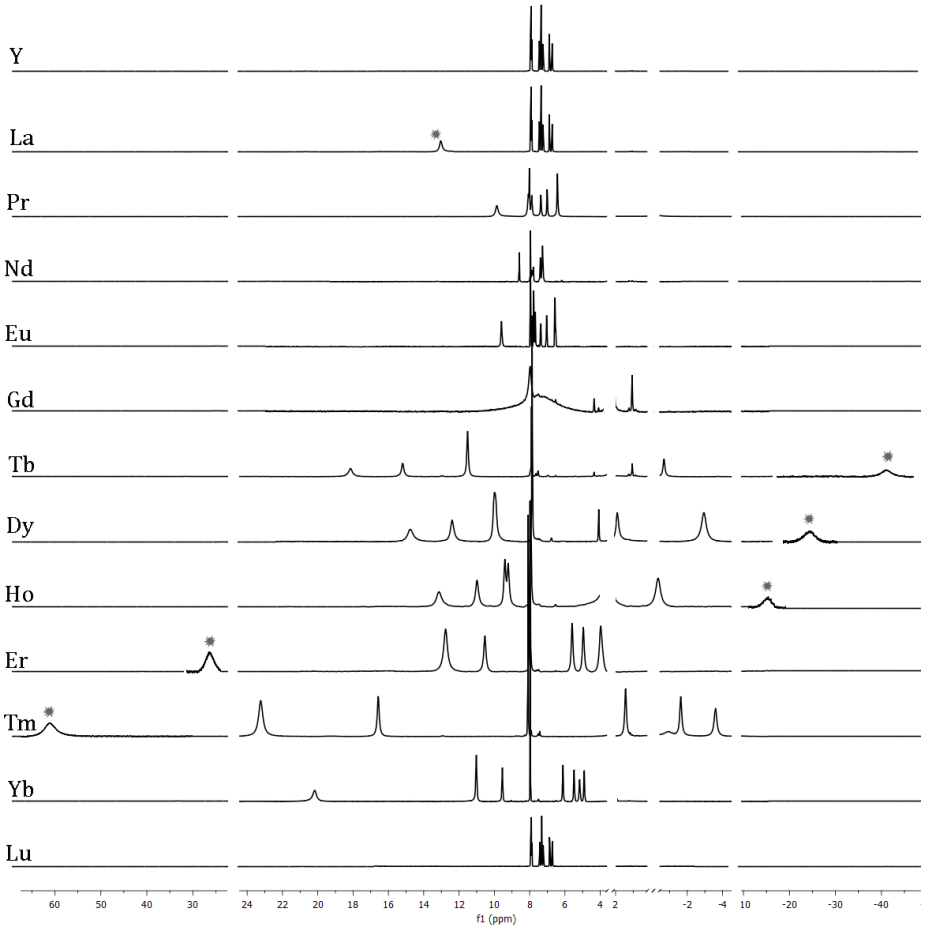

Figure 2.12 Spectra of the 13 heterometallic $LnGa_4$-2 (where Ln stays for Y, La, Pr, Nd, Eu, Gd, Tb, Dy, Ho, Er, Tm, Yb and LU) collected in DMSO-d_6 at 298 K. The encapsulated Ln^{III} ion is indicated on the left. Solvent signals and regions without resonances were omitted for clarity. Grey stars highlight the broaden resonances, whom intensities were enhanced to be better visualized.

Table 2.8 δ^{oss}(i) observed chemical shift, integrals and multiplicity of the Y, La-Lu series of $LnGa_4$-2 derivatives (except Pm and Sm)

$LnGa_4$-2	Observed chemical shift δ^{oss}(i), integral and multiplicity						
Y	7.92 (2H, d)	7.88 (1H, d)	7.45 (1H, t)	7.34 (2H, t)	7.24 (1H, t)	6.88 (1H, d)	6.72 (1H, t)
La	12.95[i] 10%	7.97 (3H, m)[b]	7.82 (1H, d)	7.52 (1H, t)	7.37 (2H, t)	7.23 (1H, t)	6.86 (1H, d)	6.69 (1H, t)
Lu	7.92 (2H, d)	7.87 (1H, dd)	7.44 (1H, t)	7.32 (2H, t)	7.24 (1H, dt)	6.88 (1H, d)	6.72 (1H, t)
Pr	9.86 (2H, s)	7.89-8.07 [c] (4H, m)	7.36 (1H, s)	7.01 (1H, s)	6.43 (2H, s)		
Nd	8.59 (1H, s)		7.79-7.95 [c] (3H, m)		7.27-7.39 [c] (4H, m)		
Eu	9.59 (2H, s)	7.77 (2H, t)	7.68 (1H, t)	7.38 (1H, d)	7.04 (1H, t)	6.53-6.59 [c] (2H, m)	
Tb	18.14 (1H, s)	15.19 (1H, s)	11.52 (2H, s)	-0.68 (1H, s)	-7.81[e] (2H, s)	-41.6 [d]	
Dy	14.75 (1H, s)	12.40 (1H, s)	10.00 (2H, s)	1.90 (1H, s)	-2.94 (2H)[e]	-25.22 [d]	
Ho	13.14 (1H, s)	10.98 (1H, s)	9.40 (1H, s)	9.22 (1H, s)	-0.14 (2H)[e]	-16.43 [d]	
Er	26.45 [d]	12.76 (2H, s)	10.53 (1H, s)	5.59 (1H, s)	4.96 (1H, s)	3.98 (2H, s)	
Tm	61.01 [d]	23.23 (2H, s)	16.57 (1H, s)	1.43 (1H, s)	-0.91 (1H, s)	-1.61 (1H, s)	-3.60 (1H, s)
Yb	20.17 [d]	11.02 (2H, s)	9.55 (1H, s)	6.11 (1H, s)	5.48 (1H, s)	5.17 (1H, s)	4.92 (1H, s)

Notes: [a] small signals related to 10% impurity within the sample; [b] the signal integrate 3H and is overlapped to that of the DMF, which is expected to have a 7.95 ppm chemical shift; [c] multiplet, multiple integration; [d] broaden signals, which were considered integrating for 2 H; [e] the signal integrate 2H, is considered the overlap of 2 resonances; [i] impurities; the % is reported as well.

Despite the presence of the lanthanide and the absence of an additional and predominant paramagnetic system (like in the case of the $LnMn_4$ series), overall the Ga-compounds (except $GdGa_4$-2) show narrow signals and some of them are enough resolved to see the resonances multiplicity (e.g $EuGa_4$-2). As far as it concerns the $LaGa_4$, $NdGa_4$ and $SmGa_4$ compounds the

spectra were collected and are reported in Figure S3 (Chapter 2, Supplementary Materials). However, the $LaGa_4$ spectrum shows two additional signals (19.94 and 7.61 ppm respectively) accounted to c.ca 10% of impurities, the $SmGa_4$ derivative was found impure as well and the spectrum of the Nd derivative is affected by a strong overlap of the resonances, which makes impossible an accurate analysis of integrals and chemical shifts. For these reasons $LaGa_4$-2, $SmGa_4$-2 and $NdGa_4$-2 compounds will not be included in any further data treatment.

The overall signals in the first seven spectra of Figure 2.12 (Y-$EuGa_4$-2) are closely similar in terms of both chemical shifts and bandwidth. Conversely, the spectra of the heavier lanthanides (Tb-$YbGa_4$-2) exhibit widely different chemical shifts and signals are shifted up to 50 ppm with respect to the diamagnetic reference. It is worth notice that the trend of the shift follows that of the Bleaney's constant (C_J) in terms of both sign and magnitude. That is more evident for the heavier lanthanides, thanks to their greater C_J constant. Hence, Tm has the greatest and positive constant and the spectrum account the larger chemical shift in the positive direction (+61.16 ppm). While Tb has the lower and negative C_J and the spectrum shows the larger shift in the negative direction (-41.6 ppm). These considerations allow to suggest the hypothesis that, at least for heavy Ln^{III}, the Fermi contact contribution is negligible. This anticipation will be demonstrated further on.

Beyond these considerations, the spectra of Pr^{III}, Tm^{III} and Yb^{III} derivatives show seven resonances; the $EuGa_4$-2 one shows five well resolved signals and one multiplet which is the overlap of two signals; the Tb, Ho, Dy, Er compounds present only six singlets, having two overlaid resonances , which appear as one slightly broaden signal. For the data treatment the latter $\delta^{oss}(i)$ values were counted twice with the same chemical shift (see Table 2.8). Beside

these observations and except for $GdGa_4$-2, whose spectrum is not informative, all the other NMR patterns are consistent with the presence of a stable, undissociated 4-fold symmetrical MC scaffolds in solution.

2.2.6 Determination of the lanthanide induced shift (LIS_{Ln})

The determination of the LIS_{Ln} was not as straightforward as in the case of $LnMn_4$. This is an effect of different joint reasons:

- the presence of the benzoate linkers instead of the acetate, results in three resonances rather than one and moreover one of those is related to a sole proton, like those related to the shi^{3-} ligand;

- the COSY spectra of the paramagnetic derivatives are not accessible as an effect of the enhanced relaxation time due to the unpaired electrons;

- the multiplicity of the signals is not everywhere retained;

- the lanthanide induces a chemical shift, which move the signals far away form the positions of the related diamagnetic reference.

As a consequence, the correlation of the $\delta^{oss}_{Ln}(i)$ with the correspondent δ^{dia}_{Y} (i) is not straightforward and some more considerations are necessary.

The LIS_{Ln} can be calculated through the enq. 1.3:

$$LIS_{Ln}\ (i) = \delta^{obs}_{Ln} - \delta^{dia}_{Y} \qquad (1.3)$$

If the δ^{FC}_{Ln} is negligible, the enq. 1.3 becomes as follow:

$$LIS_{Ln}(i) = \delta^{FC}(i) + \delta^{PC}(i) \sim \delta^{PC}(i) \quad (1.7)$$

$$LIS_{Ln}(i) \sim BC_J G(i)_{Ln} \quad (3.4)$$

Because the $LnGa_4$-2 complexes are isostructural, it means that for the same **i** proton the geometrical term G(i) of different Ln-complexes should have the same value. This means that the spectra along the series show different chemical shifts in terms of ppm values but the sequence ***i, j, k,*** … of the resonances is the same (i.e. from the left to the right the order of the signals related to the ***i, j, k,*** … protons is retained). As a consequence, the assignments of the resonances of one spectrum is enough to the determination of the overall LIS_{Ln}.

Table 2.9 $LIS_{Ln}(i)$ of the Pr-$YbGa_4$-2 derivatives. Those related to the benzoate linkers (i.e. e, f, g resonances) are underlined.

	Resonance	1	2	3	4	5	6	7
	$LnGa_4$-2	**$LIS_{Ln}(i)$**						
(-)C_J	**Pr**	3.14	0.19	0.83	1.01	-0.09	-0.33	-1.49
	Tb	11.42	7.31	4.28	4.64	-8.13	-15.15	-49.52
	Dy	8.03	4.52	2.76	3.12	-5.55	-10.28	-33.14
	Ho	6.42	3.1	3.74	2.52	1.77	-7.48	-24.35
(+)C_J	**Eu**	1.67	0.43	0.23	0.5	-0.2	-1.32	-0.18
	Er	18.5	5.42	3.08	-1.29	-2.28	-3.9	-2.74
	Tm	53.09	15.89	9.12	-5.45	-8.15	-9.51	-3.12
	Yb	12.25	3.68	2.1	-0.77	-1.76	-2.71	-1.8

The resonances were assigned for the $EuGa_4$-2 spectrum, for two reasons: first, the lanthanide induced shift is expected to be small, considering that both the C_J and the S_z values are small for Eu^{III}. Also, the spectrum shows well resolved signals, where the multiplicity is still visible. Thanks to the analysis of the integrals, multiplicity and the comparison of its spectrum

with the one of the diamagnetic reference (i.e. Y-Ga_4-2), the 1-7 (from the left to the right) resonances of the spectrum of $EuGa_4$-2 were correlated to the YGa_4-2 A-G protons. The 1-7 signals of the $EuGa_4$-2 spectrum were assigned as: e-f-g-d-c-a-b respectively. This sequence was used for the determination of the LIS_{Ln} of $EuGa_4$-2 and of the other $LnGa_4$-2 derivatives, having a positive C_J (i.e. Eu, Er, Tm, Yb). For those of the $LnGa_4$-2, where the Ln shows a negative C_J value (i.e. Pr, Tb, Dy, Ho), the sequence was mirrored and for the 1-7 resonances, the b-a-c-d-g-f-e assignment was considered. Overall the $\delta^{obs}_{Ln}(i)$ have been subtracted with the related $\delta^{obs}_{Y}(i)$, leading to the LIS_{Ln} reported in Table 2.9.

2.2.7 Determination of the Fermi contact (δ^{FC}_{Ln}) and Pseudocontact (δ^{PC}_{Ln}) contribution to the LIS_{Ln}, following the "*all lanthanide*" method

The "*all lanthanides*" method allowed to calculate the Fermi contact and pseudocontact contributions to the LIS_{Ln} and to confirm the assignment of the resonances assumed in the previous paragraph.

The $YbGa_4$-2 was selected as reference compound and the δ^{FC}_{Ln} contribution was considered negligible. Hence, the *plot-I* was calculated (Figure 2.13).

The *plot-I* displays the $LIS_{Ln}(i)$ of each **i** proton versus the respective $LIS_{Yb}(i)$. Overall the $LnGa_4$-2 were investigated. However, the linear trend is more evident for heavier lanthanides. The best fit for these straight lines, resulting from the linear regression (forced through the origin) is shown in *plot-I*, as well. The slopes of these lines are indicated as m_{Ln} and are reported in Table 2.10.

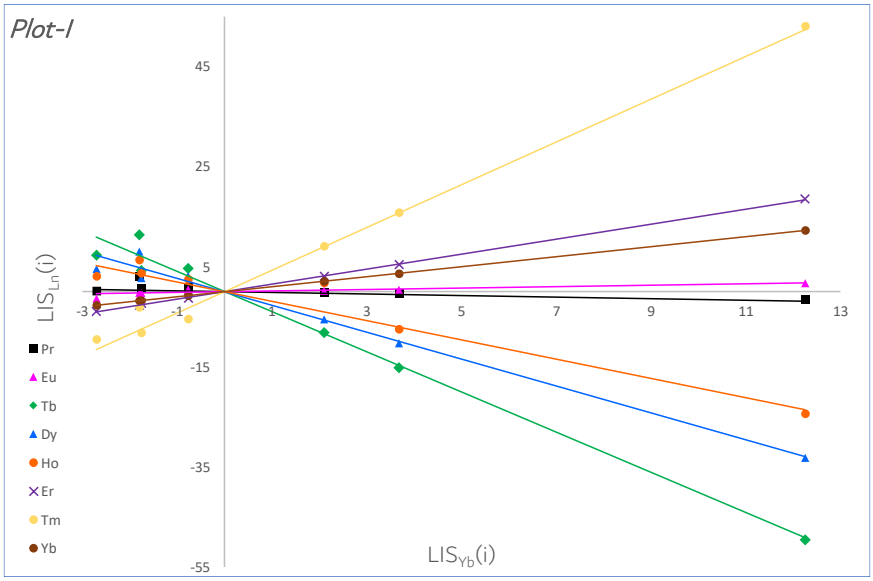

Figure 2.13 "*All lanthanides*" calculations, *Plot-I*. The graph displays the $LIS_{Ln}(i)$ values versus the related $LIS_{Yb}(i)$ of the $LnGa_4$-2 series of compounds. All the calculated $LIS_{Ln}(i)$ were considered. The best fit was traced as straight lines, as a result of the linear regression forced through the origin.

Table 2.10 m_{Ln} slopes values for the $LnGa_4$-2 complexes, related to the *plot-I*

plot-I	Pr	Eu	Tb	Dy	Ho	Er	Tm	Yb
mLn	-0.15(9)	0.14(3)	-4.0(2)	-2.7(1)	-1.9(2)	1.50(1)	4.3(2)	1
R2	0.31	0.93	0.99	0.98	0.93	0.75	1	0.99

As long as discussed in the previous case (i.e. for $LnMn_4$), the $\mathbf{m}_{Ln}$ values are proportional to the anisotropy of the magnetic susceptibility tensor, and are expected to be positive for prolate lanthanide ions and negative for oblate ones, consistent with the slopes of *Plot-I*. As established by the "*all lanthanide*" method, if (I) the complexes are strictly isostructural, (II) the overall Ln^{III} ions experience the same crystal field splitting effect (B_{Ln}, see eqn. 1.6), and (III) the $\delta^{FC}_{Ln}(i)$ term is negligible compared to the $\delta^{PC}_{Ln}(i)$ one, then the $\mathbf{m}_{Ln}$ parameter would ideally reduce to the

C_J(Ln)/C_J(Yb) ratio of the Bleaney's constants, within the limits of validity of Bleaney's theory mentioned in Paragraph 1.3.2 and detailed elsewhere [20,62] This explains why the slopes are larger for heavier lanthanides than for lighter ones, as the lanthanides within Tb^{III}-Yb^{III} have larger Bleaney's constants (Table S1, Chapter 2, Supplementary Materials).[63]

The standard deviations of $\mathbf{m}_{Ln}$ and the R^2 values, reported in Table 2.10, demonstrate that deviations from the linearity in *plots-I* are experienced by Pr and Eu derivatives. This behavior is accounted for a non-negligible Fermi contact $\delta^{FC}_{Ln}(i)$ contribution and preclude the determination of the $\delta^{PC}_{Ln}(i)$ and $\delta^{FC}_{Ln}(i)$ contributions for these compounds. The different behavior of the heavier lanthanides (i.e. Tb-Yb) in $LnGa_4$-2 is another example of the previously mentioned phenomenon named "*Gadolinium break*".

The *plot-II* was determined for the Tb-$YbGa_4$-2 complexes: the $LIS_{Ln}(i)/\langle S_z\rangle_{Ln}$ values were plotted as a function of $\mathbf{m}_{Ln}/\langle S_z\rangle_{Ln}$. and straight lines were obtained from the linear regression of the data (Figure 2.14 *"All lanthanides"* calculations, *Plot-II.* The graph displays the $\delta^{para}_{Ln}(i)/\langle S_z\rangle_{Ln}$ ratio for each lanthanide versus the $\mathbf{m}_{Ln}/\langle S_z\rangle_{Ln}$ ratio. The Tb-$YbGa_4$-2 derivatives were considered.).

Thanks to the linear regression, the slopes (M(i)) and the intercepts (Q(i)) of the overall straight lines were calculated (Table 2.11). It is worth noting here that for each proton, the M(i) value can be calculated.

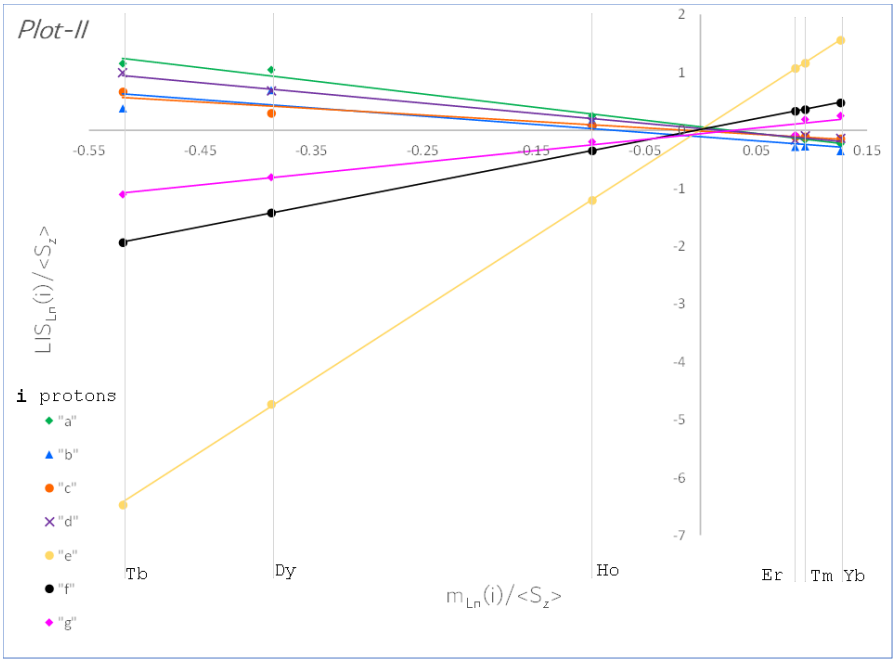

Figure 2.14 *"All lanthanides"* calculations, *Plot-II*. The graph displays the $\delta^{para}_{Ln}(i)/\langle S_z\rangle_{Ln}$ ratio for each lanthanide versus the $m_{Ln}/\langle S_z\rangle_{Ln}$ ratio. The Tb-$YbGa_4$-2 derivatives were considered.

Table 2.11 Slopes, Intercepts and R^2 values related to the *Plot-II*, (Figure 2.14)

resonances	*a*	*b*	*c*	*d*	*e*	*f*	*g*
M(i)	-2.3(1)	-1.4(3)	-1.1(1)	-1.76(9)	12.39(5)	3.73(1)	1.2.0(2)
Q(i)	-0.06(3)	-0.11(9)	-0.02(3)	0.03(2)	0.01(1)	-0.010(3)	-0.06(5)
R^2	0.99	0.83	0.95	0.99	1	1	0.97

These M(i) values will be used to determine the $\delta^{PC}_{Ln}(i)$ and $\delta^{FC}_{Ln}(i)$ contributions and provide a confirmation of the two assumptions done at the beginning: (I) the assignments of the resonances based on those of the $EuGa_4$-2, (II) the LIS_{Ln} calculation based on this assumption, and (III) the $\delta^{FC}_{Ln}(i)$ contribution negligible compared to the pseudocontact shift. It is also interesting to highlight that the Q(i) values are not statistically significative.

Table 2.12 $\delta^{PC}_{Ln}(i)$ and $\delta^{FC}_{Ln}(i)$ contributions, calculated for the Tb-$YbGa_4$-2 complexes by means of the eqns. 1.12, 1.13 and 3.4.

	δ^{PC}_{Ln} | δ^{FC}_{Ln}													
H	*a*		*b*		*c*		*d*		*E*		*f*		*g*	
Tb	9.10	-1.79	5.71	11.42	4.51	0.13	7.05	-2.77	-49.67	0.15	-14.95	-0.20	-7.93	-0.20
Dy	6.09	-1.57	3.83	8.03	3.02	0.10	4.72	-1.96	-33.26	0.12	-10.01	-0.27	-5.31	-0.24
Ho	4.37	-1.27	2.74	6.42	2.17	0.35	3.38	0.36	-23.82	-0.53	-7.17	-0.31	-3.80	5.57
Er	-3.41	-0.49	-2.14	-2.74	-1.69	0.40	-2.64	0.36	18.59	-0.09	5.60	-0.18	2.97	0.11
Tm	-9.69	0.18	-6.08	-3.12	-4.80	-0.65	-7.50	-0.65	52.86	0.23	15.92	-0.03	8.44	0.68
Yb	-2.27	-0.44	-1.43	-1.80	-1.13	0.36	-1.76	0.00	12.39	-0.14	3.73	-0.05	1.98	0.12

Hence, the Fermi contact contributions have been calculated as the difference between the LIS_{Ln} and the pseudocontact contribution (eqn. 3.4), instead of what claimed for the "*all lanthanides*" method (eqn. 1.14, paragraph 1.3.3). The $\delta^{PC}_{Ln}(i)$ and $\delta^{FC}_{Ln}(i)$ contributions were calculated by means of equations 1.12, 1.13 and 3.4.

2.2.8 Correlation of the crystal structures with the information in solution: assignments of ^{1}H NMR resonances

The values of the $<G(i)_{XRD}>$ terms were calculated from the X-Ray structure of the Dy, Ho and Er -Ga_4-2 derivatives. Distances and angles are reported in Table S7 (Chapter 2, Supplementary Materials). Thanks to the high similarity of these terms, the <G(i)> values related to the three Ln were merged resulting in an average <<G(i)>> series (values and related standard deviations are reported in Table 2.13 M(i)/M(c) ratios extrapolated from the *a-g* resonances, G(i) terms and G(i)/G(j) ratios calculated from the ϑ_i and r_i values (Table S7, Chapter 2, Supplementary Materials) related to the X-Ray structures of the $LnGa_4$-2 series.). The latter geometrical parameters were correlated to the M(i) ones, related to the structure in

solution. The determination of the M(i)/M(c) and the <<G(i)>>/ <<G(c)>> ratios (where c is the smaller M(i) or G(i) parameter) for the overall shi^{3-} protons allowed to confirm the assignments determined at the beginning for the $EuGa_4$-2 and assumed for all the others $LnGa_4$-2 complexes. (Table 2.13) The same cannot be said for the benzoate protons, whose M(i)/M(c) ratios do not correspond to the <<G(i)>>/<<G(c)>> ones. This can be ascribed to slight fluxionality or a partial dissociation of the benzoate linkers. Within this hypothesis the signals of the NMR spectra would be the average of a hang on/off process which may affect these carboxylate linkers. Despite the consideration concerning the benzoate linkers, overall the other observations are consistent with the $LnGa_4$-2 structure retainment after dissolution, at least for the heavy-lanthanides derivatives.

Table 2.13 M(i)/M(c) ratios extrapolated from the *a-g* resonances, G(i) terms and G(i)/G(j) ratios calculated from the ϑ_i and r_i values (Table S7, Chapter 2, Supplementary Materials) related to the X-Ray structures of the $LnGa_4$-2 series.

	H^{NMR}	M(i)/M(c)	<<G(i)>>	<<G(i)>>/<<G(c)>>	H^{XRD}
Shi^{3-}	*a*	2.02	-2.078344(1)E-3	2.28	A
	b	1.26	-1.11911(1) E-3	1.23	B
	c	1	-9.1103394(3)E-4	1	C
	d	1.56	-1.337032(5) E-3	1.46	D
OBz	e	-11.00	4.16(2) E-4	-0.95	E
	f	-3.31	1.21854(2)E-3	-1.40	F
	g	-1.76	-2.48(7) E-3	6.61	G

Even if in the solid state the shi^{3-} ligand was found disordered in two positions, possibly the fluxionality, which takes place in solution, averages this effect and only one set of narrowed resonances was found, when collecting the $_1H$ NMR spectra.

Therefore, by comparing the $\langle G(i)_{XRD}\rangle/\langle G(c)_{XRD}\rangle$ parameters, obtained from the crystal structure, with the M(i)/M(c) parameters, obtained from the NMR data and related with the structure in solution (through the $G(i)_{NMR}$ parameter, defined in eqn. 1.8 and applied in eqn. 1.10, paragraph 1.3.3), we could unambiguously assign the NMR resonances to the four shi^{3-} protons. This assignment has been carried out based solely on the evaluation of the Lanthanide Induced Shifts, and therefore the assignments for the shi^{3-} reported in Table 2.13 represent a proof of consistency of our approach and of the hypothesis, on which it is based.

Conclusions

In this section I presented the ^{1}H NMR analysis of the chemical shifts observed for twelve $Ln^{III}Na^{I}(OAc)_4$[12-$MC_{Mn^{III}(O)H3Shi-3H}$-4] complexes (Ln^{III}-MC), and thirteen $Ln^{III}Na^{I}(OBz)_4$[12-$MC_{Ga^{III}(O)H3Shi-3H}$-4] complexes (Ln = Pr-Lu, except Pm, and Y). Beside the YMn_4, YGa_4-2, $LaGa_4$-2 and $LuGa_4$-2, all the other complexes contain a paramagnetic center. The Y-derivatives have been investigated as diamagnetic references. The $LuGa_4$-2 ^{1}H NMR spectrum 100% matches the Y-metallacrown. Considering that Y^{III} resembled Gd^{III} in terms of ionic radius, this result supports the hypothesis that the complexes in solution are stable and isostructural irrespective of the dimension of the core metal.

Despite the paramagnetic nature of the metal centers, narrow and well resolved resonances were found for both the 12-MC-4 series. In the case of $LnMn_4$, two independent paramagnetic systems affect the diamagnetic chemical shift. The main contribution to the chemical shift is determined by the $[Mn]_4$ paramagnetic system, while the Ln^{III} induces a second order perturbation. On the contrary, in the $LnGa_4$-2 compounds the overall paramagnetic shift is determined by the lanthanides, which act as major actors, shifting the signals from the diamagnetic positions.

The lanthanide induced shift (LIS_{Ln}) values were calculated for all the compounds and then treated following the "*all lanthanides*" method. In both the series, the *plot-I* shows that the Fermi contact contribution to the chemical shift is not negligible for the lighter lanthanides, which were not further analyzed.

As far as it concerns the gadolinium derivatives, the presence of the $[Mn]_4$ paramagnetic system enhanced the relaxation time, allowing to observe the ^1H NMR signals, being the first example in literature, to the best of our knowledge. On the contrary, when alone, the Ln paramagnetic system does not act, increasing the protons relaxation time, indeed, the $GdGa_4$-2 spectrum does not show resolved signals.

Finally, the "*all lanthanides*" calculations provided both the δ^{FC}_{Ln} and δ^{PC}_{Ln} values for the Gd-$YbMn_4$ series and for the Tb-$YbGa_4$-2 one.

One of the main advantages in the application of the "*all lanthanide*" procedure was the possibility to calculate both the δ^{FC}_{Ln} and δ^{PC}_{Ln} parameters without any *a-priori* assumption, which is not common in literature.[19] Indeed, this approach was based solely on the evaluation of the Lanthanides Induced shift and overall the assumptions necessary to carried out the calculations are confirmed by ad-hoc checkpoints, placed within the procedure (e.g. the *plot-I* is the checkpoint for the negligible Fermi contact contribution assumption). Therefore, any results here listed constitutes a pure experimental confirmation of the stability of the MC-scaffold in solution and of the retention of the molecular structure after dissolution.

Moreover, the presence of one set of resonances on each LnM_4 spectra, gives rise to the hypothesis that minor rearrangements in the structure take place, when the complexes dissolve. Indeed, the crystal structures of the complexes do not exhibit a proper C_4 axis, whose evidence in the ^1H NMR spectra suggests, that in solution these systems average the small distortions and turn into 4-fold symmetrical molecules.

No information is provided either on the presence of a coordinated sodium ion on the concave face of the metallacrown, or conversely on its possible dissociation. The investigations of the Na behavior after the dissolution of these compounds represents one of the next steps in the characterization of these systems.

Finally, by taking advantage of the X-Ray crystallographic data combined with the parameters obtained from the "*all lanthanides*" calculations, we were able to unambiguously assign the resonances of the Shi^{3-} protons both in case of the $LnMn_4$ and the $LnGa_4$-2 compounds.

We plan to provide additional confirmations about the assignments of the resonances, by preparing and analyzing the same complexes using monodeuterated salicylhydroxamic acid as ligand and para-methylated benzoic acid. Indeed, the resultant complexes will show two less signals, allowing to confirm the results discussed in the present dissertation.

However, these results are unprecedented in the field of the characterization of metallacrowns and may open the future use of paramagnetic NMR methods for structural determination of these species in solution.

Moreover we intend now to investigate the magnetic properties of these molecules and, if worth, to make use of the resulting features to develop materials or probes which are responsive to stimuli that produce small conformational changes on their structure and, in turn, to the (para)magnetic properties of the materials.

Experimental

Materials and Methods - All reagents and solvents were purchased from Sigma Aldrich or Alfa Aesar and used without further purification. The metallacrown complexes of formula $Ln^{III}Na^{I}(OAc)_4[12\text{-}MC_{Mn^{III}(O)H3Shi\text{-}3H}\text{-}4](H_2O)_4 6DMF$ were provided by the group of our collaborator prof C. Zaleski at the University of Shippnsburg (USA), following the synthetic procedure reported elsewhere.[33] The $Ga(NO_3)_3{\cdot}xH_2O$ salt was purchased form commercial sources as well, used without further purification and considered octa-hydrated, based on studies reported elsewere.[64] Lanthanides nitrate salts has been used as source of Ln^{III} and are reported as $Ln(NO_3)_3{\cdot}xH_2O$, where x stays for hexa-hydrated for bigger lanthanides (i.e. La-Gd and Y) and penta-hydrate for smaller lanthanides (Dy-Lu).

^1H NMR spectra were recorded on Bruker Advance 400 and Varian Vnmrs500 spectrometers using standard pulse sequences. Chemical shifts are reported in part per million (ppm) and were referenced to the residual signals of the solvents. Spectra were collected in the -60 to +100 ppm range. Both deuterated methanol (CD_3OD) and deuterated dimethylsulfoxide (DMSO-d_6) were used as the solvent for the characterization of the LnM_4 isostructural series of compounds. The overall NMR spectra processing and analysis (including deconvolution and bandwidth analysis) were performed by using the MestReNova 8.0 and MestReNova v12.0.1-20560 software packages.[59] Least square regression analysis (relaxation times and calculations through the "all lanthanides" method) were performed using the software SPSS.[65]

Single crystal X-Ray diffraction data of $LnMn_4$ series and of the $Dy^{III}(OBz)_4[12\text{-}MC_{Ga^{III}(O)H3Shi\text{-}3H}\text{-}4](py)(Hpy)(MeOH)_2$ where previously reported and taken from the Cambridge Crystallographic Data Centre (the deposition CCDC number for $LnMn_4$ are respectively

987612-22 and for the $DyGa_4$-1 derivative is 1479310).[33,40] Single crystal X-Ray diffraction data of the $Na^{I}Ln^{III}(OBz)_4[12\text{-}MC_{Ga^{III}(O)H3Shi\text{-}3H}\text{-}4](H_2O)_x(DMF)_y$ series, where Ln^{III} stays for Dy, Ho, Er, Yb, Lu and Y, were collected at 150 K on a Bruker D8 Photon II X-Ray diffractometer (Mo Ka; l = 0.71073 Å) equipped with a low temperature device. Rigaku d*trek images were exported to CrysAlisPro for processing.[66] Absorption correction was applied using the program SADABS.[67] The structures were solved by direct methods ShelXT,[68] and refined with full-matrix least squares,[69] using the Olex2 software package. The analysis of the structures (including distances and angles measurements) were carried out with the Mercury 3.10 software package.[70]

Synthesis of $Na^{I}Ln^{III}(OBz)_4[12\text{-}MC_{Ga^{III}(O)H3Shi\text{-}3H}\text{-}4](H_2O)_3(DMF)_y$ ($LnGa_4$-2, where Ln^{III}= Dy, Ho, Er, Yb) – The synthetic procedure for preparing the $LnGa_4$-2 complexes was optimized by modifying a previously reported route for the synthesis of the $Dy^{III}(OBz)_4[12\text{-}MC_{Ga^{III}(O)H3Shi\text{-}3H}\text{-}4]$.[40] Salicylhydroxamic acid (30.5 mg, 0.2 mmol) and sodium benzoate (82 mg, 0.6 mmol) were dissolved in 5 mL of a 1:1:0.25 DMF/MeOH/pyridine solution. $Ga(NO_3)_3{\cdot}xH_2O$ (79.9 mg, 0.2 mmol) was dissolved in methanol and added to the solution under stirring. After 5 minutes stirring $Ln(NO_3)_3{\cdot}xH_2O$ (0.05 mmol) dissolved in methanol was added and the resulting solution was stirred for about 5 minutes. NaCl dissolved in the minimum quantity of water and 1 mL of methanol were finally added to the solution, which was concentrated at RT and crystalized at -4°C. Slow evaporation of the solvents gave crystals suitable for X-Ray diffraction analysis, after two days. $LnNaGa_4(shi)_4(OBz)_4(H_2O)_3(DMF)_y$ (YGa_4-2). ESI-MS, $[LnGa_4(C_7H_4O_3N)_4(C_7H_5O_2)_4]^-$ calc. for $[YMC]^-$ 1452.79; found; 1451.74; calc. for $[PrMC]^-$ 1504.8 found, 1504.78; calc. for $[NdMC]^-$ 1505.8, found 1506.91; calc. for $[SmMC]^-$ 1515.81, found 1514.43; calc. for $[EuMC]^-$

1516.81, found 1515.95; calc. for $[GdMC]^-$ 1521.41, found 1521.52; calc. for $[TbMC]^-$ 1522.81, found 1522.92; calc. for $[DyMC]^-$ 1527.82, 1526.98; calc. for $[HoMC]^-$ 1528.82, found 1528.56; calc. for $[TmMC]^-$ 1532.82, found 1531.8; calc. for $[YbMC]^-$ 1537.83, found 1537.6.

Bibliography

1. Parker D. Excitement in f block : structure, dynamics and function of nine-coordinate chiral lanthanide complexes in aqueous media. Chem Soc Rev. 2004;33(3):156-165. doi:10.1039/b311001j

2. Bünzli J-CG. Lanthanide Luminescence for Biomedical Analyses and Imaging. Chem Rev. 2010;110(5):2729-2755. doi:10.1021/cr900362e

3. Gai S, Li C, Yang P, Lin J. Recent Progress in Rare Earth Micro/Nanocrystals: Soft Chemical Synthesis, Luminescent Properties, and Biomedical Applications. Chem Rev. 2014;114(4):2343-2389. doi:10.1021/cr4001594

4. Heffern MC, Matosziuk LM, Meade TJ. Lanthanide Probes for Bioresponsive Imaging. Chem Rev. 2014;114(8):4496-4539. doi:10.1021/cr400477t

5. Aspinall HC. Chiral Lanthanide Complexes: Coordination Chemistry and Applications. Chem Rev. 2002;102(6):1807-1850. doi:10.1021/cr010288q

6. Shibasaki M, Yoshikawa N. Lanthanide Complexes in Multifunctional Asymmetric Catalysis. Chem Rev. 2002;102(6):2187-2210. doi:10.1021/cr010297z

7. Copéret C, Comas-Vives A, Conley MP, et al. Surface Organometallic and Coordination Chemistry toward Single-Site Heterogeneous Catalysts: Strategies, Methods, Structures, and Activities. Chem Rev. 2016;116(2):323-421. doi:10.1021/acs.chemrev.5b00373

8. Viswanathan S, Kovacs Z, Green KN, Ratnakar SJ, Sherry AD. Alternatives to gadolinium-based metal chelates for magnetic resonance imaging. Chem Rev. 2010;110(5):2960-3018. doi:10.1021/cr900284a

9. Chan WTK, Wong W-T. Recent development in lanthanide coordination compounds for biomedical imaging applications. Polyhedron. 2014;83:150-158. doi:http://dx.doi.org/10.1016/j.poly.2014.05.054

10. Amoroso AJ, Pope SJA. Using lanthanide ions in molecular bioimaging. Chem Soc Rev. 2015;44(14):4723-4742. doi:10.1039/C4CS00293H

11. Binnemans K. Lanthanide-Based Luminescent Hybrid Materials. Chem Rev. 2009;109(9):4283-4374. doi:10.1021/cr8003983

12. Wang X, Chang H, Xie J, et al. Recent developments in lanthanide-based luminescent probes. Coord Chem Rev. 2014;273–274:201-212. doi:http://dx.doi.org/10.1016/j.ccr.2014.02.001

13. Pointillart F, Le Guennic B, Cador O, Maury O, Ouahab L. Lanthanide Ion and Tetrathiafulvalene-Based Ligand as a “magic” Couple toward Luminescence, Single Molecule Magnets, and Magnetostructural Correlations. Acc Chem Res. 2015;48(11):2834-2842. doi:10.1021/acs.accounts.5b00296

14. Guillou O, Daiguebonne C, Calvez G, Bernot K. A Long Journey in Lanthanide Chemistry: From Fundamental Crystallogenesis Studies to Commercial Anticounterfeiting Taggants. Acc Chem Res. 2016;49(5):844-856. doi:10.1021/acs.accounts.6b00058

15. Sessoli R, Powell AK. Strategies towards single molecule magnets based on lanthanide ions. Coord Chem Rev. 2009;253(19–20):2328-2341. doi:http://dx.doi.org/10.1016/j.ccr.2008.12.014

16. Rinehart J, Long J. Exploiting single-ion anisotropy in the design of f-element single-molecule magnets. Chem Sci. 2011;2(11):2078-2085. doi:10.1039/c1sc00513h

17. Guo Y-N, Xu G-F, Guo Y, Tang J. Relaxation dynamics of dysprosium(III) single molecule magnets. Dalt Trans. 2011;40(39):9953-9963. doi:10.1039/c1dt10474h

18. Woodruff DN, Winpenny REP, Layfield RA. Lanthanide Single-Molecule Magnets. Chem Rev. 2013;113(7):5110-5148. doi:10.1021/cr400018q

19. Di Pietro S, Piano S Lo, Di Bari L. Pseudocontact shifts in lanthanide complexes with variable crystal field parameters. Coord Chem Rev. 2011;255(23-24):2810-2820. doi:10.1016/j.ccr.2011.05.010

20. Blackburn OA, Edkins RM, Faulkner S, et al. Electromagnetic susceptibility anisotropy and its importance for paramagnetic NMR and optical spectroscopy in lanthanide coordination chemistry. Dalt Trans. 2016;45(16):6782-6800. doi:10.1039/C6DT00227G

21. Bertini I, Luchinat C. Chapter 3 Relaxation. Coord Chem Rev. 1996;150:77-110. doi:10.1016/0010-8545(96)01243-X

22. Di Bari L, Pintacuda G, Salvadori P, Dickins RS, Parker D. Effect of axial ligation on the magnetic and electronic properties of lanthanide complexes of octadentate ligands. J Am Chem Soc. 2000;122(38):9257-9264. doi:10.1021/ja0012568

23. Valencia L, Martinez J, Macías A, Bastida R, Carvalho RA, Geraldes CFGC. X-ray diffraction and 1H NMR in solution: Structural determination of lanthanide complexes of a Py2N6Ac4 ligand. Inorg Chem. 2002;41(20):5300-5312. doi:10.1021/ic0257017

24. Di Bari L, Lelli M, Pintacuda G, Pescitelli G, Marchetti F, Salvadori P. Solution versus Solid-State Structure of Ytterbium Heterobimetallic Catalysts. J Am Chem Soc. 2003;125(18):5549-5558. doi:10.1021/ja0297640

25. Fernández-Fernández MDC, Bastida R, Macías A, Pérez-Lourido P, Platas-Iglesias C, Valencia L. Lanthanide(III) complexes with a tetrapyridine pendant-armed macrocyclic ligand: 1H NMR structural determination in solution, X-ray diffraction, and density-functional theory calculations. Inorg Chem. 2006;45(11):4484-4496. doi:10.1021/ic0603508

26. Di Bari L, Di Pietro S, Pescitelli G, Tur F, Mansilla J, Saá JM. [Ln(binolam)3]·(OTf)3, a New Class of Propeller-Shaped Lanthanide(III) Salt Complexes as Enantioselective Catalysts: Structure, Dynamics and Mechanistic Insight. Chem - A Eur J. 2010;16(47):14190-14201. doi:10.1002/chem.201001683

27. Lah MS, Pecoraro VL. Isolation and Characterization of (Mnii[Mniii(Salicylhydroximate)]4(Acetate)2(Dmf)6).2DMF - an Inorganic Analog of M2+ (12-Crown-4). J Am Chem Soc. 1989;111(18):7258-7259. doi:10.1021/ja00200a054

28. Lah MS, Pecoraro VL. A functional analogy between crown ethers and metallacrowns. Inorg Chem. 1991;30(5):878-880. doi:10.1021/ic00005a002

29. Lah MS, Gibney BR, Tierney DL, Pennerhahn JE, Pecoraro VL. The Fused Metallacrown Anion Na2([Na0.5[Ga(Salicylhydroximate)]4]2(μ 2-OH)4)- Is an Inorganic Analog of a Cryptate. J Am Chem Soc. 1993;115(13):5857-5858. doi:10.1021/ja00066a077

30. Gibney BR, Wang H, Kampf JW, Pecoraro VL, Bldg R. Structural Evaluation and Solution Integrity of Alkali Metal Salt Complexes of the Manganese 12-Metallacrown-4 (12-MC-4) Structural Type. 1996;89(1):6184-6193. doi:10.1021/ic960371+

31. Kessissoglou DP, Bodwin JJ, Kampf J, Dendrinou-Samara C, Pecoraro VL. Pseudohalide complexation by manganese 12-metallacrowns-4 complexes. Inorganica Chim Acta. 2002;331(1):73-80. doi:10.1016/S0020-1693(01)00755-1

32. Koumousi ES, Mukherjee S, Beavers CM, Teat SJ, Christou G, Stamatatos TC. Towards models of the oxygen-evolving complex (OEC) of photosystem II: a Mn4Ca cluster of relevance to low oxidation states of the OEC. Chem Commun. 2011;47(39):11128-11130. doi:10.1039/C1CC13770K

33. Azar MR, Boron TT, Lutter JC, et al. Controllable Formation of Heterotrimetallic Coordination Compounds: Systematically Incorporating Lanthanide and Alkali Metal Ions into the Manganese 12-Metallacrown-4 Framework. Inorg Chem. 2014;53(3):1729-1742. doi:10.1021/ic402865p

34. Cao F, Wang S, Li D, et al. Family of mixed 3d-4f dimeric 14-metallacrown-5 compounds: Syntheses, structures, and magnetic properties. Inorg Chem. 2013;52(19):10747-10755. doi:10.1021/ic3025952

35. Boron TT, Lutter JC, Daly CI, et al. The Nature of the Bridging Anion Controls the Single-Molecule Magnetic Properties of DyX 4 M 12-Metallacrown-4 Complexes. Inorg Chem. 2016;55(20):10597-10607. doi:10.1021/acs.inorgchem.6b01832

36. Beccia MR, García B, García-Tojal J, Leal JM, Secco F, Tegoni M. The mechanism of the Cu 2+ [12-MC Cu(Alaha) -4] metallacrown formation and lanthanum(III) encapsulation. doi:10.1039/c4dt00557k

37. Happ P, Plenk C, Rentschler E. 12-MC-4 metallacrowns as versatile tools for SMM research. Coord Chem Rev. 2015;289-290(1):238-260. doi:10.1016/j.ccr.2014.11.012

38. Tegoni M, Furlotti M, Tropiano M, Choong), Lim S, Pecoraro VL. Thermodynamics of Core Metal Replacement and Self-Assembly of Ca 2þ 15-Metallacrown-5. Inorg Chem. 2010;49:5190-5201. doi:10.1021/ic100315u

39. Zaleski CM, Tricard S, Depperman EC, et al. Single Molecule Magnet Behavior of a Pentanuclear Mn-Based Metallacrown Complex: Solid State and Solution Magnetic Studies. Inorg Chem. 2011;50(22):11348-11352. doi:10.1021/ic2008792

40. Chow CYCY, Eliseeva SVS V, Trivedi ERER, et al. Ga3+/Ln3+Metallacrowns: A Promising Family of Highly Luminescent Lanthanide Complexes That Covers Visible and Near-Infrared Domains. J Am Chem Soc. 2016;138(15):5100-5109. doi:10.1021/jacs.6b00984

41. Boron TT, Lutter JC, Daly CI, et al. The Nature of the Bridging Anion Controls the Single-Molecule Magnetic Properties of DyX 4 M 12-Metallacrown-4 Complexes. 2016;55(20). doi:10.1021/acs.inorgchem.6b01832

42. Travis JR, Zeller M, Zaleski CM, et al. Crystal structure of tetraaqua(dimethylformamide)tetrakis(μ - N ,2-dioxidobenzene-1-carboximidato)tetrakis(μ - trimethylacetato)tetramanganese(III)sodiumyttrium–dimethylformamide–water (1/8.04/0.62). Acta Crystallogr Sect E Crystallogr Commun. 2015;71(11):1300-1306. doi:10.1107/S2056989015018216

43. Travis JR, Zeller M, Zaleski CM. Facile carboxylate ligand variation of heterotrimetallic 12-metallacrown-4 complexes. Polyhedron. 2016;114:29-36. doi:10.1016/j.poly.2015.09.006

44. Chow CY, Trivedi ER, Pecoraro V, Zaleski CM. Heterometallic Mixed 3d-4f Metallacrowns: Structural Versatility, Luminescence, and Molecular Magnetism. Comments Inorg Chem. 2015;35(4):214-253. doi:10.1080/02603594.2014.981811

45. Lim CS, Tegoni M, Jakusch T, Kampf JW, Pecoraro VL. Clarifying the mechanism of cation exchange in Ca(II)[15-MCCu(II)Ligand-5] complexes. Inorg Chem. 2012;51(21):11533-11540. doi:10.1021/ic3013798

46. Tegoni M, Furlotti M, Tropiano M, Choong), Lim S, Pecoraro VL. Thermodynamics of Core Metal Replacement and Self-Assembly of Ca 2þ 15-Metallacrown-5. Inorg Chem. 2010;49:5190-5201. doi:10.1021/ic100315u

47. Lah MS, Pecoraro VL. Isolation and Characterization of (Mnii[Mniii(Salicylhydroximate)]4(Acetate)2(Dmf)6).2Dmf - an Inorganic Analog of M2+ (12-Crown-4). J Am Chem Soc. 1989;111(18):7258-7259. doi:10.1021/ja00200a054

48. Eaton DR. The Nuclear Magnetic Resonance of Some Paramagnetic Transition Metal Acetylacetonates. J Am Chem Soc. 1965;87(14):3097-3102. doi:10.1021/ja01092a015

49. La Mar GN, Walker FA. Proton nuclear magnetic resonance line widths and spin relaxation in paramagnetic metalloporphyrins of chromium(III), manganese(III), and iron(III). J Am Chem Soc. 1973;95(21):6950-6956. doi:10.1021/ja00802a014

50. Koenig SH, Brown RD, Spiller M. The anomalous relaxivity of Mn3+(TPPS4). Magn Reson Med. 1987;4(3):252-260. doi:10.1002/mrm.1910040306

51. Luz Z, Silver BL, Fiat D. O–17 Nuclear Magnetic Resonance of Manganese (III) Tris(Acetylacetonate). J Chem Phys. 1967;46(2):469-471. doi:10.1063/1.1840690

52. Vishnevskaya GP, Kozyrev BM. Effect of solvent on the paramagnetic relaxation constants in liquid solutions of gadolinium nitrate. J Struct Chem. 1967;7(1):20-24. doi:10.1007/BF00739229

53. Hudson A, Lewis JWE. Electron spin relaxation of 8S ions in solution. Trans Faraday Soc. 1970;66(0):1297-1301. doi:10.1039/tf9706601297

54. Koenig SH. From the relaxivity of Gd(DTPA)2– to everything else. Magn Reson Med. 1991;22(2):183-190. doi:10.1002/mrm.1910220204

55. Hernandez G, Bryant RG, Tweedle MF. Proton magnetic relaxation dispersion in aqueous glycerol solutions of Gd(DTPA)2- and Gd(DOTA)-. Inorg Chem. 1990;29(25):5109-5113. doi:10.1021/ic00350a018

56. Aime S, Barbero L, Botta M. Trends in NMR studies of paramagnetic Gd(III) complexes as potential contrast agents in MRI. Magn Reson Imaging. 1991;9(5):843-847. doi:10.1016/0730-725X(91)90386-Z

57. Bertini I, Capozzi F, Luchinat C, Nicastro G, Xia Z. Water proton relaxation for some lanthanide aqua ions in solution. J Phys Chem. 1993;97(24):6351-6354. doi:10.1021/j100126a007

58. Atzeri C, Marzaroli V, Quaretti M, et al. Elucidation of 1 H NMR Paramagnetic Features of Heterotrimetallic Lanthanide(III)/Manganese(III) 12-MC-4 Complexes. Inorg Chem. 2017;56(14):8257-8269. doi:10.1021/acs.inorgchem.7b00970

59. MestReNova. 2013;8.1.4(4.9.9.9).

60. Rigault S, Piguet C. Predictions and assignments of NMR spectra for strongly paramagnetic supramolecular lanthanide complexes: The effect of the “gadolinium break” [5]. J Am Chem Soc. 2000;122(38):9304-9305. doi:10.1021/ja000958u

61. Piguet C, Geraldes CFGC. Paramagnetic NMR Lanthanide Induced Shifts for Extracting Solution Structures. In: Geschneidner JKA, Bunzli J-CG, Pecharsky VK, eds. Handbook on the Physics and Chemistry of Rare Earths. Vol 33. Amsterdam: Elsevier Science; 2003:353-463. doi:10.1016/S0168-1273(02)33005-8

62. S. Dickins R, Parker D, I. Bruce J, J. Tozer D. Correlation of optical and NMR spectral information with coordination variation for axially symmetric macrocyclic Eu(III) and Yb(III) complexes: axial donor polarisability determines ligand field and cation donor preference. Dalt Trans. 2003;127(7):1264-1271. doi:10.1039/b211939k

63. Bleaney B. Nuclear magnetic resonance shifts in solution due to lanthanide ions. J Magn Reson. 1972;8(1):91-100. doi:10.1016/0022-2364(72)90027-3

64. A. Marini V berbenni. Thermal Decomposition Of Gallium Nitrte Hydrate Ga(NO3)3xH2O. J Therm Anal Calorim. 2005;82:401-407.

65. SPSS. SPSS. 2011;(17.0.0).

66. Agilent. CrysAlis PRO. 2014.

67. Sheldrick GM. Area-Detector Absorption Correction. 1996.

68. Sheldrick GM. SHELXT – Integrated space-group and crystal-structure determination. Acta Crystallogr Sect A Found Adv. 2015;71(1):3-8. doi:10.1107/S2053273314026370

69. Sheldrick GM. Crystal structure refinement with SHELXL. Acta Crystallogr Sect C Struct Chem. 2015;71(1):3-8. doi:10.1107/S2053229614024218

70. Macrae CF, Bruno IJ, Chisholm JA, et al. Mercury CSD 2.0 – new features for the visualization and investigation of crystal structures. J Appl Crystallogr. 2008;41(2):466-470. doi:10.1107/S0021889807067908

Chapter 2

SUPPLEMENTARY MATERIAL

Table S1

The first row reports the density maps of the *4f*-shell electron density distributions of free lanthanides ions at the lower *J* states. The prolate, oblate or spherical shapes are based on the quadrupole approximation.

The second and third rows report respectively the Bleaney's constants C_J and the $<S_z>_{Ln}$, parameters. The latter is a magnetic constant and correspond to the expectation value of the *z*-component of the total spin angular momentum for the Ln^{III}. Overall data were previously reported in literature.[a]

	Pr^{3+} $4f^2$	Nd^{3+} $4f^3$	Sm^{3+} $4f^5$	Eu^{3+} $4f^6$	Gd^{3+} $4f^7$	Tb^{3+} $4f^8$
4f e⁻ density distribution	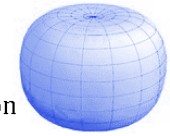	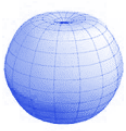	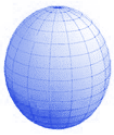	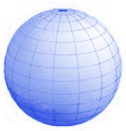	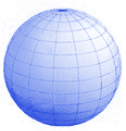	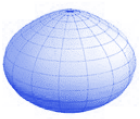
C_J	-20.7	-8.08	0.943	7.53	0	-157.5
$<Sz>_{Lnj}$	2.97	4.49	-0.06	-10.68	-31.5	-31.82

	Dy^{3+} $4f^9$	Ho^{3+} $4f^{10}$	Er^{3+} $4f^{11}$	Tm^{3+} $4f^{12}$	Yb^{3+} $4f^{13}$	Lu^{3+} $4f^{14}$
4f e⁻ density distribution	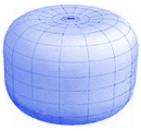	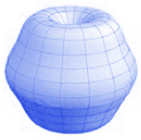	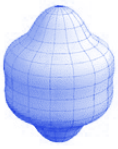	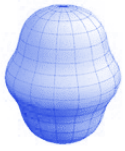	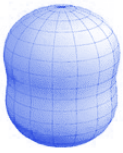	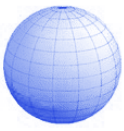
C_J	-181	-71.2	58.8	95.3	39.2	-
$<Sz>_{Lnj}$	-28.54	-22.63	-15.37	-8.21	-2.59	-

[a]Ref.s:

- Parker, D. Excitement in f block: structure, dynamics and function of nine-coordinate chiral lanthanide complexes in aqueous media. Chem. Soc. Rev. 2004, 33, 156–165.
- Bünzli, J.-C. G. Lanthanide luminescence for biomedical analyses and imaging. Chem. Rev. 2010, 110, 2729–2755.
- S. Jiang and S. Qinc Prediction of the quantized axis of rare-earth ions: the electrostatic model with displaced point charges. Inorg. Chem. Front.,2015, 2,613–619

Table S2

Distances and bowing terms, which support the description of the structure in the solid state of the $LnMn_4$ compounds. The following list of distances are reported:

- Ln-O_{ox}MP: and Na-O_{ox}MP : distance between the Ln/Na and the cavity oxygen mean plane
- Ln-O_{ac}MP: distance between the Ln and the acetate oxygen mean plane
- Ln-MnMP: distance between the Ln and manganese ring metals mean plane
- Na-Ln: the distance between the sodium and the lanthanide along the pseudo-C_4 axis
- C_{ox}-Mn^{III} - O_{ac}MP: the angle between the C carbon of the hydroxamic ligand, the manganese and the acetate oxygen
- Δ (O-Mn MP): the distance between the oxygen and manganes mean planes.

Ln-Mn₄	distances (Å)					bowing terms	
	Ln^{III} - O_{ox}MP	Ln^{III} - O_{ac}MP	Ln^{III} - MnMP	Na^{I} - O_{ox}MP	Na^{I} - Ln^{III}	C_{ox}-Mn^{III} – O_{ac}MP(°)	Δ (O-Mn MP) (Å)
Pr	1.7	0.97	2.07	1.88	3.58	103.95	0.37
Nd	1.68	0.99	2.05	1.89	3.58	103.52	0.37
Sm	1.65	1	2.01	1.89	3.54	103.08	0.36
Eu	1.63	1.02	1.99	1.9	3.53	102.85	0.36
Gd	1.62	1.03	1.97	1.91	3.53	102.66	0.35
Tb	1.61	1.02	1.96	1.9	3.51	102.52	0.35
Dy	**1.59**	**1.03**	**1.94**	**1.9**	**3.5**	**102.4**	**0.35**
Ho	**1.58**	**1.03**	**1.92**	**1.91**	**3.49**	**102.19**	**0.34**
Er	**1.57**	**1.04**	**1.91**	**1.91**	**3.48**	**102.03**	**0.34**
Tm	1.56	1.03	1.91	1.91	3.46	101.84	0.35
Yb	1.55	1.03	1.9	1.91	3.46	101.69	0.35
Y	**1.57**	**1.04**	**1.92**	**1.92**	**3.49**	**102.31**	**0.35**

Table S3 – Crystallographic tables related to X-Ray analysis of the $LnGa_4$-2 series

	Y	Dy	Ho	Er	Lu
Empirical formula	$C_{66}H_{44}Ga_4N_7NaO_{26}Y$	$C_{72.25}H_{85.05}DyGa_4N_{8.8}NaO_{29.3}$	$C_{63}H_{60.34}Ga_4HoN_{6.34}NaO_{26.34}$	$C_{66}H_{44}ErGa_4N_7NaO_{26}$	$C_{65}H_{65}Ga_4LuN_7NaO_{26}$
Formula weight ($gmol^{-1}$)	1741.86	2009.91	1794.36	1820.21	1837.08
Temperature/K	150	150	150	150	150
Crystal system	tetragonal	monoclinic	tetragonal	tetragonal	tetragonal
Space group	P4nc	Pn	P4nc	P4nc	P4nc
a/Å	16.7845(5)	14.3389(7)	16.7853(5)	16.7558(5)	16.7381(5)
b/Å	16.7845(5)	16.9909(7)	16.7853(5)	16.7558(5)	16.7381(5)
c/Å	16.3354(6)	16.8450(8)	16.2510(6)	16.2307(6)	16.4414(6)
α/°	90	90	90	90	90
β/°	90	95.376(2)	90	90	90
γ/°	90	90	90	90	90
Volume/$Å^3$	4602.0(3)	4085.9(3)	4578.7(3)	4556.9(3)	4606.3(3)
Z	2	2	2	2	2
$\rho_{calc}g/cm^3$	1.257	1.634	1.302	1.327	1.325
μ/mm^{-1}	1.851	2.297	2.086	2.15	2.288
F(000)	1742	2031	1791	1800	1836
Crystal size/mm^3	0.22 × 0.22 × 0.07	0.19 × 0.1 × 0.07	0.4 × 0.2 × 0.2	0.3 x 0.12 x 0.7	0.23 x 0.09 x 0.4
Radiation (nm)	MoKα (λ = 0.71073)	MoKα (λ = 0.71073)	MoKα (λ = 0.71073)	MoKα (λ = 0.71073)	MoKα (λ = 0.71073)
2Θ range for data collection/°	4.854 to 51.414	4.3 to 52.098	5.426 to 51.6	4.862 to 51.414	4.956 to 51.438
No.of rflcn/unique	83730/4388	82433/16110	104392/4412	122025/4343	115771/4401
Data/restraints/parameters	4388/356/269	16110/5/1004	4412/330/265	4343/338/268	4401/333/265
Goodness-of-fit on F^2	1.153	1.048	1.134	1.12	1.165
R_1 [I>=2σ (I)]	0.0782	0.0335	0.0684	0.1611	0.057
wR_2 [I>=2σ (I)]	0.2155	0.0867	0.1974	0.053	0.163
Resid. Dens / $e^- Å^{-3}$	0.83/-0.63	1.50/-0.73	2.15/-0.92	1.94/-1.86	1.81/-3.62
Flack parameter	0.06(3)	0.008(3)	0.033(7)	0.000(5)	0.025(5)

Table S4

Distances and bowing terms, which support the description of the structure in the solid state of the Dy-Ga_4-1 and Ln-Ga_4-2 compounds. The following list of distances are reported:

- Ln-O_{ox}MP: and Na-O_{ox}MP : distance between the Ln/Na and the cavity oxygen mean plane
- Ln-O_{ac}MP: distance between the Ln and the acetate oxygen mean plane
- Ln-GaMP: distance between the Ln and gallium ring metals mean plane
- Na-Ln: the distance between the sodium and the lanthanide along the pseudo-C_4 axis
- C_{ox}-Ga^{III} - O_{ac}MP: the angle between the C carbon of the hydroxamic ligand, the gallium and the acetate oxygen
- Δ (O-Ga MP): the distance between the oxygen and gallium mean planes.

Ln-Ga₄	distances (Å)					bowing terms	
	Ln^{III} - O_{ox}MP	Ln^{III} - O_{bz}MP	Ln^{III} - GaMP	Na^{I} - O_{ox}MP	Na^{I} - Ln^{III}	C_{ox}-Ga^{III} - O_{bz}MP (°)	Δ (O-Ga MP) (Å)
Dy-Ga_4-1	1.39	1.14	1.7	-	-	105.8	0.31
Dy-Ga_4-2	1.5	1.1	1.82	1.9	3.39	102.56	0.32
Ho-Ga_4-2	1.46	1.1	1.79	2.03	3.49	101.59	0.33
Er-Ga_4-2	1.46	1.04	1.78	2.01	3.48	102.08	0.32
Lu-Ga_4-2	1.45	1.12	1.75	2	3.45	101.75	0.3
Y-Ga_4-2	1.46	1.04	1.79	2.14	3.44	102.38	0.33

Table S5

T_1 spin-lattice relaxation constants and signal bandwidths (v ½ , Hz) for the proton signals in the spectra of the YMn_4 and $GdMn_4$ in deuterated methanol, at RT. The Y was reported as a diamagnetic reference. The overall relaxation time are reported elsewhere. [a]

		Signals				
Ln		Me	1	2	3	4
YMn4	δ (ppm)	27.8	10.4	-16.9	-20.5	-24.3
	T_1(ms)	2.35(1)	1.30(2)	1.48(1)	6.54(1)	7.36(1)
	v ½ (Hz)	360	290	250	60	70
GdMn4	δ (ppm)	27.8	10.1	-16.5	-20.5	-24.2
	T_1(ms)	0.14(1)	0.66(2)	0.93(4)	3.06(5)	3.35(5)
	v ½ (Hz)	2090	790	450	170	170

[a]Ref: Elucidation of ^{1}H NMR Paramagnetic Features of Heterotrimetallic Ln(III)/Mn(III) 12-MC-4 Complexes. C. Atzeri, V. Marzaroli, M. Quaretti, J. R. Travis, L. Di Bari, C. M. Zaleski*‡, and M. Tegoni *Inorg. Chem.*, 2017, *56* (14), pp 8257–8269

Figure S1

Deconvolution of the overlapped 1 and Me signals (23 and 20 ppm, respectively) in the spectrum of $DyMn_4$. Black: observed spectrum; blue: deconvolution functions; purple: calculated spectrum; red: residual function (observed – calculated). The relative integral of the two functions corresponds to 1:3 ratio.

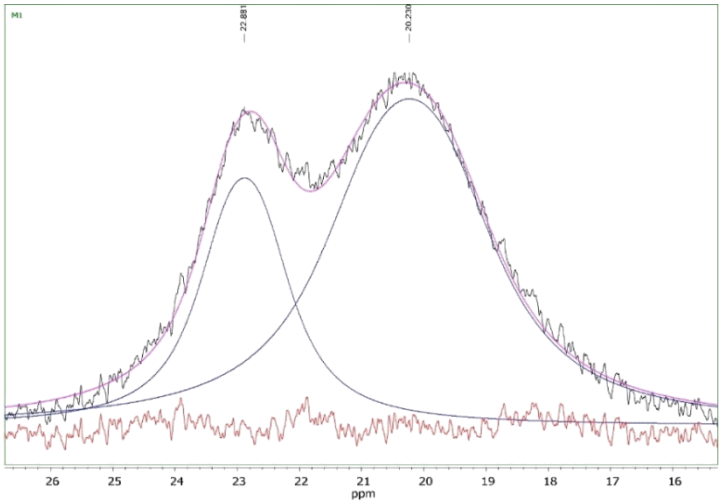

Deconvolution of the overlapped 2 and 3 signals (-27.4 and -28.0 ppm, respectively) in the spectrum of $TmMn_4$. Black: observed spectrum; blue: deconvolution functions; purple: calculated spectrum; red: residual function (observed – calculated). The relative integral of the two functions corresponds to 1:1.ratio.

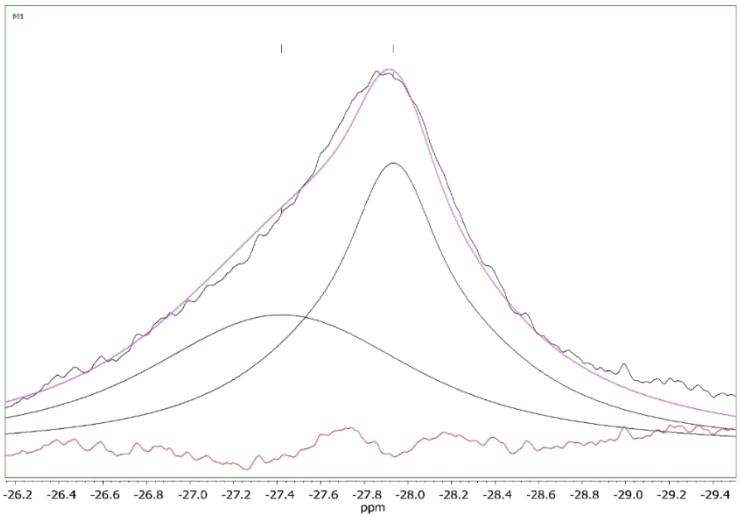

Table S6

Average distances ($r_{Ln..H}$) and angles with respect of the molecular axis ($\vartheta_{Na\text{-}Ln\text{-}H}$) for the shi^{3-} protons in the Gd-$YbMn_4$ series (see labelling in Figure 2.7 and here below). Data obtained from the X-Ray crystal structure and measured with the appropriate tools of the Mercury Software. The angles between the nucleus under consideration and the principal magnetic axis of the lanthanide ion has been approximated into the Na^{I}-Ln^{III} direction. Distances and angles have been averaged for each proton in the four shi^{3-} ligands.

		r Ln-H (Å)				ϑ Na-Ln-H (°)			
		HA	HB	HC	HD	HA	HB	HC	HD
$LnMn_4$	Gd	7.94	9.31	8.93	6.98	114.55	113.05	111.77	112.78
	Tb	7.81	9.29	8.916	6.96	114.47	111.99	111.72	112.68
	Dy	7.92	9.29	8.914	6.96	114.32	112.85	111.59	112.53
	Ho	7.91	9.28	8.903	6.95	114.2	112.75	111.52	112.41
	Er	7.90	9.27	8.894	6.94	114.21	112.77	111.49	112.38
	Tm	7.89	9.26	8.882	6.94	114.13	112.71	111.48	112.34
	Yb	7.89	9.27	8.888	6.94	114.11	112.72	111.44	112.28

Figure S2

2D COSY of the YGa_4-2 collected in DMSO-d_6 at RT

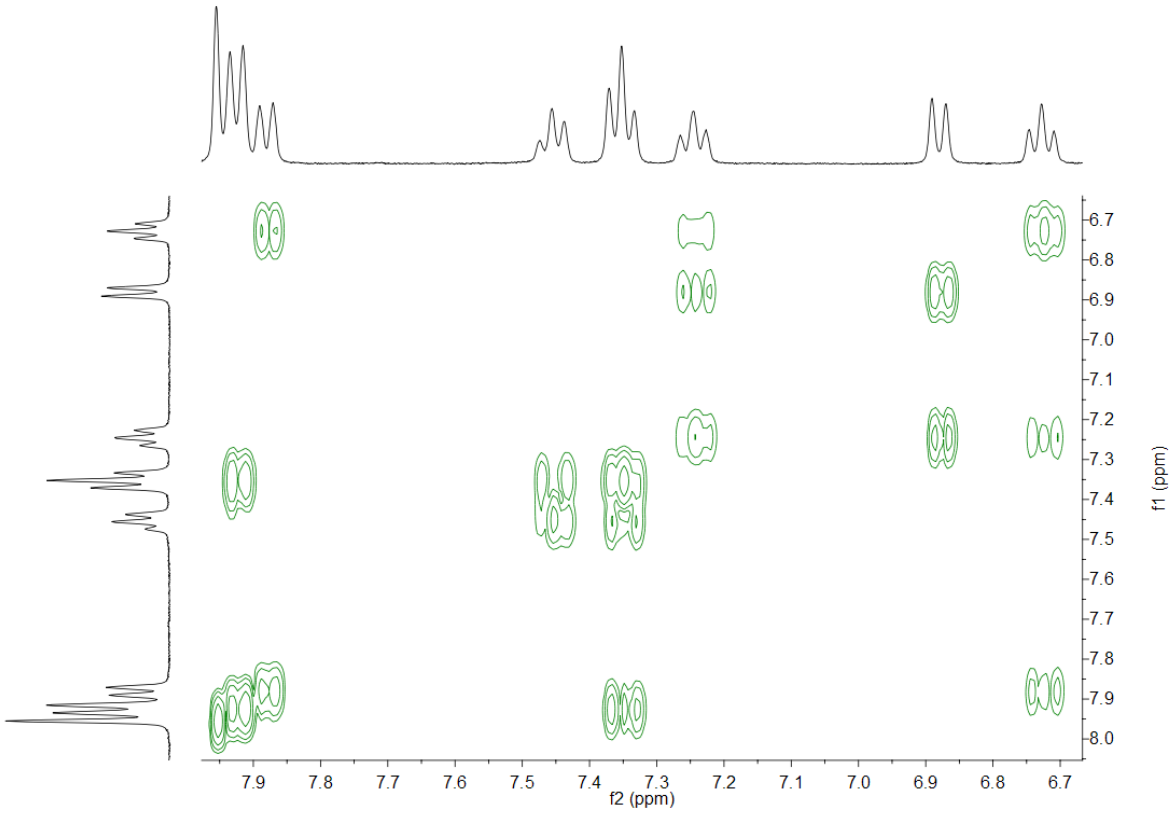

Figure S3

^{1}H NMR of the $LnGa_4$-2 collected in DMSO-d_6 at RT. The Nd and Sm are included. As far as it concerns the $SmGa_4$-2 no analysis is displayed, since the spectrum shows impurities.

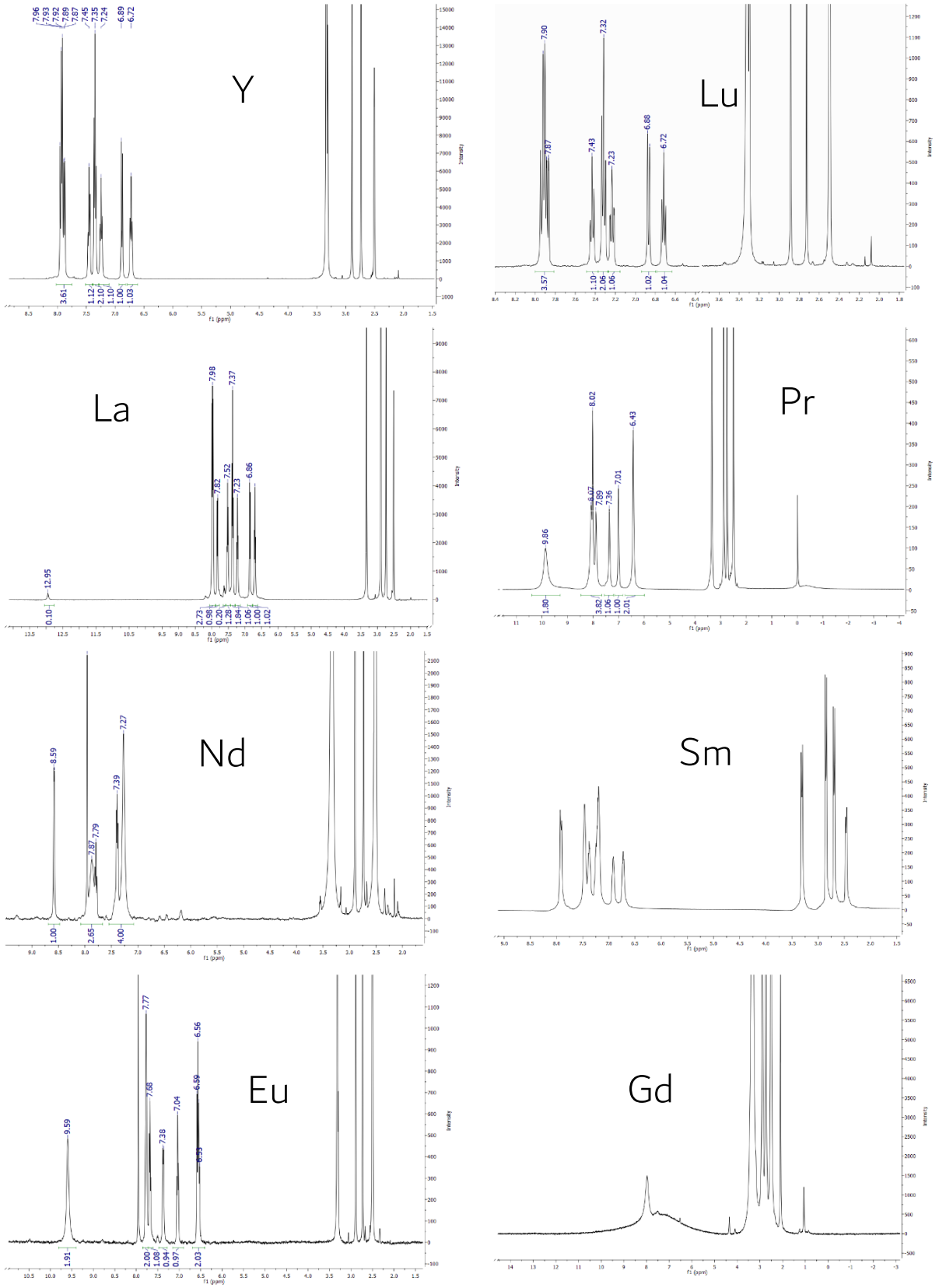

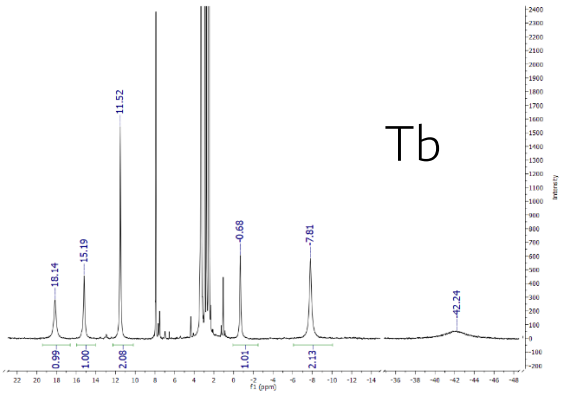
Tb
18.14
15.19
11.52
0.68
7.61
42.24
0.99
1.00
2.08
1.01
2.13

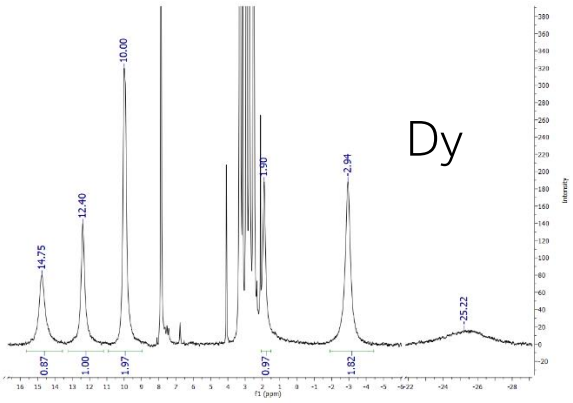
Dy
14.75
12.40
10.00
1.90
2.94
25.22
0.87
1.00
1.97
0.97
1.82

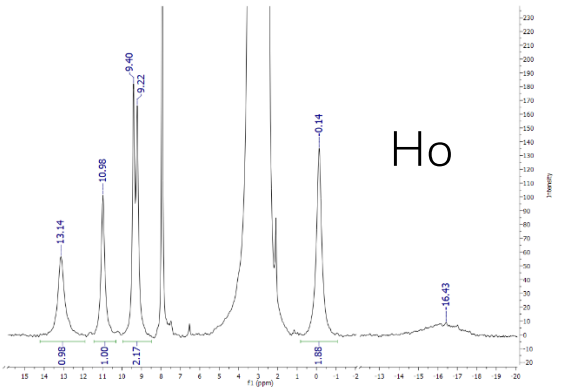
Ho
13.14
10.98
9.40
9.22
0.14
16.43
0.98
1.00
2.17
1.88

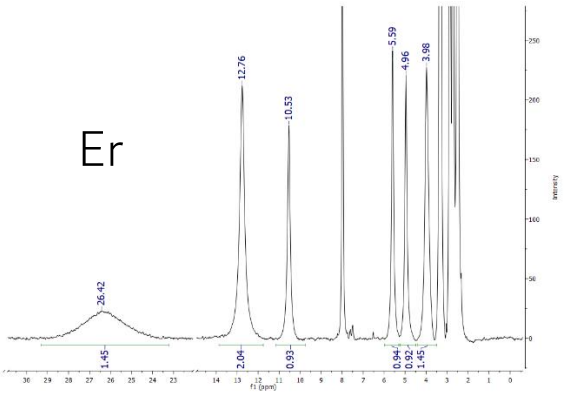
Er
26.42
12.76
10.53
5.59
4.96
3.98
1.45
2.04
0.93
0.94
0.92
1.45

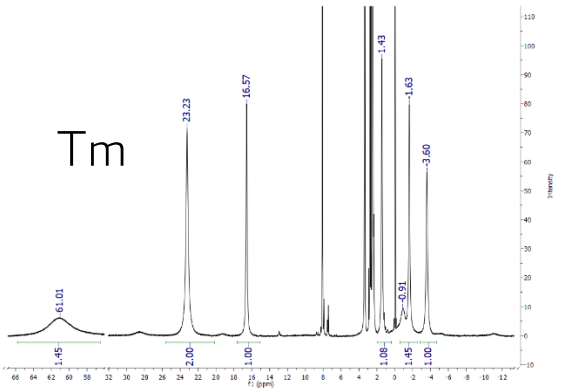
Tm
61.01
23.23
16.57
1.43
1.63
3.60
0.91
1.45
2.00
1.00
1.08
1.45
1.00

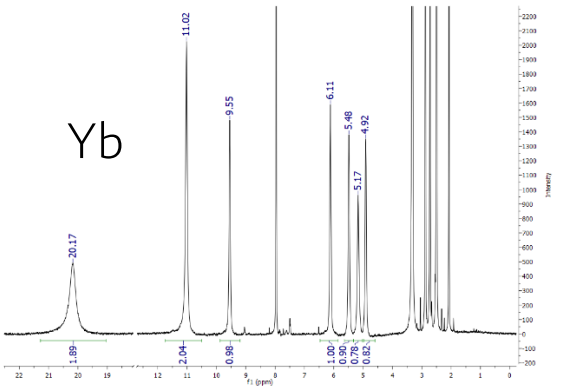
Yb
20.17
11.02
9.55
6.11
5.48
4.92
5.17
1.89
2.04
0.98
1.00
0.90
0.78
0.82

Table S7

Average distances ($r_{Ln..H}$) and angles with respect of the molecular axis ($\vartheta_{Na\text{-}Ln\text{-}H}$) for the shi^{3-} and benzoate protons in the Tb-$YbGa_4$-2 series (see labelling in Figure 2.11 and here below). Data obtained from the X-Ray crystal structure.od the Dy, Ho and Er derivatives. The angles between the nucleus under consideration and the principal magnetic axis of the lanthanide ion has been approximated into the Na^{I}-Ln^{III} direction. In the case of Dy, distances and angles have been averaged for each proton in the four shi^{3-} ligands and four benzoate linkers. In the case of both Ho and Er distances and angles have been averaged for each shi^{3-} proton disordered in the two positions (see Figure 2.4-Right).

	Dy			Ho			Er		
	Average r_i (Å)	average ϑ_i (°)	<G(i)>	average r_i (Å)	average ϑ_i (°)	<G(i)>	average r_i (Å)	average ϑ_i (°)	<G(i)>
HA	6.85	70.40	-2.1 E-03	6.81	70.45	-2.1 E-03	6.83	70.31	-2.1 E-03
HB	8.77	72.63	-1.1 E-03	8.77	75.73	-1.2 E-03	8.78	72.09	-1.1 E-03
HC	9.16	71.63	-9.1 E-04	9.17	71.69	-9.1 E-04	9.17	71.59	-9.1 E-04
HD	7.82	68.78	-1.3 E-03	7.80	69.96	-1.4 E-03	7.80	69.78	-1.4 E-03
HE - HE'	5.08	126.92	6.3 E-04	5.06	123.67	-6.0 E-04	5.08	128.44	1.2 E-03
HF - HF'	7.13	133.67	1.2 E-03	7.11	133.20	1.1 E-03	7.08	134.56	1.3 E-03
HG	7.97	134.96	9.8 E-04	7.92	136.28	1.1 E-03	3.95	68.31	-9.6 E-03

Chapter 3

THREE DIMENSIONAL METALLACROWN BASED COORDINATION POLYMERS

"It has been stated that Shakespeare "only" strung words together to make beautiful sentences. I hope I demonstrated how, in the field of reticular chemistry, we have "only" strung molecules together to make crystals that are not just of wondrous beauty but of unparalleled diversity and utility."

Omar M. Yaghi

Introduction

Ordered assemblies of metal complexes and especially porous coordination polymers (PCPs), are largely investigated in these years. One of the reasons lies in the fact, that PCPs are promising materials that may have applications in gas storage, separations of small molecules, catalysis, luminescence and magnetism.[1–7]

Functional metallacrowns, on the other hand, provide an opportunity to reach highly responsive materials, thanks to the high density of metal ions. In addition, functional MCs are rigid scaffolds, whose materials are expected to retain, after polymerization, those properties exhibited on the molecular level.[8,9] Considering the achievable functional metallacrowns, the most promising in terms of their possible applications are those that show luminescent brightness,[10–14] single-molecule magnetic behavior,[15–27] and, as recognition agents, selectivity for both anionic or cationic guests.[28–36] These are all desirable properties to be incorporated into porous coordination polymers.

In addition, the metallacrown literature clearly describes how topologies and chemical-physical properties of this class of compounds, can be predicted to some extent.[37–40] In the past 20 years, an extensive investigation of a huge number of structures and functional properties of metallacrowns has been carried out, leading to the proof of concept, that the final architecture and features of metallacrown assemblies, depends on the choice of the starting building blocks (i.e. metal ions, ligand and linkers, already described in paragraphs 1.1.3-7), both in solution and in the solid state.[38,41–44]

The latter considerations suggest that it is possible to design ligands and linkers capable to give rise to extended networks of metallacrowns, possibly three dimensional, and interestingly when porous. In other words, the use of metallacrowns as Secondary Building Units (SBUs,

paragraph 1.2) may be a successful approach for the construction of coordination polymers, containing luminescent or magnetic metallacrowns.

Moreover, because a wide variety of building blocks may result in functional metallacrowns, and because the modification of the periphery of both ligands and linkers does not usually prevent their formation, it becomes particularly interesting to design MCs based SBUs capable to assemble in three-dimensional porous coordination polymers (Figure 3.1). [38,39,45]

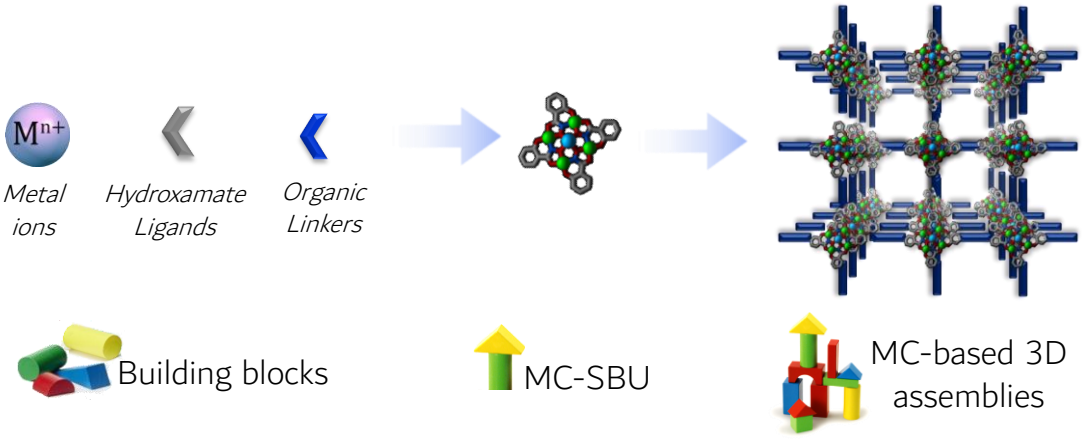

Figure 3.1 Schematic representation of the genesis of a MC-based extended three-dimensional network. The typical building blocks of MC (i.e. metal ions, ligands and linkers) are reported on the left, those compounds assemble into MC-based SBUs, that can be possibly connected, leading to MC-based porous coordination polymers. This process resembles the construction of buildings, starting from woody-blocks.

In general, the use of a polymetallic SBU instead of a single metal ion joint, enhances the stability, the rigidity and the robustness of the resulting framework and moreover it also ensures a more straightforward prediction of the topology of the final architecture.[9,46,47]

It is finally worth to point out, that exploiting metallacrowns for the construction of coordination frameworks, means that the joints are SBUs characterized by the M-N-O connectivity, rather than the M-(O/N)-C classical connectivity, commonly found in coordination polymers and MOFs topology.

3.1 Strategies for the construction of MC networks

According to what reported in literature, it is possible to reach MC networks by following two different approaches. The linkage of SBUs, that shows the MC topology, can be reached:

A- by interacting with the scaffold through the edge of the central cavity (Figure 3.2, left)

B- by wisely decorating the ligand periphery with heteroatoms, that act as hooks and are capable to interact externally to the MC scaffold (Figure 3.2, right).

Both these linking strategies may involve intermediate supramolecular interactions given by neutral organic linkers, cationic species, anionic species, solvents, etc. … . In addition these approaches may or not involve an additional external metal ion. [39,48]

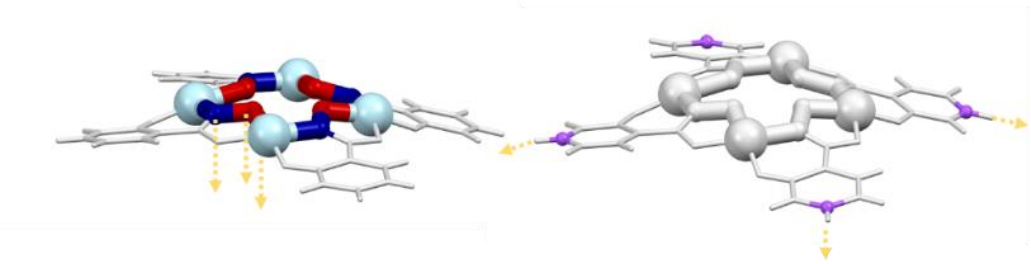

Figure 3.2 Schematic representation of generic 12-MC-4 scaffolds, which highlights the two main approaches to connect MC-SBUs; yellow narrows represent the linking directions. **Left**: representation of the A-strategy: connection through the edge of the central cavity. **Right**: representation of the B-strategy, linking through the ligand periphery. [39,48]

3.2 Examples of MC networks

A large number of coordination networks showing the metallacrown topology was found over the years and some examples are here reported.

Zaleski, showed in 2015 1D-chains, where 12-MC-4 units polymerize, thanks to the presence of aliphatic carboxylates (i.e. propionate and butyrate anions, Figure 3.3, a).[49] These organic

linkers coordinate with both the top of the scaffold of one 12-MC-4 unit and the bottom of the following one, being an example of the A-strategy.

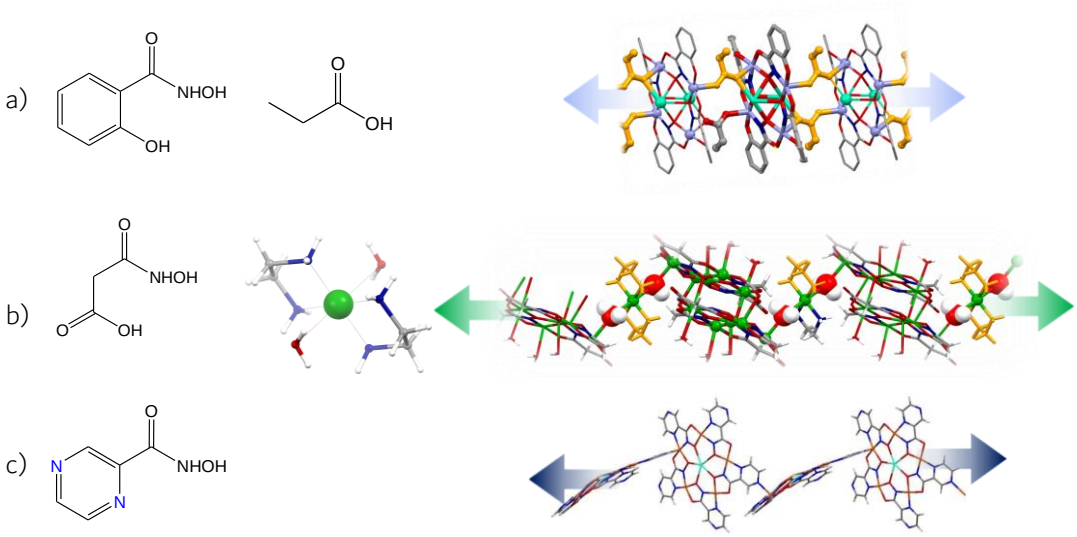

Figure 3.3 Three examples of ligands, linkers and the resulting monodimensional polymeric chains: the Salicylhydroxamic ligand, the propionate linker and the $\{Na_2(O_2CCH_2CH_3)_2[12\text{-}MC_{Mn(III),(O)H3Shi\text{-}3H\text{-}4}](DMF)_4(H_2O)_2\}_n$ chain (**a**); [49] the malonomonohydroxamic acid (H_3mmh) ligand, the $[Cu(en)_2(H_2O)_2]$ intermediating complex and the $\{[Cu(en)_2(H_2O)_2][(\mu\text{-}H_2O)\{Cu(II)[12\text{-}MC_{Cu(II),(O)H3mmh\text{-}3H}\text{-}4)(H_2O)_3\}_2]\}^{2n-}$ chain (**b**); [50] the $\{Gd(III)[15\text{-}MC_{Cu(II)pyzHA\text{-}2H}\text{-}5]^{+3}\}_n$, where thanks to the peripheral N atom, the pyrazinohydroxamic acid is capable to connect MCs units, acting both as ligand and linker at the same time (**c**).[51]

The internal edge of the MC scaffold is involved either in the polymerization of the $\{[Cu(en)_2(H_2O)][(\mu\text{-}H_2O)\{Cu(II)[12\text{-}MC_{Cu(II),(O)H3mmh\text{-}3H}\text{-}4)(H_2O)_3\}_2]\}_n^{2n-}$ anionic polymer, whose chain is reported in Figure 3.3-b (H_3mmh is the malonomonohydroxamic acid ligand). Here, a copper(II)$(en)_2(H_2O)_2$ complex bridges two consecutive MC-dimers. The 1D chain results from the supramolecular interactions, provided by the two water molecules, that bridge the Cu-complex and the edge of the cavity of the dimer.[50] This is another example of A-strategy, which involve an additional external metal ion.

Directed interactions between the ligand periphery of a 15-MC-5 scaffold with the top-face of the following one, lead the $Gd(III)[15\text{-}MC_{Cu(II)\ pyzHA\text{-}2H}\text{-}5]^{+3}$ species to polymerize in 1D chians

(Figure 3.3, *c*).[51] The pyrazinohydroxamate ligand contains one N donor atom, in para to the hydroxamate group, capable to coordinate with one Cu(II) ring metal of the following 15-MC-5 scaffold. The latter is an example of the B-strategy.

Multidimensional coordination networks of metallacrowns are not as frequent as 1D are. The $\{Cu(II)[12\text{-}MC_{Cu(II),dmAphaH\text{-}2H}\text{-}4]^{2+}(4,4'\text{-bipy})_3\}_n$ polymer presents bidimensional layers, stacked in pillars. The SBU is a 12-MC-4 unit formed by copper(II) and the 2-(dimethylamino)phenylhydroxamate ligand ($dmAphaH_2$-2H). Two 4,4'-bipyridine molecules (bipy) coordinate with the top-face of one 12-MC-4 scaffold, and with the bottom of the following one (respectively through the 4, 4' N donor atoms). The result is a 1D chian along the *a* crystallographic axis. A third bipy molecule crosslinks the 1D chains, leading to 2D layers of metallacrowns. (Figure 3.4) [52]

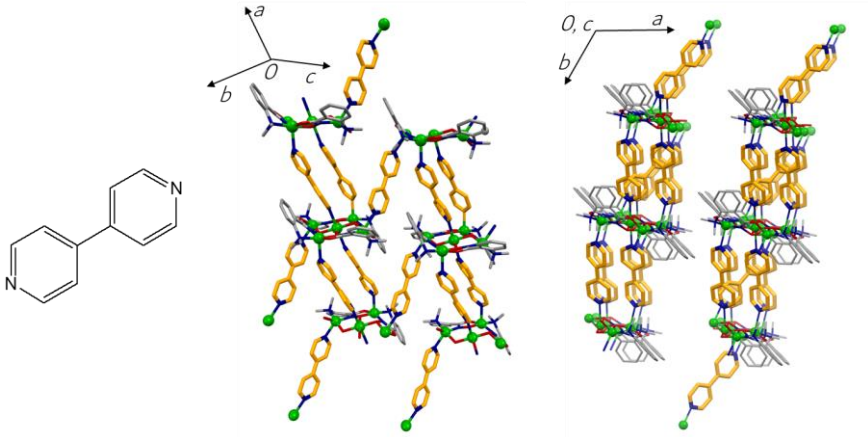

Figure 3.4 Structure of $\{Cu(II)[12\text{-}MC_{Cu(II),dmAphaH\text{-}2H}\text{-}4]^{2+}(4,4'\text{-bipy})_3\}_n$, an example of a bidimensional coordination polymer (counterions and solvents were omitted for clarity). **Left**: Scheme of the 4,4'-bipyridine (bipy) linker. **Right**: top and side views of the 2D layers. The side view along the *b* crystallographic axis highlights the absence of interactions between two stacked layers.[52] Colours code: Cu-green, O-red, N-blue, -C(MC)-grey, C(bipy)-yellow.

Finally, the malonomonohydroxamic acid (H_3mmh) and copper(II) building blocks, which have been described above, capable to form the 1D chains (Figure 3.3-b), can also give rise to the 3D

architecture shown in Figure 3.5, where the metallacrown topology is provided by Cu^{II}[12-$MC_{CuII,(O)H3mmh-3H}$-4] complex. [53]

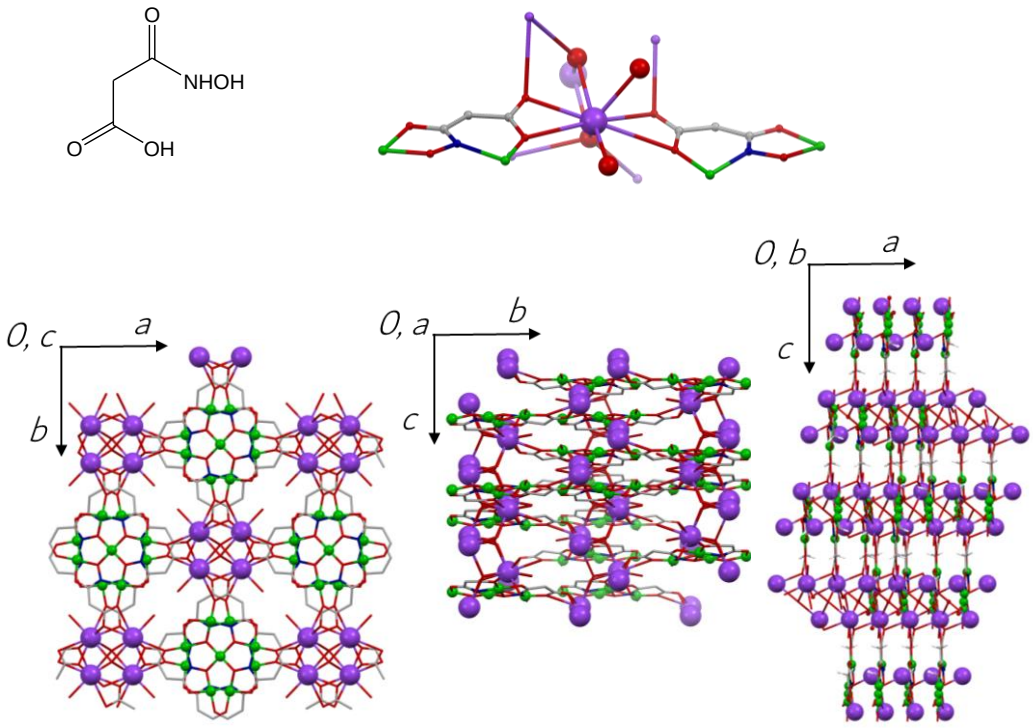

Figure 3.5 Structure of the {[$K(H_2O)_2$]$_2$$Cu^{II}$[12-$MC_{CuII,(O)H3mmh-3H}$-4]}$_n$ three dimensional coordination polymer. **Top**: structure of the malonomonohydroxamic acid ligand (H_3mmh) and of the [$K(H_2O)_2$] linkage complex, where two mmh^{3-} ligands are involved. **Bottom**: the three crystallographic projections of the 3D-coordiation polymer. Colours code: Cu^{II} = green, K^{I} = purple, O = red, N = blue.[53]

Several three dimensional MC-based coordination networks can be found in the recent literature.[47,48,54–61] Nevertheless, among these, only a few were reported to possess real pores and, to the best of knowledge, the only onethat was found permanently porous results from the assembly of the {Cu(II)[12-$MC_{Cu(II),hinHA-3H}$-4]}$^{2-}$ anionic SBU (Figure 3.6). In this case, the presence of one N donor atom in para to the hydroxamate function, is crucial for the 3-hydroxyisonicotine hydroxamate (hin^{3-}) ligand in connecting the MC-based SBUs. The latter is an example of the B-strategy described above. Indeed, two hin^{3-} ligands of two following MCs coordinate an external Cu^{II} ion, whose coordination sphere is completed by one acetate and one

pyridine molecules (Figure 3.6, left). Thus, MC-SBUs alternate with the [Cu^{II}(AcO)Py] complexes and result in a 2D framework. These 2D-layers are stacked in pillars and form endless mono dimensional channels (Figure 3.6, center and left). Moreover, this material can be activated and shows the 23.3 wt% uptake of CO_2 at RT. As a result, the {[Cu^{II}(AcO)Py]$_2${Cu^{II}[12-$MC_{CuII,hinHA-3H}$-4]}}$_n$ can be defined as an example of 2D coordination polymer, permanently porous and whose joints show the MC topology.[37]

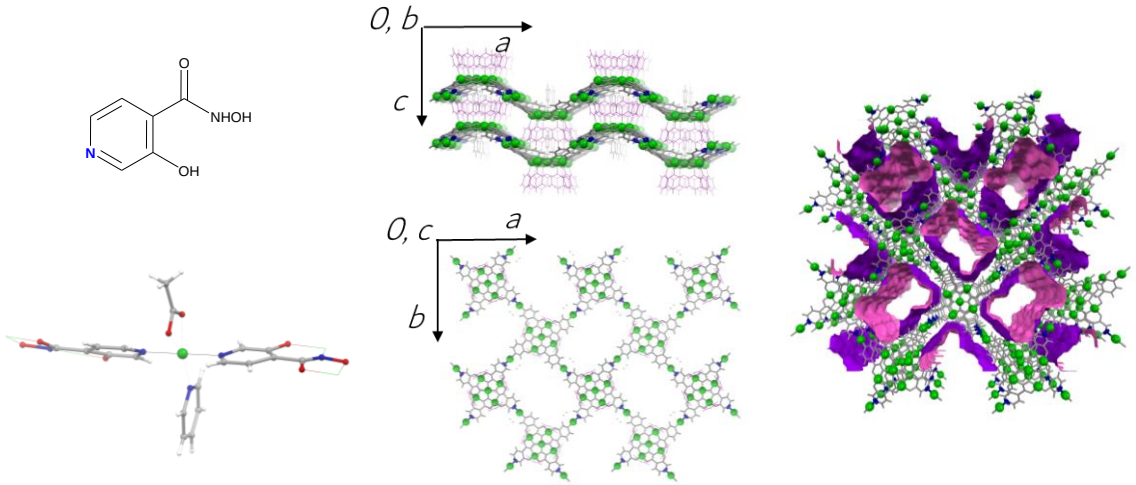

Figure 3.6 The {[Cu^{II}(AcO)Py]$_2${Cu^{II}[12-$MC_{CuII,hinHA-3H}$-4]}}$_n$ 2D coordination polymer. **Left:** scheme of the 3-hydroxyisonicotine hydroxamic acid (H_3HinHA) ligand and of the [Cu^{II}(AcO)Py] linkage. **Center:** top and side views of the 2D layers. **Right**: view of the 1D endless channels. The channels surface is reported in purple.[37]

Overall the examples reported above lead to conclude that the synthesis of 3D, permanently porous coordination networks, having MC-joints is still not straightforward. In addition, most of the examples reported in literature are copper based materials, while recent applications in the field of magnetism often utilize ions with greater single ion paramagnetism and magnetic anisotropy such as mixed valent manganese assemblies.[64]

The use, in charge of SBU, of an endeca-manganese(II/III) metallamacrocycle, whose arms show the MC topology (i.e. M-N-O motif) is here described. This SBU will be further on referred to as **Mn_{11}-cage** and was exploited to originate five different 3D networks. The main features,

which differentiate the five networks are summarized in the scheme reported here below (Figure 3.7 Schematic representation of the main features, which differenciate the new five 3D networks, obtained by the connection of the Mn11-cage SBU, which is an endeca-manganese(II/III) metallamacrocycle, whose arms show the typical MC topology (i.e. M-N-O motif)).

Hydroxamic Acid Ligand	Linker	Complete acronim	Reference number	Linkage entities
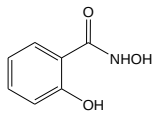 H_3Shi		Na-$Mn_{11}Shi_6$	6	
		K-$Mn_{11}Shi_6$	7	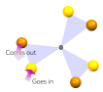
		Cs-$Mn_{11}Shi_6$	8	
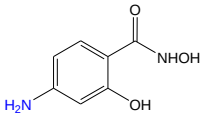 H_3p-aShi		Na-$Mn_{11}p$-$aShi_6$	9	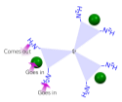
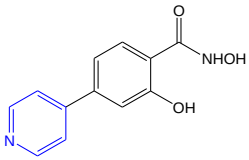 H_3p-pyShi	-	$Mn_{11}p$-$pyShi_6$	10	

Figure 3.7 Schematic representation of the main features, which differenciate the new five 3D networks, obtained by the connection of the Mn_{11}-cage SBU, which is an endeca-manganese(II/III) metallamacrocycle, whose arms show the typical MC topology (i.e. M-N-O motif).

The five networks show the same Mn_{11}-cage joint, and every framework is formed by following the B-strategy of polymerization, described at the beginning of Chapter 3. However, the five MC-based coordination polymers are connected by different linkage entities.

Three to the five networks were prepared using the salicylhydroxamate (shi^{3-}) ligand and the resulting SBUs were connected through external alkali metals, leading to the Na-$Mn_{11}Shi_6$ (**6**), K-$Mn_{11}Shi_6$ (**7**) and Cs-$Mn_{11}Shi_6$ (**8**) networks.

The design of two new ligands, *p*-aShi$_6^{3-}$ and *p*-pyShi$_6^{3-}$, led to the two remaining networks. Those are: the Na-Mn$_{11}$*p*-aShi$_6$ (**9**) and Mn$_{11}$*p*-pyShi$_6$ (**10**) coordination polymers. Indeed, the position in para to the salicylhydroxamate group was functionalized, and the *p*-aShi$_6^{3-}$ and *p*-pyShi$_6^{3-}$ ligands were obtained by placing respectively an-amino (-NH$_2$) and a pyridyl (-py) hook, capable to connect SBUs.

Finally, it is worth to point out that the following list of acronyms will be used further on:

- Mn$_{11}$-cage, refers to the generic SBU
- Mn$_{11}$*p*-RShi$_6$ (where R stays for H, NH$_2$, py), differentiates the ligands
- X-Mn$_{11}$*p*-RShi$_6$ (where X means Na^I, K^I, Cs^I and R stays for H, NH$_2$, py) take into account also of the alkali metal ion bridges.

Results and discussion

Manganese(II) acetate, salicylhydroxamate derivative (*p*-RShi^{3-}) and alkali metals linkers (X) self-assemble in DMF solution at 50°C, forming the Mn_{11}-cage. The slow evaporation of the solvent allows the systems to polymerize, leading to five X-Mn_{11}*p*-$RShi_6$ three dimensional frameworks.

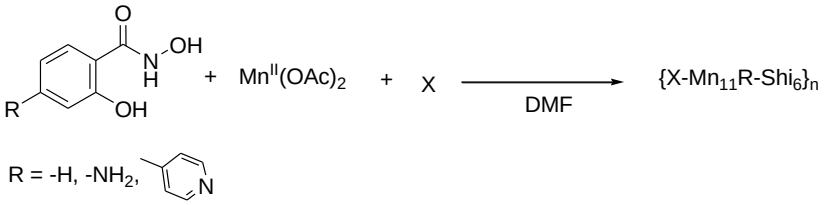

Scheme 3.1 Scheme of the reaction, leading to the X-Mn_{11}*p*-$RShi_6$ frameworks. R refers to the functionalization of the ligand, X indicates the alkali metals (i.e. Na^I, K^I, or Cs^I).

These five compounds show the same Mn_{11}-cage SBU, which has the $[(Mn^{II})_2(Mn^{III})_9(\mu^3\text{-}O)_4(p\text{R-Shi})_6(OAc)_3]^{2+}$ general formula. Additional acetate or hydroxide ions decorate the periphery of this polymetallic node, resulting in a "closed-shell" SBU. The inner core of the SBU is almost the same, being the effective joint. The linkage in 6-8 is due to additional alkali metal ions, in 7 the combination of external Na^I and the hooks placed onto the ligand itself (-NH_2) led the SBU to polymerize; finally, the -py functionalization allowed the SBU to be directly connected, without the involvement of any additional linkage, resulting in 10.

3.3. The Mn_{11}-cage joint

The structure of the SBU (Mn_{11}-cage), having general formula $[(Mn^{II})_2(Mn^{III})_9(\mu_3\text{-}O)_4(p\text{-RShi})_6(OAc)_3]^{2+}$, is complicated, thus a step by step description will be provided: starting from

the inner core to the external periphery. It is worth underline, that overall the Mn_{11}-cages show a molecular pseudo 3-fold symmetry axis.

Hence, the complex is a combination of different topologies, form which originate four description purposes: the Mn_{11}-cage as (I) a combination of $[Mn^{III}_3O_4]^{7+}$ units, (II) a metallacryptate, (III) an inverse metallacrown, and (IV) a polymetallic cluster, which resembles a three blades propeller (propeller-paradigm).

3.3.1 The Mn_{11}-cage joint as a system of Mn^{III} triangles

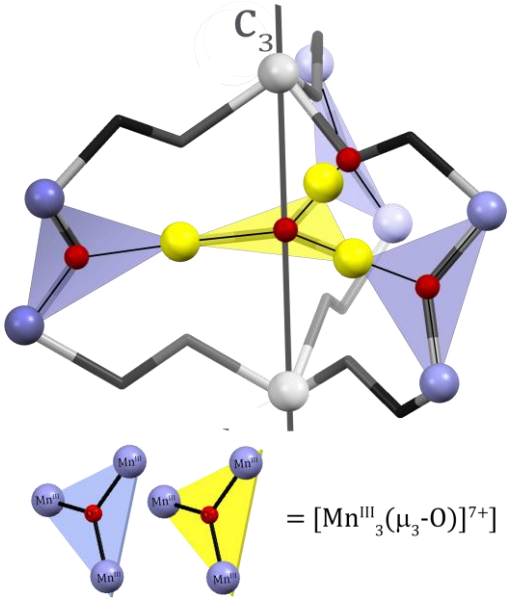

Figure 3.8 Description of the Mn_{11}-cage as a combination of four $[Mn^{III}_3O_4]^{7+}$ triangular units (T#), whose layout is here highlighted. The central triangle (T1) is yellow and three T2 units depart from it. (blue). The grey atoms correspond to the arms of the metallacryptate.

The inner core of the joint, is formed by a system of four $[Mn^{III}_3O_4]^{7+}$ triangular units (T#). In this perspective, all the four oxide ions of the Mn_{11}-cage sit in the center of a $[Mn^{III}_3O_4]^{7+}$ unit. The orientations of the four T# are well represented in **Figure 3.8**, where the central triangle, named T1 is drawn in yellow. Three T2 depart from T1. The latter is oriented perpendicular to the pseudo-C_3 axis, while T2 are in line with the axis and are related to the T1, by sharing one

of the Mn^{III} (i.e. Mn3). The orientation of T2 with respect to the axis and to the T1 plane depends from the specific X-Mn_{11}*p*-$RShi_6$., indeed the two Mn^{III} ions, which are not related to the T1, are somehow involved in the peripheral linkage.

On the molecular level, the fact that the overall Mn_{11}-cage is a composition of manganese triangles, may give rise to peculiar magnetic features. Indeed, a huge number of inorganic assemblies involving $[M_3(\mu_3\text{-}O)]^{n+}$ triangular systems is reported exhibiting interesting magnetic properties and some of them show single molecule magnetic behavior.[62–65]

3.3.2 The Mn_{11}-cage joint as a metallacryptate

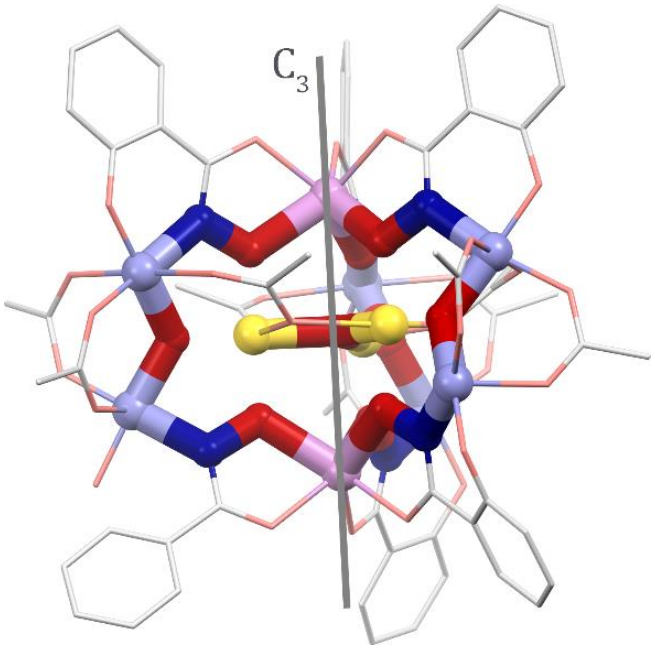

Figure 3.9 Description of the Mn_{11}-cage, following the metallacryptate topology. The $[(Mn^{II})_2(Mn^{III})_9(\mu^3\text{-}O)_4(p\text{R-Shi})_6(OAc)_3]^{2+}$ complex is reported and the metallacryptate arms are highlighted. The pseudo-C_3 molecular axis is lined in grey. The $[Mn^{III}{}_3O_4]^{7+}$ triangular units are omitted for clarity, except fot T1, which represents the guest of the Mcryp. Colors code: Mn^{III}-light blue if peripheral (T3), yellow if central (T1), Mn^{II}-pink; O-red; N-blue.

Following the metallacryptate topology, the Mn_{11}-cage shows the [3.3.3]metallacryptate (Mcrypt) topology. Here, the two Mn^{II} act as connection points of the metallacryptate and join

three identical arms. Each arm is formed by the Mn^{II}_{top}-O-N-Mn^{III}-O_{oxide}-Mn^{III}-N-O-Mn^{II}_{bottom} connectivity. Both Figure 3.9 and Figure 3.10-Center display the Mcrypt topology of the Mn_{11}-cage.

Associated to the Mcryp connectivity is the topology of the [1.1.1]orthoester cryptand (Figure 3.10, right).[66–68] This organic cryptand bears a R-C-O_3 connection points rather than a nitrogen as in Lehn-type cryptands (Figure 3.10, left), allowing the first and the fourth atoms of each arm to be two oxygens, rather than carbon atoms, like in Lehn-type cryptands.[69]

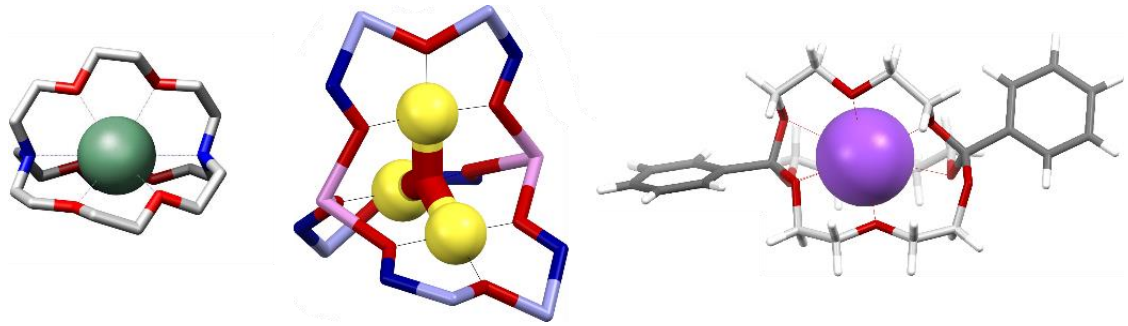

Figure 3.10 Structures respectively of the Lehn-type [2.2.2]cryptand (**left**), [70] of the Mn_{11}-cage with the M-crypt topology highlighted (**center**), and of the orthoester Mcryp-type (**right**).[68]

Therefore, if metallacrowns are the inorganic analogs of crown ethers, obtained by ideally replacing the CH_2-CH_2 chain with N and M atoms, the Mn_{11}-cage is the inorganic analog of [1.1.1]orthoester cryptates.[66–68] Moreover, by following the Mcrypt topology, the Mn_{11}joint sequesters the T1, which acts as a guest, coordinated within the Mcrypt central cavity.

3.3.3 The Mn_{11}-cage joint inverse-metallacrown topology

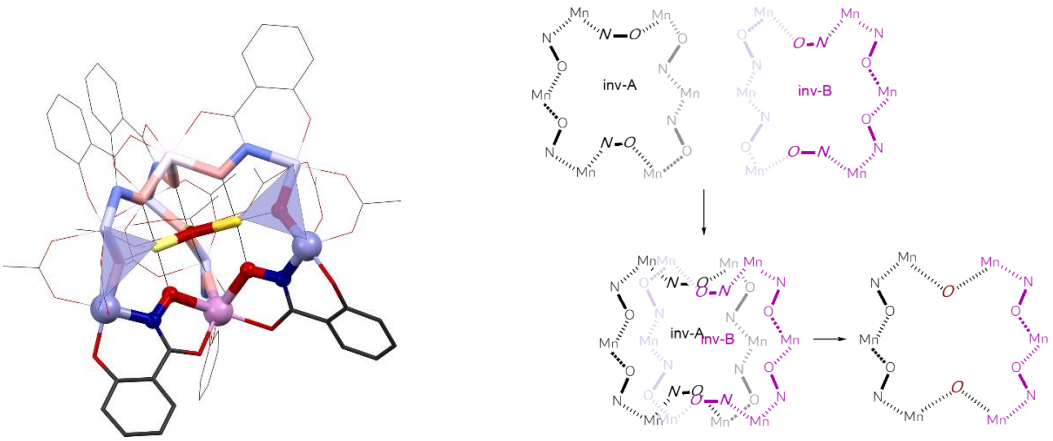

Figure 3.11 Description of the Mn_{11}-cage as an inverse metallacrown. **Left**: molecular structure, where the M-N-O connectivity is highlighted. **Right**: scheme of the conceptual fusion between the two specular helves of 18- *inv*MC-6.

The classical metallacrown connectivity is provided by the sequence M-N-O, highlighted in Figure 3.11. However, in classical MCs the linkage is consistently M-N-O-M-N-O, while here the linkage is transposed to M-N-O-M-O-N-. This connectivity is typical for inverse metallacrowns (*inv*MC, paragraph 1.1.6). By following the *inv*MC topology, the Mn_{11}-cage results by ideally fusing together two specular halves of a 18-*inv*MC-6. The representation of this ideal fusion is reported in Figure 3.11-Right, while the image on the left shows how the T2 units seem act as linkages of the two helves.

Actually the topology is not that of a traditional *inverse* metallacrown, because oxygen atoms, rather than Mn^{III} cations, are here oriented toward the central cavity.

3.4 The propeller paradigm

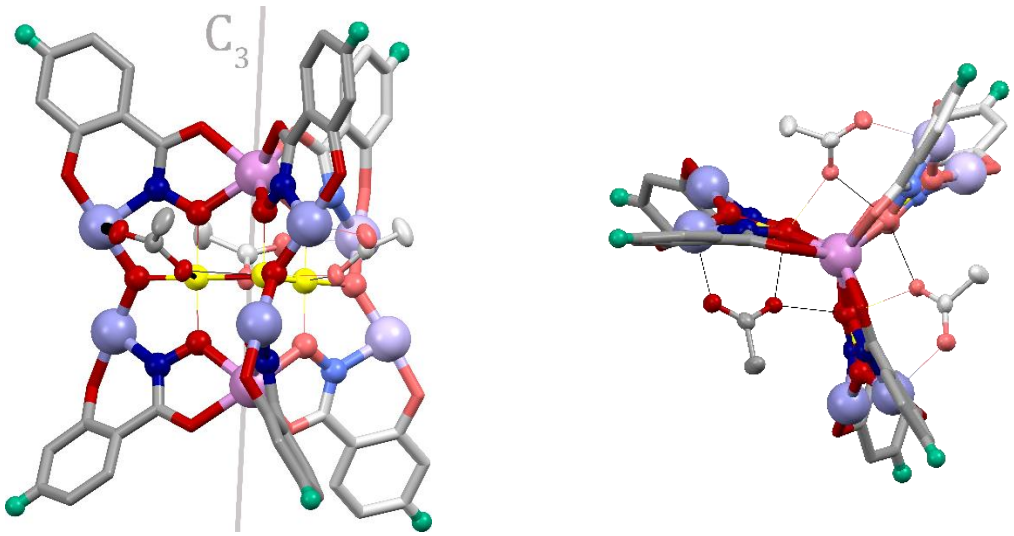

Figure 3.12 Structure of the $[(Mn^{II})_2(Mn^{III})_9(\mu^3\text{-}O)_4(OAc)_3(p\text{-}R\text{Shi})_6]^{2+}$ SBU, described as a polymetallic cluster, which resembles a three blades propeller (*propeller-paradigm*). The R positions in para to the hydroxamate are highlighted by emerald spheres (R = H, $-NH_2$, -py). The SBU is displayed along (**left**) and perpendicular (**right**) with respect to the molecular pseudo-C_3 axis (drawn in grey). Colours code: Mn^{II}-pink, Mn^{III} (T2)-light blue, Mn^{III} (T1)-yellow, N-dark blue, O-red, C-grey, R-emerald. OAc molecules are shown in ellipsoid style, the MC structural motif, that form the central cavity is highlighted by displaying atoms as spheres. Backside atoms are shown in light colours.

The complete SBU is reported in Figure 3.12. The top-view of the structure (Figure 3.12, right) suggests, that the architecture resembles a three-blade propeller, where the three blades are related by the pseudo-C_3 axis and the T1 is the hub of the propeller.

This topology point out how the position in para to the hydroxamate function are oriented outside the SBU. Hence it's reasonable to consider these metallacryptates as SBUs and to connect them by following the B-strategy. This way, the R-green-spheres are considered as hooks, from which the network can be developed.

3.5 The linkage modes

The Figure 3.13 illustrates the linkage modes found for the five X-Mn_{11}*p*-$RShi_6$ compounds. The top view of each SBU is displayed by reducing the overall joint to the three T2. As a consequence of the 2D layout of the picture, the T2 seems oriented perpendicular to the molecular pseudo-C_3,axis rather than tilted, thus pink arrows were drawn to indicate which vertex comes out of the sheet and which one goes into it.

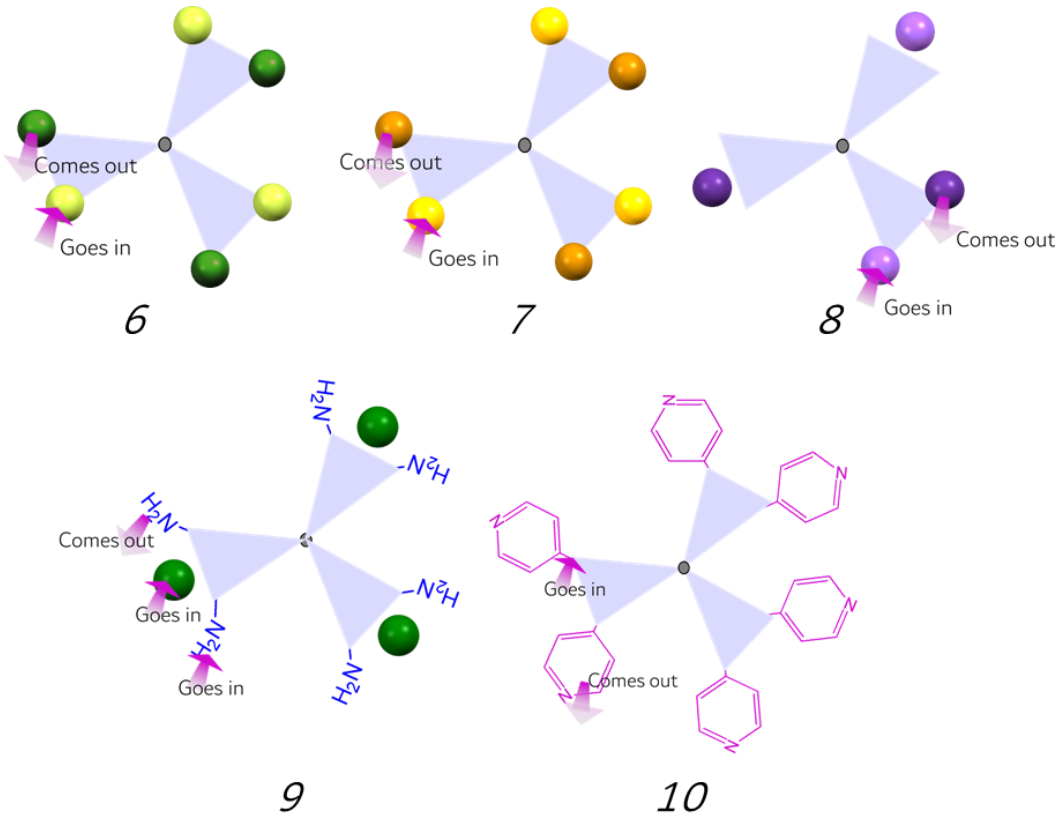

Figure 3.13 Schematic view of the 6-10 SBUs linkage modes. The SBUs are displayed highlighting the surrounding hooks, which assist the formation of the networks. Hooks color: Na-green, K-orange, Cs-purple. NH_2-blue and py-pink.

. As illustrated through Figure 3.13, 6-8 SBUs are joint by alkali metal ions, that bridge the Mn_{11}-cages by coordinating with one acetate and one Shi^{3-} at the edge of the blades. In 9 both

the Na^{I} linkage mode, and supramolecular interactions provided by the $-NH_2$ hook (and mediated by water molecules), contribute to the formation of the framework. Finally, 10 results from the formation of a coordinative bond directly between the N donor atom of the pyridyl hooks and one T2(Mn3) of the surrounding SBUs. A more detailed description follows (paragraph 3.6).

3.6 The Na-Mn_{11}*p*-$HShi_6$ network

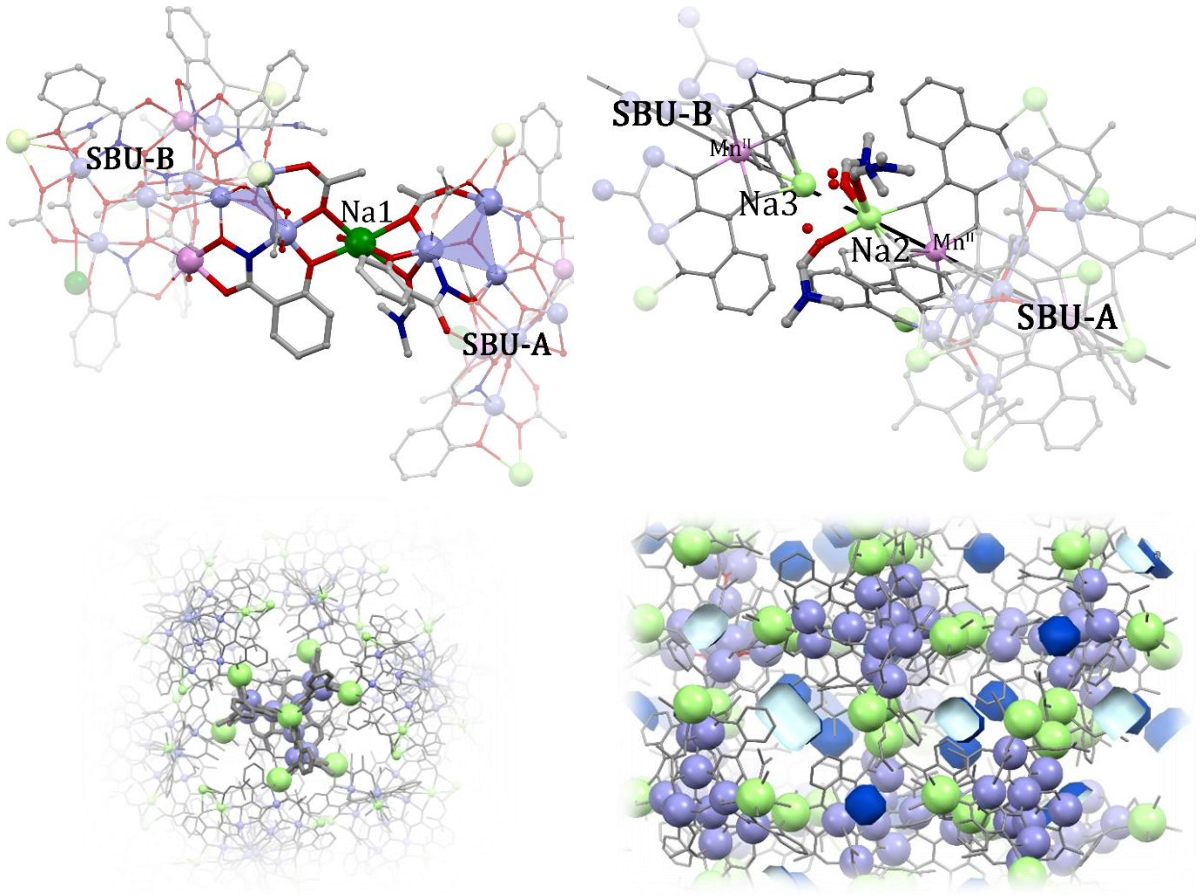

Figure 3.14 Top-left: the Na1 linkage mode. The T2 are drawn (light blue) to highlight the direction of the interactions. **Top-right:** the Na2 and Na3 coordination mode along the molecular pseudo-C_3 axis. **Bottom-left**: flattered octahedral coordination of the SBU via Na1, resulting in the network. **Bottom-right:** network of 6, where the calculated cavities are displayed (c.ca 1.6% empty volume). Color code: Na-green, Mn^{III}-light blue, Mn^{II}-pink, O and N highlighted atoms are red and blue respectively, C and not focused atoms are grey. Surface of the cavities is light and dark blue.

In network 6, each blade of the SBU connect two neighboring SBUs, thanks to the coordination of two Na^{I} (Na1) metal ions, which act as bridges. The Na1 linkage mode is reported in Figure 3.14, top-left: Na1 is hexacoordinated, three ligands come from the SBU-A and three from the SBU-B. In both cases the three ligands are one acetate(O), one shi^{3-}(O) and one DMF.

As mentioned in paragraph 3.5 and highlighted in Figure 3.13, the 6 SBU is surrounded by six Na1 cations. With respect to the SBU, the overall set of linkers are arranged in a flattened octahedral geometry, whose connections with six surrounding joints generate the overall framework (Figure 3.14, bottom-left). Along the direction of the molecular pseudo-C_3 axis and interacting with the Mn^{II} ions (Mn1 and Mn2), two disordered Na2 and Na3 sodium cations are placed. The occupancy of Na2 and Na3 was set 0.5, indicating that only one Na^{I} atom is alternatively coordinated at SBU-A(Na2) or SBU-B(Na3). The Na2 (or Na3) coordination environment is defined by disordered solvent molecules (i.e. three DMF or alternatively three water molecules, Figure 3.14, top-right). Moreover, Na2 and Na3 do not contribute to the construction of the framework, since they do not provide any bridging connection between symmetry related Mn_{11}-cages.

As far as it concern the porosity, 6 shows small interstitial cavities (Ø c.ca 6-7 Å), that correspond to c.ca 1.6% of empty volume (calculated with a sphere of 1.2 Å radius) and were found filled with solvent molecules, (Figure 3.14, bottom-right).

3.7 The K-Mn_{11}*p*-$HShi_6$ network

In network 7, the linkage is provided by potassium cations. Each SBU is surrounded by six K^{I} linkers, which bridge six neighbouring joints, like in 6. However, unlike 6, 7 SBUs are connected

also down the molecular pseudo-C_3 axis by two K^I ions (K1 and K1') interacting with the Mn^{II} ions (Mn1 and Mn1'). Indeed, K1 and K1', unlike Na2 and Na3, actively contribute to the framework, by linking two more joints. Possibly, the Na^I ion is smaller than K^I and the steric hindrance of the propeller does not allow the sodium to act as a bridge along the pseudo-C_3 axis direction. Thus, each SBU of 7 is surrounded by 8 neighbors.

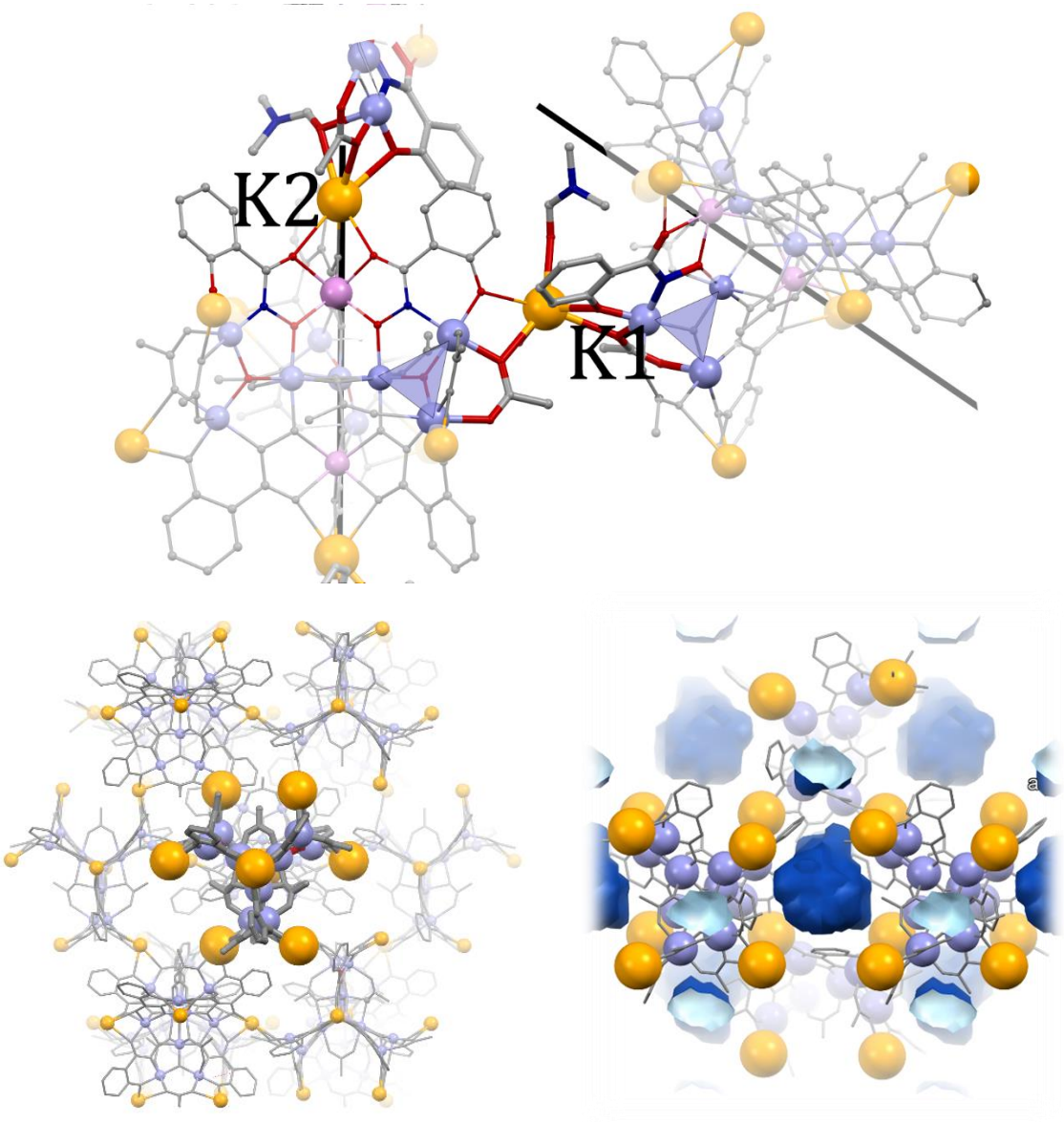

Figure 3.15 Top: K1 and K2 linkage modes, between symmetry related SBUs. **Bottom-left**: Flattered octahedral coordination of the SBU via K linkers. **Bottom-right:** calculated cavities within the 3D network (c.ca 6.9 % empty volume) for K-Mn_{11}*p*-$HShi_6$. Color code: K-orange, Mn^{III}-light blue, Mn^{II}-pink, O and N highlighted atoms are respectively red and blue, C and not focused atoms are grey. Surface of the cavities is light and dark blue.

K^{I} is hexacoordinated and shows the same coordination environment found for Na^{I} (i.e. one acetate(O), one ligand(O) and one DMF molecule from each of the two blades, **Figure 3.15**, top). As far as it concerns the porosity, 7 shows small interstitial cavities filled by disordered solvent molecules (i.e. water and DMF). Cavities are slightly larger than in 6 (Ø c.ca 8-10 Å) and correspond to 6.9% of empty volume within the unit cell (calculated with a sphere of 1.2 Å radius).

3.8 The Cs-Mn_{11}*p*-$HShi_6$ network

The use of the bigger Cs^{I} ions as bridging linkers, result in 8, which is a 2D-coordination polymer, rather than 6 and 7. The linkage modes provided by Cs^{I} are shown in Figure 3.16. Two of the three blades coordinate one Cs^{I} (Cs1, Cs4), rather than two cations like Na^{I} in 6 and K^{I} in 7. The third blade resembles those of 6 and 7 and coordinates two Cs^{I} ions (Cs1' and Cs4'). These four linkages take place down the *a* crystallographic direction, providing the formation of chains. Cs1 and Cs4 are hexacoordinated, two acetate molecules and one shi^{3-} are provided by the first SBU and the identical set of coordinative interactions is provided by the following one. The 2D layers grow down the pseudo-C_3 axis direction (Figure 3.16, right). Two Cs^{I} cations (Cs2 and Cs3) interact with the Mn^{II} ions (respectively Mn1 and Mn1', Figure 3.16, right). Also, both Cs2 and Cs3 form a Cs-Cs' tilted bridge (i.e. Cs2-Cs2' = 5.06 Å and Cs3-Cs3' = 4.86 Å), surrounded by coordinated DMF molecules. The tilting angle (Mn^{II}-Cs-Cs') is 117° degree both for Cs2 and C3 side. Thus, the pseudo-C_3 molecular axis of two following SBUs are parallel and 4.16 Å far. Along the third dimension, no interactions take place. The distance between layers is 7.3 Å.

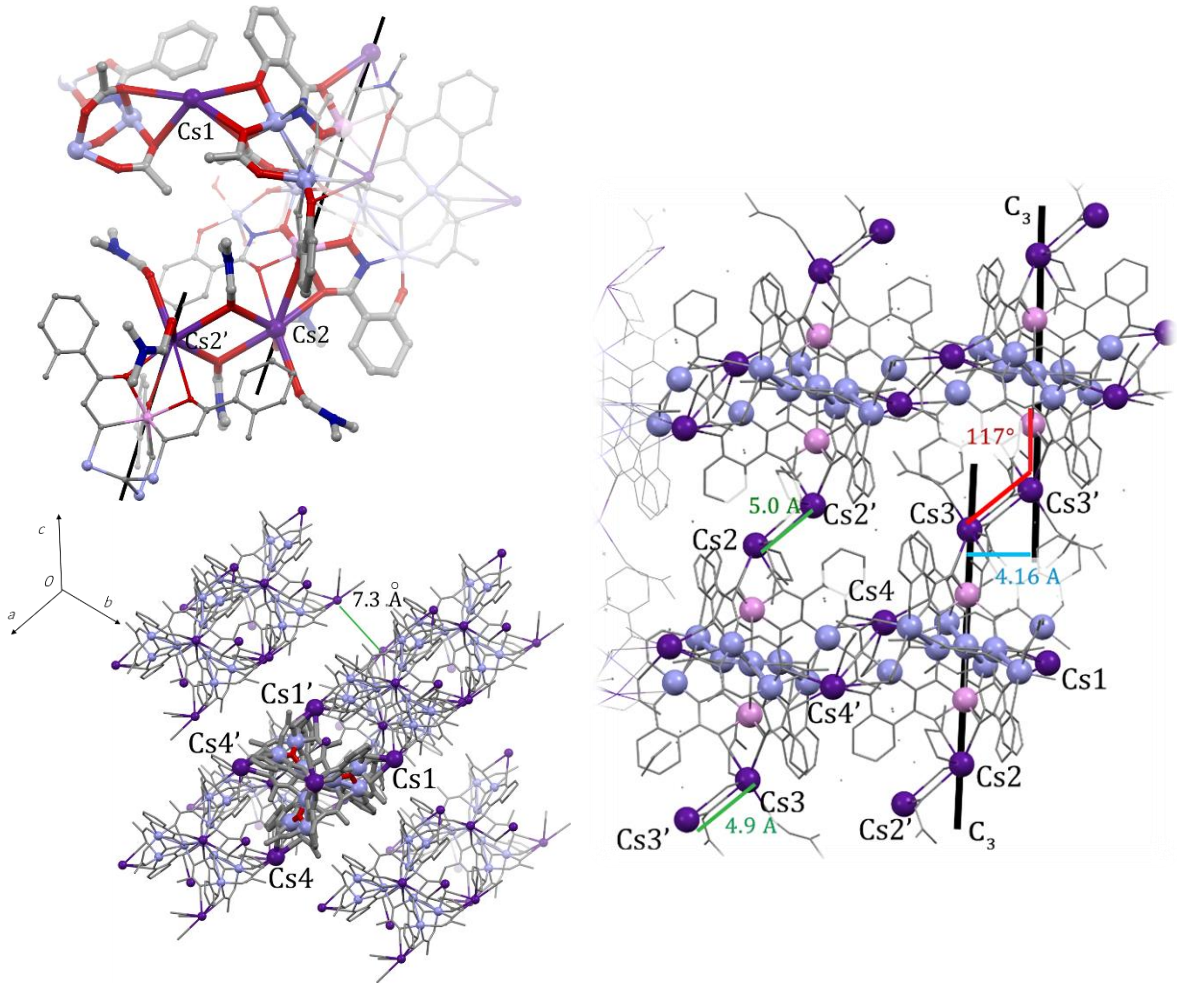

Figure 3.16 Top-left: linkage modes of Cs1 (equivalent to Cs4, Cs1' and Cs4') and of Cs2 (equivalent to Cs2', Cs3 and Cs3'). **Bottom-left**: top view of the 2D layers, the absence of interactions between layers is evident, the SBU is highlighted by larger sticks, Cs1 and Cs4 are coordinated to two different blades, Cs1' and Cs4' coordinate to the same blade. **Right**: the pseudo-C_3 axis direction of grow. The Cs-Cs bridge is highlighted. Distances and angles are reported as well. Colours code: Cs-purple-Mn^{III}-light blue, Mn^{II}-pink, O and N highlighted atoms are respectively red and blue, C and not focused atoms are grey.

3.9 The Na-Mn_{11}*p*-$aShi_6$ network

In network 9 the ligand is the *p*-$aShi^{3-}$derivative of the salicylhydroxamic acid. This means, that an amino hook was placed in para to the hydroxamic group. As anticipated in paragraph 3.5 and in Figure 3.13, the functionalization of the ligand, result in an SBU, which displays 6 amino (-NH_2) hooks pointing to the outside. As expected, the SBU of 9 forms a different set of

linkages and results in a 3D network significantly different than that of 6 (Figure 3.17), beside the presence of Na^{I} cations like in 6.

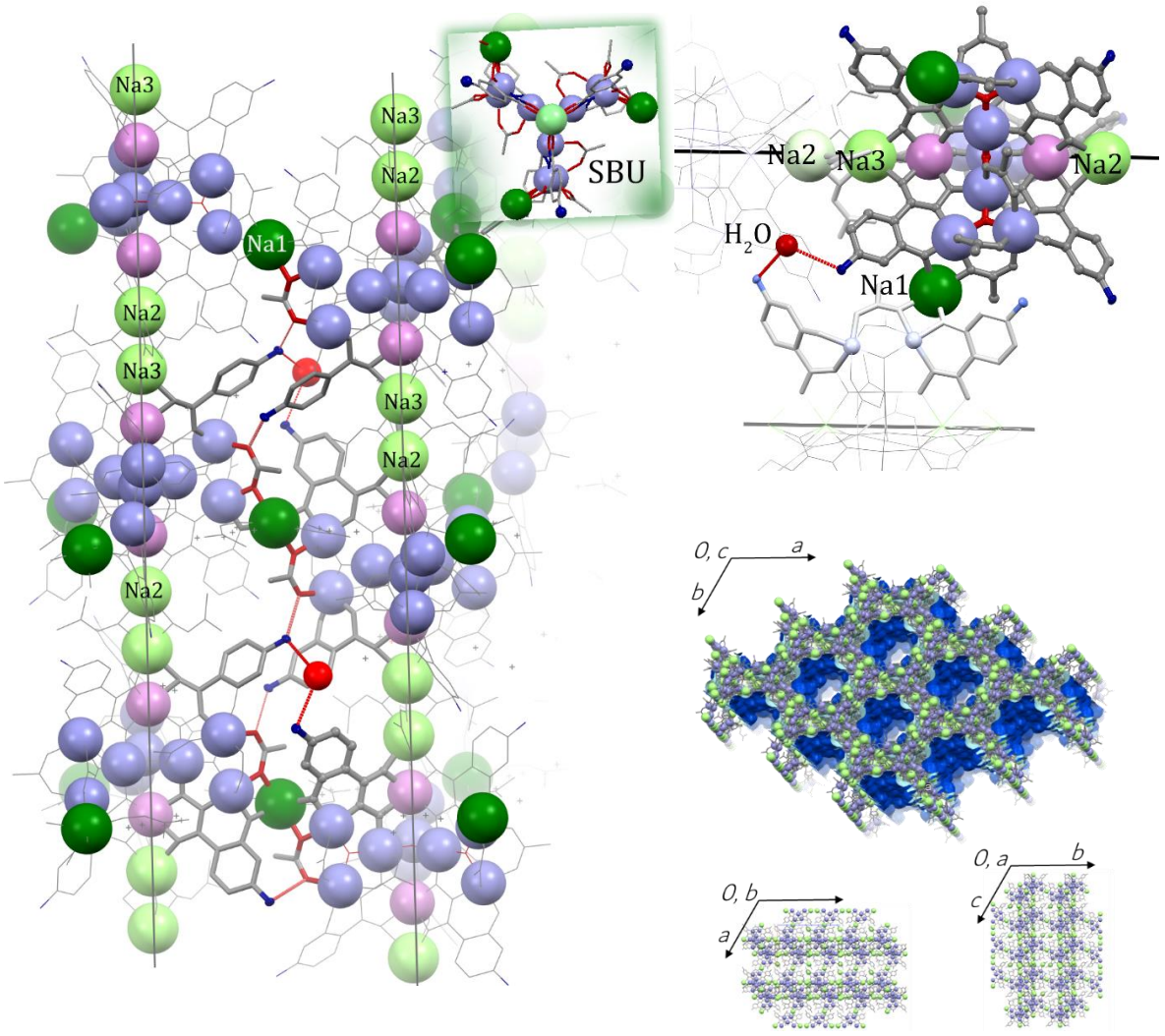

Figure 3.17 Left: interactions between adjacent SBUs in network 9. View down the crystallographic *c* axis. Dashed red lines represents hydrogen bonds. Colour code: Mn^{III}-light blue, Na1-dark green, Na2,Na3-light green, NH_2-hook-blue. The Na1 atoms bridge between blades of Mcrypt units from neighboring chains, similarly to 6. Na2 and Na3 atoms lie on the crystallographic *c* axis and bridge between SBUs through the $(Na2)(DMF)_3(Na3)$ moiety. **Bottom-right** structure of 9 in the three crystallographic projections. Color code: Mn-light blue, Na-green. The c view highlights the endless monodimensional channels. The surface of the channels is represented in blue.

Each blade of the M_{11}-cages generates three connections, one is in charge to Na^{I} (Na1) and two are generated by the two amino hooks. The Na1 interacts with one blade of the neighboring SBU, showing the same coordination environment reported for 6 (i.e. one acetate(O), one shi^{3-} (O) and one DMF).The Figure 3.17, top-right show the Na1 coordination environment except for DMF molecules that set behind the Na1 sphere and were omitted for clarity.

The two peripheral amino groups of *p*-$aShi^{3-}$ ligand lead to the formation of two braided extensive nets of supramolecular interactions. The connectivity, highlighted in Figure 3.17-left, follows:

... NH_2(H)-OAc(O)-Na-OAc(O)-NH_2(H)-H_2O(O,H)-NH_2(N)-etc ...

This supramolecular net results in parallel pillars of SBUs that grow along the c crystallographic direction. The linkage modes reported above describes the connections, which are oriented perpendicularly to the c axis, while down to the c direction the SBUs are connected by two more Na^{I} ions (Na2 and Na3), interacting with the Mn^{II} ions (Mn1 and Mn2) one side and forming one Na-Na bridge on the other one. Rather than in 6, Na2 and Na3 actively contribute to the framework (Figure 3.17, left).

Hence, each SBU provides eleven linkages, leading to the formation of endless 1D hexagonal channels, partially occupied by solvent molecules, and which correspond to 29% of the unit cell volume (calculated with a sphere of 1.2 Å radius).

3.10 The Mn_{11}*p*-$pyShi_6$ network

In network 10, the presence of the pyridyl fragment of *p*-$pyShi^{3-}$ leads to the formation of an extensive 3D framework, whose joints are represented by the metallacryptate reported in top-right corner of Figure 3.18. The *p*-$pyShi^{3-}$ ligand provides not only one N donor atom

pointing outside the SBU, like *p*-aShi^{3-}does, it is also longer and more rigid. The combination of these factors leads the pyridyl hook to coordinate with one of the apical positions of the Mn^{III} (i.e. Mn4), resulting in a network, without the involvement of any additional linker, rather than the ligand itself.

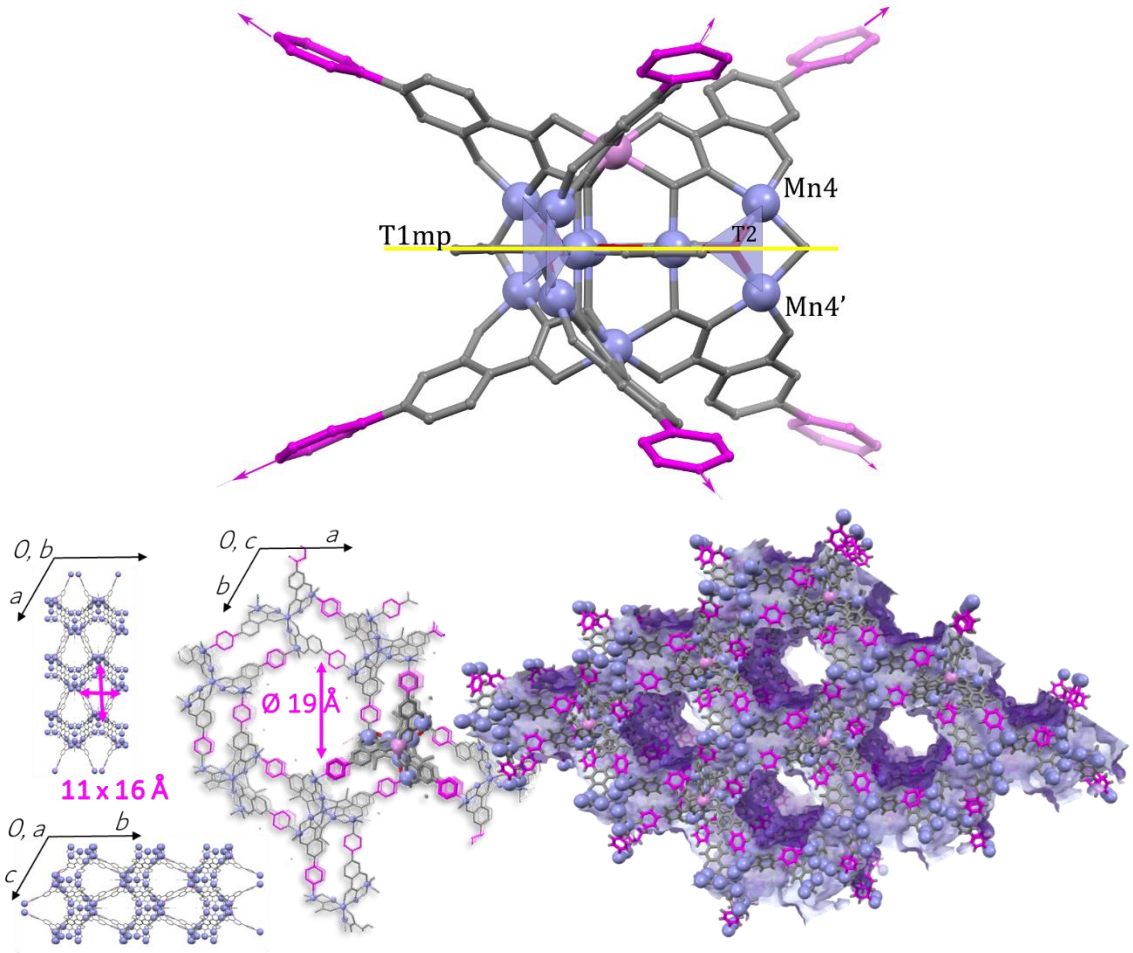

Figure 3.18 Representations of network 10. **Top**: The SBU, where the hooks are highlighted (pink), arrows mark the six linkages directions , departing from the SBU. The T2 triangles (light blue) and the T1 mean plane (T1mp, yellow) are traced. **Bottom:** View of the network and channels along the three crystallographic projections (**left**),. 3D-view of the hexagonal channels along the *c* crystallographic direction. The surface of the channels is represented in purple (**right**).

Each joint is connected to six neighboring ones, through twelve connections mediated by the pyridyl fragment. Six connections depart from the node (i.e. the ligand that form the SBU that coordinate Mn4 (or Mn4') ion on the opposite side ; Figure 3.18, top) and six come to the node

(i.e. the N-pyridyl functions of the neighboring SBUs, that coordinate at the Mn4). More specifically, the interaction between the six Mn_{11}*p*-pyShi_6 nodes occurs through a coordinative bond between the Mn4 (and Mn4') ion of T2 and the nitrogen of the peripheral pyridyl group. Six connections are diagonally directed above the T1 mean plane and six connections are oriented below the same plane. The six connections above the T1 mean plane are eclipsed with respect to those below T1. Among the six connections of each group, three come and three depart. The arrangement of the *p*-pyShi^{3-} ligands results in a hexagonal framework when viewed along the *c* crystallographic axis. The endless channel along the c direction has a 19 Å diameter and is partially occupied by disordered solvent molecules (i.e. water and DMF). Moreover, 10 shows channels along the *a* and *b* crystallographic directions as well. Those are smaller and present a trapezoidal section (Figure 3.18, bottom). These channels correspond to 55% of the unit cell volume (calculated with a sphere of 1.2 Å radius).

3.11 Distortions of the SBU along the X-Mn_{11}*p*-RShi_6 series

The five SBU present a very similar Mcrypt architecture and connectivity of the blades, although with significant differences. The position of the eleven Mn atoms is closely the same along the series, indeed the intraSBU distance between Mn^{II}-Mn^{II} (pink spheres, Figure 3.19) slightly decreases along the series between 6.23 Å (6) and 6.10 Å (10). These differences in cages length are a consequence of the different bridging modes provided by the alkali-metal ions, that assist the formation of the network along the molecular pseudo-C_3 axis. More evident are those distortions, that occur at the periphery of the blades, experienced by the ligands and by the acetate molecules (i.e. the counterions). Indeed, while the blades in 6, 7 and 9 are nearly planar, that of 8 is significantly distorted and that of 10 is clearly domed (Figure 3.19).

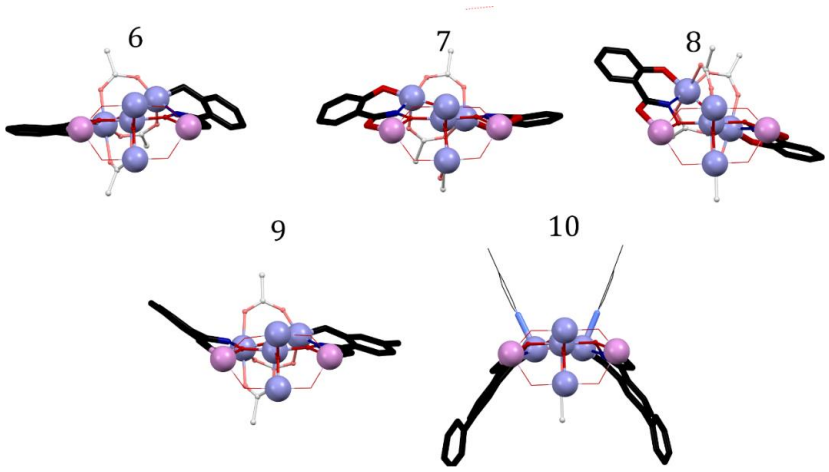

Figure 3.19 Structures of the 6-10 blades, highlighting the distortions that occur along the series, especially to the ligand periphery. The molecular pseudo-C_3 axis are oriented horizontal. Color code: Mn^{II}-pink, Mn^{III}-light blue, and ligands bold-black. In 10 the Mn4-N linkage is shown as well, above the blade (bold light blue and first phenyl group).

The distortions experienced by the ligands, slightly modify the orientation of T2. The consequence is the different coordination geometry and environment of the acetates coordinated to the core of the SBU (**Figure 3.20**). Two general modes are found: the acetate interacts both with T1 and T2 in 6, 8 and 10, AcO^- interact only with T1 in 7 and is bound only to T2 in 9.

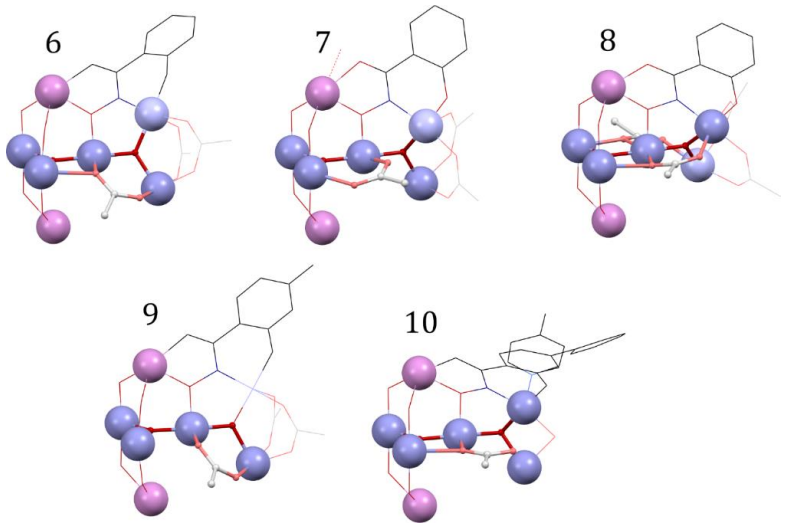

Figure 3.20 Portion of the 6-8 SBU, which highlights the coordination modes of the acetates coordinated to the T1. Two general modes are found: the acetate interacts both with T1 and T2 in 6, 8 and 10, AcO^- interact only with T1 in 7 and is bound only to T2 in 9.

Conclusions

In this work it has been demonstrated the possibility to obtain five different three-dimensional networks starting from the same SBU and by modifying its periphery. In particular the combination of three different salicyhydroxamate derivatives (*p*-$RShi^{3-}$) as ligands and manganese(II) acetate as metal ion source lead to the formation of the same polymetallic SBU, while the decoration of the ligand periphery in para position with respect to the hydroxamic group and by modulating the bridging linkers (i.e. changing the alkali-metal ions size), five new networks based on the same endeca-manganese polymetallic joints were found

The Secondary Building Units are endeca-manganese complexes, which have general formula $[(Mn^{II})_2(Mn^{III})_9(\mu_3\text{-}O)_4(p\text{-}RShi)_6(OAc)_3]^{2+}$. The so called Mn_{11}-cage can be described by following four different topologies. First it can be seen as a combination of four $[Mn^{III}_3O_4]^{7+}$ units, where one to the four is in the center and the other three are related to the first. Second, the Mn_{11}-cage can be seen as a [3.3.3]metallacryptate, made of three identical arms and incapsulating a $[M_3(\mu_3\text{-}O)]^{n+}$ triangular unit as guest. Third the complex can be described following the topology of inverse metallacrowns and in this case, the five new networks might be promising for the investigation of the magnetic properties, since many inverse metallacrowns have been found having peculiar magnetic behaviour, including single molecule magnetic features. Finally, the complicated architecture of this polymetallic cluster, resembles that of a propeller. Indeed four to the five SBUs present three identical blades and the 8 compound present two identical blades and a slightly different third one.

Overall the five Mn_{11}-cages are mixed valence metallacryptates, since among the eleven Mn ions two are bivalent (Mn^{II}) and nine are trivalent (Mn^{III}). These molecules present the same

connectivity along the series and, at least for what concerns the position of the metal atoms, the five SBUs show also the same geometry.

Five different modification of the periphery of the SBU were performed, following the so called B-strategy for the construction of MC networks.

Thus, the linkage modes experienced by the SBU has been tuned, resulting in five different coordination polymers. By using the same ligand (i.e. salicylhydroxamate, shi^{3-}) it was possible to change the connection mode by increasing the size of the cationic linker (from Na^{I}, to K^{I} and Cs^{I}). Using Na^{I}, and K^{I}, three-dimensional coordination polymers were found. These two materials are tightly packed, show small interstitial cavities and both the networks involve solvent molecules in the metal ions coordination spheres. The largest cationic linker (Cs^{I}) produced a 2D networks.

However, the most interesting results have been found through the functionalization of the ligand. Indeed, two new derivatives of the salicylhydroxamic acid were designed and synthetized, by placing two coordinative functions in para to the hydroxamic group. Hence, *p*-$aShi^{3-}$ shows an amino hook and *p*-$pyShi^{3-}$ a pyridyl one, both capable to connect SBUs, forming respectively supramolecular and coordinative interactions.

The crystal structure of the last two materials is characterized by the Mn_{11}-cage SBU, which arranges in three-dimensional coordination polymers containing potential accessible voids. The amino hook led the SBUs to generate eleven connections, five of them provided by the coordination of sodium bridging linkers and six are supramolecular interactions provided by the hook itself. The *p*-$pyShi^{3-}$ derivative on the other hand leads the SBU to generate twelve interactions. Six of them are provided by the ligands themselves and the other six are received

by the surrounding SBUs. Indeed each N donor atom of the pyridyl hook is capable to coordinate with one manganese(III) of the neighbouring propeller.

Both the *p*-aShi^{3-} and *p*-pyShi^{3} Mn_{11}-cages result in honeycomb architectures. The first allows the formation of monodimensional channels, while the second assemble in a framework which has three-dimensional channels.

The present results are extremely interesting firstly because represent a proof of the concept, that it is possible to connect metallacrowns, resulting in three-dimensional arrays containing potential voids. Also, because it is a demonstration that a wise design of the ligand allows to predict to some extent the final compound.

The large interest of the results discussed in this section of the present dissertation have been awarded by the IUCr International Scientific Union. Indeed the poster entitled "Engeneering novel poruos 3D metallacrown-frameworks, through the ligand periphery design" has been awarded of the IUCr Journals Poster Prize for Structural Chemistry, the last August 2018 at the 31st Meeting of the European Crystallographic Association (Oviedo, Spain).

In the future, the thermal stability profiles will be firstly investigated, to clarify if the three-dimensional architectures survive the evacuation of the solvent molecules, or if they experience the collapse of the three-dimensionality. These analyses should be followed by the investigation of the sorption properties, especially in case of compounds 9 and 10, to understand if they show permanent porosity and to determine the surface area.

Finally, it will be interesting to study the magnetic behaviour of overall the compounds and perhaps if the different linkage modes tune the magnetic properties as well.

Experimental

Materials and methods – Chemicals and solvents were purchased from commercially available sources and used without further purification. Reactions performed under an inert atmosphere, were carried out using Schlenk glassware and nitrogen as the inert gas. Flash column chromatography was performed using silica gel (230-400 mesh).

^{1}H NMR spectra, of vacuum dried samples, were recorded on Bruker Advance 400, Varian MR400 and Varian Vnmrs500 spectrometers using standard pulse sequences. Chemical shifts are reported in part per million (ppm) and were referenced to the residual signals of the solvents. The following abbreviations are used in reporting the multiplicity for NMR resonances: s=single, d=doublet, dd= doublet of doublet, t= triplet, and m=multiplet. MestReNova software package was used to process and analyze data and to plot the spectra.

Electrospray ionization mass spectra (ESI-MS) of compounds 2-5 were collected on a Micromass LCT TOF electrospray ionization mass spectrometer, using a capillary voltage of 3500 and a desolvation temperature of 350 ºC. Samples (40 µM) were injected through direct infusion using a syringe pump at 11 µl/min, and the spectra recorded in full scan analysis mode in the range 100-2000 *m/z*. MestReNova software package was used to process and analyze data and to plot the spectra.

Infrared Spectroscopy (IR) spectra were collected on vacuum dried samples with a Thermo Scientific Nicolet 5PCFT-IR-ATR spectrometer equipped with diamond crystal (4000-400 cm^{-1} interval).

Single crystal X-Ray diffraction data of 6 were collected at 293 K on a Bruker Smart APEXII CCD diffractometer (Mo Ka; l = 0.71073 Å). Intensities were integrated from several series of exposure frames that covered the sphere of reciprocal space.[71] Single crystal X-Ray diffraction

data of 7 were collected at 200 K on a Bruker d8 PhotonII area detector X-Ray diffractometer (Mo Ka; l = 0.71073 Å) equipped with a low temperature device.

Single crystal X Ray diffraction data of 8 were performed at Elettra Syncrotron (Trieste, Italy) on beamline XRD1[72] at 100 K by mean of an Oxford Cryostream. The source used for the analysis was a NdBFe Multipole Wiggler (Hybrid linear), 4.27 keV with a power of 8.6 kW, a source size FWHM of 2.0×0.37mm (0.7×0.2 mm FWHM beam size at sample) and photon flux 10^{12}–10^{13} phs^{-1}. 8 crystals were taken from the mother liquor and mounted with cryoloops (0.05–0.3 mm), prior to flash freezing at 100 K. Diffraction data were indexed, integrated, and scaled using CrysAlis software.[73] Single crystal X Ray diffraction data of 9 and 10 were collected with a Rigaku AFC10K Saturn 944+ CCD-based X-Ray diffractometer equipped with a low temperature device and Micromax-007HF Cu-target micro-focus rotating anode (λ = 1.54187 A) operated at 1.2 kW power (40 kV, 30 mA). Rigaku d*trek images were exported to CrysAlisPro for processing.[73] Absorption correction was applied using the program SADABS.[74] The structures of compounds 6-10 were solved by direct methods ShelXT,[75] and refined with full-matrix least squares,[76] using the Olex2 software package. The structures were analysed with the Mercury 3.10 software package.[77] Crystallographic data for 6, 9 and 10 reported in this dissertation have been deposited with the Cambridge Crystallographic Data Centre (the deposition CCDC number for are respectively 1849184, 1849185 and 1849186).

Ligand synthesis

Synthesis of 4-aminosalicylhydroxamic acid (H_3*p*-aShi, 5). – The synthetic procedure for ligand **5** is reported in **Scheme 3.2** (optimization of a previously reported route for the synthesis of hydroxamic acids).[78]

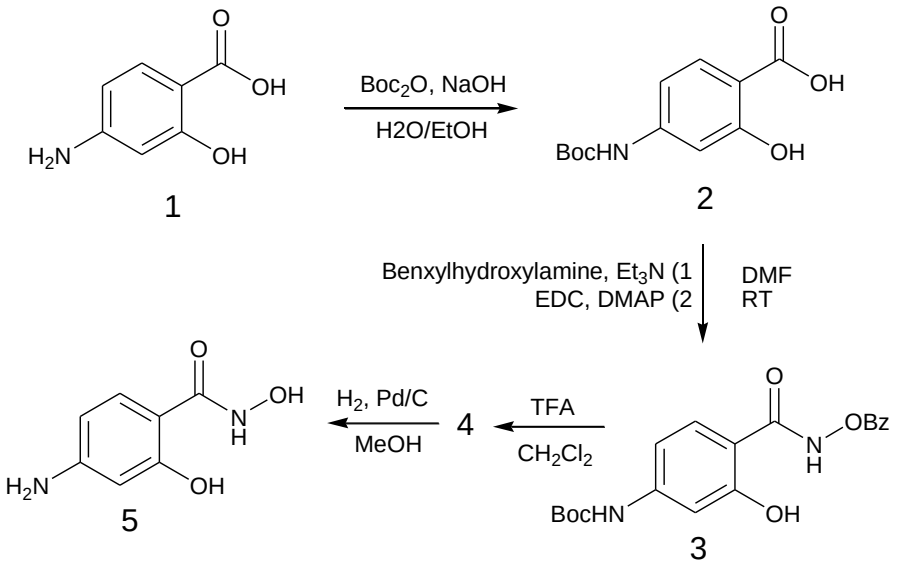

Scheme 3.2 Synthetic route for the preparation of the H_3*p*-aShi ligand (**5**)

Synthesis of N-*t*-butyloxycarbonyl-4-aminosalicylic acid (2) – 4-aminosalicylic acid (**1**, 4.0 g, 0.026 mol) was dissolved in 50 mL of ethanol. Sodium hydroxide (2.1 g, 0.052 mol), dissolved in 20 mL of water, was added. Di-*t*-butyl dicarbonate (11.4 g, 0.052 mol), dissolved in 40 mL of ethanol, was added dropwise within 1 hour, and the solution stirred overnight. The solvent was removed *in vacuo* and hydrochloric acid (1 M) was added up to pH = 3. The precipitate was filtered off, washed with water, and dried under reduced pressure at room temperature to obtain a white powder (3.7 g, 93 %). FT-IR (ATR) ν_{max}/cm^{-1}: 3361m, 2884w, 1737s, 1621s, 1588s, 1452s, 1298s, 1220s, 1192m, 1138vs, 1048m, 1023m, 984w, 914w, 872s, 826m, 775s, 699w, 643vs, 596m, 540m, 504m, 464m. ^{1}H NMR (400 MHz, DMSO-d_6) δ 9.71 (1H, s, Ar-NH), 7.64 (1H , d, $J_{6,1}$ 8.7 Hz, Ar-6H), 7.12 (1H, d, $J_{3,1}$ 2.1 Hz, Ar-3H), 6.98 (1H, dd, $J_{1,6}$ 8.8, $J_{1,3}$ 2.1 Hz, Ar-1H), 1.47 (9H, s, Boc-CH_3). (ESI-QTOF): *m/z* 276.25$[M+Na]^+$; 292.21 $[M+K]^+$. Elemental analysis found: C, 56.8; H, 6.2; N, 5.6. Calc for $C_{12}H_{15}NO_5$: C, 56.9; H, 6.0; N, 5.5%.

Synthesis of N-*t*-butyloxycarbonyl-4-aminosalicyl-O-benzylhydroxamate (3) – Compound **2** (5.00 g, 0.0198 mol) was dissolved in 120 mL of DMF. Triethylamine (5.5 mL, 0.0395 mol), *O*-

benzylhydroxylamine hydrochloride (6.3 g, 0.040 mol), EDC hydrochloride (4.54 g, 0.0395 mol) and DMAP (0.30 g, 0.0024 mol) were added to the reaction mixture in this order. The resulting mixture was stirred for 48 hours at room temperature. DMF was removed under reduced pressure, and the resulting yellowish oil diluted with ethyl acetate (50 mL). The organic phase was washed with a saturated $NaHCO_3$ solution (3 x 50 mL), brine and then dried with anhydrous Na_2SO_4. The solvent was removed *in vacuo* and the product purified by flash column chromatography (silica gel, ethyl acetate/hexane 1:1 as the eluent). Pure compound **3** was isolated as a brownish powder (2.74 g, 40 %). ^{1}H NMR (400 MHz, DMSO-d_6) δ 11.98 (1H, s, OBz-OH), 11.66 (1H, s, Ar-OH), 9.60 (1H, s, Ar-NH), 7.55 (1H, d, $J_{6,1}$ 8.7 Hz, Ar-6H), 7.42 (5H, m, OBz-H), 7.13 (1H, s, Ar-3H), 6.92 (1H, d, $J_{1,6}$ 8.7 Hz, Ar-1H), 4.92 (2H, s, OBz-CH_2). (ESI-QTOF): *m/z* 737.28 $[(M-H)_2Na]^-$. Elemental analysis found: C, 63.4; H, 6.3; N, 7.7. Calc for $C_{19}H_{22}N_2O_5$: C, 63.7; H, 6.2; N, 7.8%.

Synthesis of 4-aminosalicyl-*O*-benzylhydroxamate (4) – Compound **3** (2.09 g, 5.83 mmol) was dissolved in a dichloromethane/TFA mixture (1:1 *v:v*), and the solution stirred for 2 hours at room temperature. The solvent was removed *in vacuo*. The resulting oil was dissolved in 50 mL of ethyl acetate, washed with water (3 x 50 mL), brine, and treated with anhydrous Na_2SO_4. The solvent was removed *in vacuo*, yielding compound **4** as a brownish powder (1.9 g, 91 %,). ν_{max}/cm^{-1}: 2859m, 2603m, 1611vs, 1543m, 1497m, 1472w, 1430m, 1389w, 1321w, 1255w, 1196s, 1142vs, 1109s, 1017m, 974m, 840w, 906w, 857w, 823w, 796m, 734s, 717s, 695s, 602s, 570w, 539w, 517w, 492w. ^{1}H NMR (400 MHz, DMSO-d_6) δ 7.49 – 7.26 (7H, m, OBz-H + Ar-1H), 6.03 (1H, d, $J_{6,1}$ 9.7 Hz, Ar-6H), 5.96 (s, 1H, Ar-3H), 5.79 (2H, s, Ar-NH_2), 4.88 (2H, s, Ar-NH_2). (ESI-QTOF): *m/z* 281.22 $[M+Na]^+$; 297.25 $[M+K]^+$; 539.25 $[M_2+Na]^+$. Elemental analysis found: C, 65.4; H, 5.4; N, 10.6. Calc for $C_{14}H_{14}N_2O_3$: C, 65.1; H, 5.5; N, 10.8%.

Synthesis of 4-aminosalicylhydroxamic acid (H_3p-aShi, 5) – The compound **4** (0.120 g, 0.464 mmol) was dissolved in 60 mL of methanol and hydrogenated in the presence of Pd/C (0.018 g, 15% w/w) under H_2 (p_{H2} = 30 psi) for 24 hours. The catalyst was filtered off from the pale pink solution, the solvent removed *in vacuo*, and pure H_3p-aShi (**5**) isolated as a dark red powder (0.050 g, 92 %). ^{1}H NMR (400 MHz, DMSO-d_6) δ 7.32 (1H, d, $J_{6,1}$ 8.6 Hz, Ar-6H), 6.00 (1H, dd, $J_{1,6}$ 8.6, $J_{1,3}$ 2.2 Hz, Ar-3H), 5.94 (1H, d, $J_{3,1}$ 2.2 Hz, Ar-3H), 5.71 (2H, s, Ar-NH_2). ESI-QTOF): *m/z* 169.06 $[M+H]^+$. Elemental analysis found: C, 50.3; H, 4.9; N, 16.4. Calc for $C_7H_8N_2O_3$: C, 50.0; H, 4.8; N, 16.7%.

Synthesis of 4-(pyridin-4-yl)-salicylhydroxamic acid (H_3p-pyShi) – The synthesis of 4-(pyridin-4-yl)-salicylhydroxamic acid (H_3p-pyShi) was optimized by the group of Giulia Licini at the University of Padova. The route finally proposed is reported in **Scheme 3.3**.

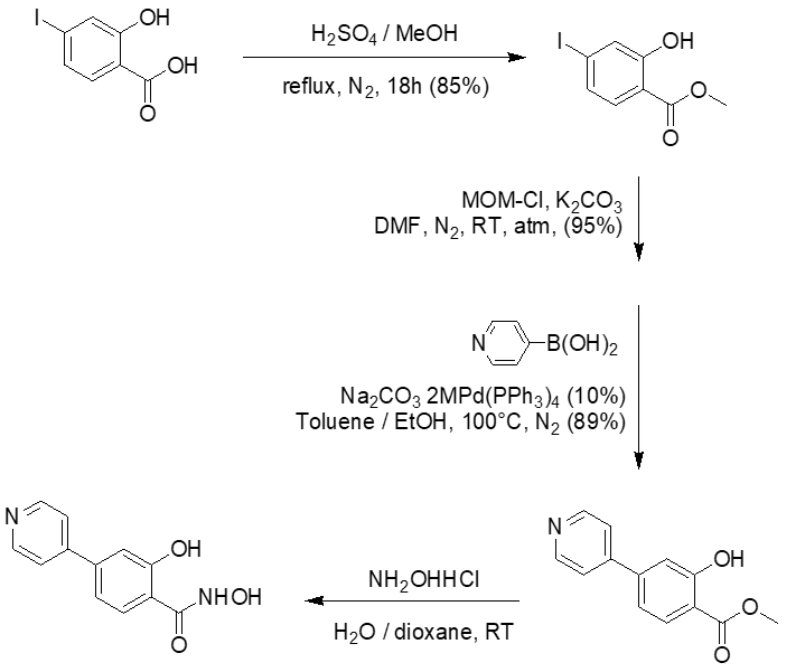

Scheme 3.3 Synthetic route proposed for the preparation of the H_3p-pyShi ligand

Synthesis of the X-$Mn_{11}L_6$ metallacryptates

General comments – The synthetic procedures for the X-$Mn_{11}L_6$ metallacryptates were optimized by modifying a previously reported route, purposed by C. Atzeri in his PhD dissertation.[79] The novel strategy for the preparation of the Na-$Mn_{11}Shi_6$ material allowed to avoid two main difficulties experienced by Atzeri: first the undesired crystallization of the previously reported $Mn^{II}[12\text{-}MC_{MnIII,(O)H3Shi\text{-}3H}\text{-}4](OAc)_2$ species instead of the Mn_{11}-cage, second, the co-crystallization of sodium acetate as by-product.[80] The synthesis of the K-$Mn_{11}Shi_6$ metallacryptate is more straightforward and easily crystallize. Whereas, the Cs^I species gives small, deliquescent and aggregated or geminated crystals, affecting the X-Ray diffraction data. The reaction of manganese acetate with the H_3*p*-aShi_6 ligand, gives the $Mn^{II}[12\text{-}MC_{MnIII,(O)H3p\text{-}aShi\text{-}3H}\text{-}4](OAc)_2$ more frequently than the sibling H_3Shi_6. The $Mn^{II}[12\text{-}MC_{MnIII,(O)H3p\text{-}aShi\text{-}3H}\text{-}4](OAc)_2$ species is novel in literature and is isostructural to the previously reported $Mn^{II}[12\text{-}MC_{MnIII,(O)H3Shi\text{-}3H}\text{-}4](OAc)_2$ complex (see Figure S8 and Table S8, Supplementary Materials, respectively for X-Ray structure and crystallographic data). Finally, the synthesis of the Mn_{11}*p*-pyShi_6 give very low yields of pure crystals after one month.

Synthesis of $Na_4[(Mn^{II})_2(Mn^{III})_9(\mu^3\text{-}O)_4(OAc)_9(Shi)_6(DMF)_3](DMF)_3(H_2O)_{6.75}$ (Na-$Mn_{11}Shi_6$, 6) – Manganese(II) acetate tetrahydrate (0.435 g, 1.76 mmol) and the H_3Shi ligand (0.100 g, 0.65 mmol) were dissolved in 5 mL DMF, previously heated at 50°C. The resulting mixture was stirred for 15 minutes, keeping the system at 50°C. Sodium chloride (0.008 g, 0.14 mmol) was dissolved in the minimum quantity of H_2O and added to the solution, under stirring. The resulting dark brown solution was stirred for four hours and centrifuged to remove the impurities. The supernatant (1.5 mL) was crystallized by stratification of toluene (3 mL) in a 10

mL tubes in the fridge. The diffusion of the toluene gave dark brown crystals suitable for XRD analysis within 1 month, with yields variable from 20 to 40%.

Synthesis of $K_4[(Mn^{II})_2(Mn^{III})_9(\mu_3\text{-}O)_4(OAc)_3(Shi)_6(OAc)_6](DMF)_4(H_2O)_4(DMF)$ (K-$Mn_{11}Shi_6$, 7) and $Cs_4[(Mn^{II})_2(Mn^{III})_9(\mu_3\text{-}O)_4(OAc)_3(Shi)_6(OAc)_6](DMF)_6(H_2O)_x$ (Cs-$Mn_{11}Shi_6$ 8) – Manganese(II) acetate tetrahydrate (0.122 g, 0.50 mmol) and the H_3Shi ligand (0.032 g, 0.21 mmol) were singly dissolved in 1 mL DMF. The solution of the ligand was heated at 50°C, then the Mn solution was added. The resulting mixture was stirred for 15 minutes, keeping the system at 50°C. X chloride (where X = K^I, Cs^I; 0.030 g of KCl or 0.067 g of CsCl, 0.4 mmol) was dissolved in the minimum quantity of water and added to the Mn-Shi solution. 8 mL of methanol were added to the resulting dark brown solution, that was kept under stirring overnight and then centrifuged to remove insoluble impurities. Slow evaporation of the supernatant at room temperature gave dark brown crystals suitable for XRD analysis within one week, with yields variable from 12 to 28%.

Synthesis of $Na_{3.5}H_{0.5}[(Mn^{II})_2(Mn^{III})_9(\mu^3\text{-}O)_4(OAc)_9(p\text{-}aShi)_6](DMF)_{7.5}(H_2O)_6$ (Na-$Mn_{11}p$-$aShi_6$, 9) – Manganese(II) acetate tetrahydrate (0.061 g, 0.25 mmol), the H_3p-aShi ligand (0.017 g 0.1 mmol) and sodium acetate trihydrate (0.014 g, 0.1 mmol) were dissolved in 2 mL DMF each. The three solution were mixed under stirring, following the order: manganese(II) acetate, H_3p-aShi and sodium acetate. The resulting dark brown solution was kept under stirring for 4 hours and then centrifuged to remove insoluble impurities. Slow evaporation of the supernatant at room temperature gave dark brown crystals suitable for XRD analysis within four weeks, with yields of 5%.

Synthesis of $H[(Mn^{II})_2(Mn^{III})_9(\mu^3\text{-}O)_4(OAc)_3(OH)_3(p\text{-pyShi})_6](H_2O)_6$ ($Mn_{11}p$-pyShi$_6$, 10) – The H_3p-pyShi ligand (0.023 g, 0.1 mmol) was dissolved in 5 mL DMF. Potassium chloride (0.008 g, 0.1 mmol) was dissolved in distilled water and added to the ligand. The solution was heated at 50°C, then manganese(II) acetate tetrahydrate (0.061 g, 0.25 mmol) was added as solid, under stirring. The resulting dark brown solution was stirred for 2 hours at room temperature and centrifuged to remove insoluble impurities. Slow evaporation of the supernatant at room temperature gave dark brown crystals suitable for XRD analysis within four weeks, with 8% yields.

Biblioghraphy

1. Zhou H-C, Long JR, Yaghi OM. Introduction to Metal–Organic Frameworks. Chem Rev. 2012;112(2):673-674. doi:10.1021/cr300014x
2. Zhou H-C "Joe", Kitagawa S. Metal–Organic Frameworks (MOFs). Chem Soc Rev. 2014;43(16):5415-5418. doi:10.1039/C4CS90059F
3. Batten SR, Champness NR, Chen X-M, et al. Coordination polymers, metal–organic frameworks and the need for terminology guidelines. CrystEngComm. 2012;14(9):3001-3004. doi:10.1039/c2ce06488j
4. Jiang J, Zhao Y, Yaghi OM. Covalent Chemistry beyond Molecules. J Am Chem Soc. 2016;138(10):3255-3265. doi:10.1021/jacs.5b10666
5. Janiak C, Vieth JK. MOFs, MILs and more: concepts, properties and applications for porous coordination networks (PCNs). New J Chem. 2010;34(11):2366-2388. doi:10.1039/c0nj00275e
6. Fujita D, Ueda Y, Sato S, Mizuno N, Kumasaka T, Fujita M. Self-assembly of tetravalent Goldberg polyhedra from 144 small components. Nature. 2016;540(7634):563-566. doi:10.1038/nature20771
7. Furukawa H, Cordova KE, O'Keeffe M, Yaghi OM. The Chemistry and Applications of Metal-Organic Frameworks. Science (80-). 2013;341(6149):1230444. doi:10.1126/science.1230444
8. Cook TR, Zheng Y-R, Stang PJ. Metal-organic frameworks and self-assembled supramolecular coordination complexes: comparing and contrasting the design, synthesis, and functionality of metal-organic materials. Chem Rev. 2013;113(1):734-777. doi:10.1021/cr3002824
9. Tranchemontagne DJ, Mendoza-Cortés JL, O'Keeffe M, Yaghi OM. Secondary building units, nets and bonding in the chemistry of metal-organic frameworks. Chem Soc Rev. 2009;38(5):1257-1283. doi:10.1039/b817735j
10. Jankolovits J, Andolina CM, Kampf JW, Raymond KN, Pecoraro VL. Assembly of Near-Infrared Luminescent Lanthanide Host(Host-Guest) Complexes With a Metallacrown Sandwich Motif. Angew Chemie Int Ed. 2011;50(41):9660-9664. doi:10.1002/anie.201103851
11. Nguyen TN, Chow CY, Eliseeva S V., et al. One-Step Assembly of Visible and Near-Infrared Emitting Metallacrown Dimers Using a Bifunctional Linker. Chem - A Eur J. 2018;24(5):1031-1035. doi:10.1002/chem.201703911
12. Martinić I, Eliseeva S V, Nguyen TN, Pecoraro VL, Petoud S. Near-Infrared Optical Imaging of Necrotic Cells by Photostable Lanthanide-Based Metallacrowns. J Am Chem Soc. 2017;139(25):8388-8391. doi:10.1021/jacs.7b01587
13. Trivedi ER, Eliseeva S V., Jankolovits J, Olmstead MM, Petoud S, Pecoraro VL. Highly Emitting Near-Infrared Lanthanide "Encapsulated Sandwich" Metallacrown Complexes with Excitation Shifted Toward Lower Energy. J Am Chem Soc. 2014;136(4):1526-1534. doi:10.1021/ja4113337

14. Chow CYCY, Eliseeva SVS V, Trivedi ERER, et al. Ga3+/Ln3+Metallacrowns: A Promising Family of Highly Luminescent Lanthanide Complexes That Covers Visible and Near-Infrared Domains. J Am Chem Soc. 2016;138(15):5100-5109. doi:10.1021/jacs.6b00984
15. Boron TT, Kampf JW, Pecoraro VL. A Mixed 3d–4f 14-Metallacrown-5 Complex That Displays Slow Magnetic Relaxation through Geometric Control of Magnetoanisotropy. Inorg Chem. 2010;49(20):9104-9106. doi:10.1021/ic101121d
16. Deb A, Boron TT, Itou M, et al. Understanding Spin Structure in Metallacrown Single-Molecule Magnets using Magnetic Compton Scattering. J Am Chem Soc. 2014;136(13):4889-4892. doi:10.1021/ja501452w
17. Atzeri C, Marzaroli V, Quaretti M, et al. Elucidation of 1 H NMR Paramagnetic Features of Heterotrimetallic Lanthanide(III)/Manganese(III) 12-MC-4 Complexes. Inorg Chem. 2017;56(14):8257-8269. doi:10.1021/acs.inorgchem.7b00970
18. Pavlyukh Y, Rentschler E, Elmers HJ, Hübner W, Lefkidis G. Magnetism of metallacrown single-molecule magnets: From a simplest model to realistic systems. Phys Rev B. 2018;97(21):214408. doi:10.1103/PhysRevB.97.214408
19. Dendrinou-Samara C, Alexiou M, Zaleski CM, et al. Synthesis and Magnetic Properties of a Metallacryptate that Behaves as a Single-Molecule Magnet. Angew Chemie Int Ed. 2003;42(32):3763-3766. doi:10.1002/anie.200351246
20. Zaleski CM, Tricard S, Depperman EC, et al. Single Molecule Magnet Behavior of a Pentanuclear Mn-Based Metallacrown Complex: Solid State and Solution Magnetic Studies. Inorg Chem. 2011;50(22):11348-11352. doi:10.1021/ic2008792
21. Zaleski CM, Depperman EC, Kampf JW, Kirk ML, Pecoraro VL. Synthesis, Structure, and Magnetic Properties of a Large Lanthanide–Transition-Metal Single-Molecule Magnet. Angew Chemie Int Ed. 2004;43(30):3912-3914. doi:10.1002/anie.200454013
22. Zaleski CM, Kampf JW, Mallah T, Kirk ML, Pecoraro VL. Assessing the Slow Magnetic Relaxation Behavior of LnIII4MnIII6 Metallacrowns. Inorg Chem (Washington, DC, United States). 2007;46(6):1954-1956.
23. Boron TT, Lutter JC, Daly CI, et al. The Nature of the Bridging Anion Controls the Single-Molecule Magnetic Properties of DyX 4 M 12-Metallacrown-4 Complexes. Inorg Chem. 2016;55(20):10597-10607. doi:10.1021/acs.inorgchem.6b01832
24. Chow CY, Bolvin H, Campbell VE, et al. Assessing the exchange coupling in binuclear lanthanide(III) complexes and the slow relaxation of the magnetization in the antiferromagnetically coupled Dy2 derivative. Chem Sci. 2015:4148-4159. doi:10.1039/C5SC01029B
25. Zaleski CM, Depperman EC, Kampf JW, Kirk ML, Pecoraro VL. Using LnIII[15-MCCuII(N)(S)-pheHA-5]3+ complexes To construct chiral single-molecule magnets and chains of single-molecule magnets. Inorg Chem. 2006;45(25):10022-10024.

26. Stemmler AJ, Kampf JW, Kirk ML, Atasi BH, Pecoraro VL. The Preparation, Characterization, and Magnetism of Copper 15-Metallacrown-5 Lanthanide Complexes. Inorg Chem. 1999;38(12):2807-2817. doi:10.1021/ic9800233
27. Chow CY, Guillot R, Rivière E, Kampf JW, Mallah T, Pecoraro VL. Synthesis and Magnetic Characterization of Fe(III)-Based 9-Metallacrown-3 Complexes Which Exhibit Magnetorefrigerant Properties. Inorg Chem. 2016;55(20):10238-10247. doi:10.1021/acs.inorgchem.6b01404
28. Lim CS, Tegoni M, Jakusch T, Kampf JW, Pecoraro VL. Clarifying the mechanism of cation exchange in Ca(II)[15-MCCu(II)Ligand-5] complexes. Inorg Chem. 2012;51(21):11533-11540. doi:10.1021/ic3013798
29. Dallavalle F, Remelli M, Sansone F, Bacco D, Tegoni M. Thermodynamics of self-assembly of copper(II) 15-metallacrown-5 of Eu(III) or Gd(III) with (S)-alpha-alaninehydroxamic acid in aqueous solution. Inorg Chem. 2010;49(4):1761-1772. doi:10.1021/ic902146d
30. Tegoni M, Furlotti M, Tropiano M, Lim CS, Pecoraro VL. Thermodynamics of core metal replacement and self-assembly of Ca(2+) 15-metallacrown-5. Inorg Chem. 2010;49(11):5190-5201. doi:10.1021/ic100315u
31. Grant JT, Jankolovits J, Pecoraro VL. Enhanced guest affinity and enantioselectivity through variation of the Gd3+ [15-metallacrown-5] side chain. Inorg Chem. 2012;51(15):8034-8041. doi:10.1021/ic300110g
32. Jankolovits J, Kampf JW, Maldonado S, Pecoraro VL. Voltammetric characterization of redox-inactive guest binding to Ln(III)[15-Metallacrown-5] hosts based on competition with a redox probe. Chem Eur J. 2010;16(23):6786-6796. doi:10.1002/chem.200903015
33. Jankolovits J, Lim C-SS, Mezei G, Kampf JW, Pecoraro VL. Influencing the size and anion selectivity of dimeric Ln(3+)[15-metallacrown-5] compartments through systematic variation of the host side chains and central metal. Inorg Chem. 2012;51(8):4527-4538. doi:10.1021/ic202347j
34. Jankolovits J, Cutland Van-Noord AD, Kampf JW, Pecoraro VL. Selective anion encapsulation in solid-state Ln(iii)[15-metallacrown-5]3+ compartments through secondary sphere interactions. Dalt Trans. 2013;42(27):9803-9808. doi:10.1039/c3dt50535a
35. Lim C-S, Jankolovits J, Zhao P, Kampf JW, Pecoraro VL. Gd(III)[15-metallacrown-5] recognition of chiral α-amino acid analogues. Inorg Chem. 2011;50(11):4832-4841. doi:10.1021/ic102579t
36. Tegoni M, Tropiano M, Marchiò L. Thermodynamics of binding of carboxylates to amphiphilic Eu(3+)/Cu(2+) metallacrown. Dalton Trans. September 2009:6705-6708. doi:10.1039/b911512a
37. Atzeri C, Marchiò L, Chow CY, Kampf JW, Pecoraro VL, Tegoni M. Design of 2D Porous Coordination Polymers Based on Metallacrown Units. Chem - A Eur J. 2016;22(19). doi:10.1002/chem.201600562

38. Ostrowska M, Fritsky IO, Pavlishchuk A V. Metallacrown-based compounds: Applications in catalysis, luminescence, molecular magnetism, and adsorption. Coord Chem Rev. 2016;327:304-332. doi:10.1016/j.ccr.2016.04.017
39. Pavlishchuk AV, Satska Y., Kolotilov SV, Fritsky I. Coordination Polymers and Oligonuclear Systems Based on Oximate or Hydroxamate Building Blocks: Magnetic and Sorption Properties. Curr Inorg Chem. 2015;5(1):5-25. doi:10.2174/1877944105666150417230637
40. Lamberts K, Tegoni M, Jiang X, Kou H-Z, Englert U. Silver complexation by metallacryptates. Dalt Trans. 2016;45(1):284-295. doi:10.1039/c5dt03749b
41. Chow CY, Trivedi ER, Pecoraro V, Zaleski CM. Heterometallic Mixed 3d-4f Metallacrowns: Structural Versatility, Luminescence, and Molecular Magnetism. Comments Inorg Chem. 2015;35(4):214-253. doi:10.1080/02603594.2014.981811
42. Happ P, Plenk C, Rentschler E. 12-MC-4 metallacrowns as versatile tools for SMM research. Coord Chem Rev. 2015;289-290(1):238-260. doi:10.1016/j.ccr.2014.11.012
43. Tegoni M, Remelli M. Metallacrowns of copper(II) and aminohydroxamates: Thermodynamics of self assembly and host–guest equilibria. Coord Chem Rev. 2012;256(1-2):289-315. doi:10.1016/j.ccr.2011.06.007
44. Mezei G, Zaleski CM, Pecoraro VL. Structural and Functional Evolution of Metallacrowns. Chem Rev. 2007;107(11):4933-5003. doi:10.1021/cr078200h
45. Bodwin JJ, Cutland AD, Malkani RG, Pecoraro VL. The development of chiral metallacrowns into anion recognition agents and porous materials. Coord Chem Rev. 2001;216-217:489-512. doi:10.1016/S0010-8545(00)00396-9
46. Eddaoudi M, Moler DB, Li H, et al. Modular chemistry: Secondary building units as a basis for the design of highly porous and robust metal-organic carboxylate frameworks. Acc Chem Res. 2001;34(4):319-330. doi:10.1021/ar000034b
47. Wang K, Zou H-H, Chen Z-L, Zhang Z, Sun W-Y, Liang F-P. A series of 3D metal organic frameworks based on [24-MC-6] metallacrown clusters: structure, magnetic and luminescence properties. Dalton Trans. 2014;43(34):12989-12995. doi:10.1039/c4dt01593b
48. Pecoraro VL, Bodwin JJ, Cutland AD. Formation of Chiral Solids via a Molecular Building Block Approach. J Solid State Chem. 2000;152(1):68-77. doi:10.1006/jssc.2000.8670
49. Mengle KA, Longenecker EJ, Zeller M, Zaleski CM. One-Dimensional Coordination Polymers of 12-Metallacrown-4 Complexes: {Na2(L)2[12-$${\rm{M}}{{\rm{C}}_{{\rm{M}}{{\rm{n}}^{{\rm{III}}}}{\rm{(N)shi}}}}$$ M C M n III (N) shi -4]} n , where L is Either –O2CCH2CH3 or –O2CCH2CH2CH3. J Chem Crystallogr. 2015;45(1):36-43. doi:10.1007/s10870-014-0560-0
50. Gumienna-Kontecka E, Golenya IA, Dudarenko NM, et al. A new Cu(II) [12]metallocrown-4 pentanuclear complex based on a Cu(II)-malonomonohydroxamic acid unit. New J Chem. 2007;31(10):1798-1805. doi:10.1039/b701600j

51. Govor E V., Lysenko AB, Chernega AN, et al. Copper(II)–lanthanide(III) 15-metallacrown-5 complexes based on pyrazinohydroxamic acid as new multiple-binding pentagonal platforms with Lewis amphoteric nature. Polyhedron. 2008;27(11):2349-2356. doi:10.1016/j.poly.2008.04.042
52. McDonald C, Whyte T, Taylor SM, et al. Progressive decoration of pentanuclear Cu(ii) 12-metallacrown-4 nodes towards targeted 1- and 2D extended networks. CrystEngComm. 2013;15(34):6672. doi:10.1039/c3ce40859k
53. Lago AB, Pasán J, Cañadillas-Delgado L, et al. A three-dimensional copper(ii) 12-metallacrown-4 complex with malonomonohydroxamic acid (H3mmh) as a ligand. New J Chem. 2011;35(9):1817. doi:10.1039/c1nj20184k
54. Pavlishchuk A V., Kolotilov S V., Zeller M, et al. Magnetic and Sorption Properties of Supramolecular Systems Based on Pentanuclear Copper(II) 12-Metallacrown-4 Complexes and Isomeric Phthalates: Structural Modeling of the Different Stages of Alcohol Sorption. Eur J Inorg Chem. 2011;2011(31):4826-4836. doi:10.1002/ejic.201100790
55. Pavlishchuk A V, Kolotilov S V, Zeller M, et al. A Triple-Decker Heptadecanuclear (CuII)15(CrIII)2 Complex Assembled from Pentanuclear Metallacrowns. Eur J Inorg Chem. 2010;2010(30):4851-4858.
56. Pavlishchuk A V., Kolotilov S V., Zeller M, et al. High Nuclearity Assemblies and One-Dimensional (1D) Coordination Polymers Based on Lanthanide–Copper 15-Metallacrown-5 Complexes (Ln III = Pr, Nd, Sm, Eu). Inorg Chem. 2017;56(21):13152-13165. doi:10.1021/acs.inorgchem.7b01944
57. Pavlishchuk A V., Kolotilov S V., Zeller M, et al. Supramolecular Maleate Adducts of Copper(II) 12-Metallacrown-4: Magnetism, EPR, and Alcohol Sorption Properties. Eur J Inorg Chem. 2017;2017(41):4866-4878. doi:10.1002/ejic.201700976
58. Pavlishchuk A V., Kolotilov S V., Zeller M, Thompson LK, Addison AW. Formation of coordination polymers or discrete adducts via reactions of gadolinium(III)-copper(II) 15-metallacrown-5 complexes with polycarboxylates: Synthesis, structures and magnetic properties. Inorg Chem. 2014;53(3):1320-1330. doi:10.1021/ic401928m
59. Bodwin JJ, Pecoraro VL. Preparation of a chiral, 2-dimensional network containing metallacrown and copper benzoate building blocks. Inorg Chem. 2000;39(16):3434-3435. doi:10.1021/ic000562j
60. Lim C-S, Jankolovits J, Kampf JW, Pecoraro VL. Chiral Metallacrown Supramolecular Compartments that Template Nanochannels: Self-Assembly and Guest Absorption. Chem - An Asian J. 2010;5(1):46-49. doi:10.1002/asia.200900612
61. Cutland-Van Noord AD, Kampf JW, Pecoraro VL. Preparation of resolved fourfold symmetric amphiphilic helices using chiral metallacrown building blocks. Angew Chem Int Ed Engl. 2002;41(24):4667-4670. doi:10.1002/anie.200290010
62. Audhya A, Bhattacharya K, Maity M, Chaudhury M. Building Metallacrown Topology around a Discrete [M 3 (μ 3-O)] (M = Ni(II) and Pd(II)) Core Using Oximato Oxygen Linkers: Synthesis,

Structures, and Spectroscopic Characterization of a New Family of Compounds with an Inverse-9-MC-3 Motif. 2010. doi:10.1021/ic100179q

63. Yang C-I, Wernsdorfer W, Cheng K-H, Nakano M, Lee G-H, Tsai H-L. A [Mn III 3 O] 7+ Single-Molecule Magnet: the Anisotropy Barrier Enhanced by Structural Distortion. Inorg Chem. 2008;47(22):10184-10186. doi:10.1021/ic8012238
64. Pt Antitumor Complexes. Inorg Chem. 1992;31(4).
65. McCusker JK, Jang HG, Wang S, Christou G, Hendrickson DN. Ground-state variability in .mu.3-oxide trinuclear mixed-valence manganese complexes: spin frustration. Inorg Chem. 1992;31(10):1874-1880. doi:10.1021/ic00036a029
66. Brachvogel RC, Maid H, von Delius M. NMR Studies on Li+, Na+ and K+ complexes of orthoester cryptand 0-Me2-1.1.1. Int J Mol Sci. 2015;16(9):20641-20656. doi:10.3390/ijms160920641
67. Brachvogel R-C, Hampel F, Von Delius M. ARTICLE Self-assembly of dynamic orthoester cryptates. Nat Commun. 2015;6. doi:10.1038/ncomms8129
68. Low H, Mena-Osteritz E, von Delius M. Self-assembled orthoester cryptands: orthoester scope, post-functionalization, kinetic locking and tunable degradation kinetics. Chem Sci. 2018;9(21):4785-4793. doi:10.1039/C8SC01750F
69. Dietrich B. Cryptands. In: G.W. Gokel, ed. Comprehensive Supramolecular Chemistry. 1st ed. Oxford: Elsevier; 1996:153–211.
70. Lehn J -M. Supramolecular Chemistry—Scope and Perspectives Molecules, Supermolecules, and Molecular Devices (Nobel Lecture). Angew Chemie Int Ed English. 1988;27(1):89-112. doi:10.1002/anie.198800891
71. Bruker. SMART (control) and SAINT (integration) software. 1994.
72. Lausi A, Polentarutti M, Onesti S, et al. Status of the crystallography beamlines at Elettra Status of the crystallography beamlines at Elettra ⋆. Eur Phys J Plus. 2015;130:4-7. doi:10.1140/epjp/i2015-15043-3
73. Agilent. CrysAlis PRO. 2014.
74. Sheldrick GM. Area-Detector Absorption Correction. 1996.
75. Sheldrick GM. SHELXT – Integrated space-group and crystal-structure determination. Acta Crystallogr Sect A Found Adv. 2015;71(1):3-8. doi:10.1107/S2053273314026370
76. Sheldrick GM. Crystal structure refinement with SHELXL. Acta Crystallogr Sect C Struct Chem. 2015;71(1):3-8. doi:10.1107/S2053229614024218
77. Macrae CF, Bruno IJ, Chisholm JA, et al. Mercury CSD 2.0 – new features for the visualization and investigation of crystal structures. J Appl Crystallogr. 2008;41(2):466-470. doi:10.1107/S0021889807067908
78. Tegoni M, Ferretti L, Sansone F, Remelli M, Bertolasi V, Dallavalle F. Synthesis, solution thermodynamics, and X-ray study of CuII [12]metallacrown-4 with GABA hydroxamic acid: an

unprecedented crystal structure of a [12]MC-4 with a gamma-aminohydroxamate. Chem Eur J. 2007;13(4):1300-1308. doi:10.1002/chem.200601035

79. Atzeri C. Supramolecular coordination complexes as building blocks for porous and magnetic materials. 2016.

80. Lah MS, Pecoraro VL. Isolation and characterization of {MnII[MnIII(salicylhydroximate)]4(acetate)2(DMF)6}.cntdot.2DMF: an inorganic analog of M2+(12-crown-4). J Am Chem Soc. 1989;111(18):7258-7259. doi:10.1021/ja00200a054

Chapter 3

SUPPLEMENTARY MATERIAL

Figure S4

^{1}H NMR of N-*t*-butyloxycarbonyl-4-aminosalicylic acid (**2**) collected in DMSO-d_6*

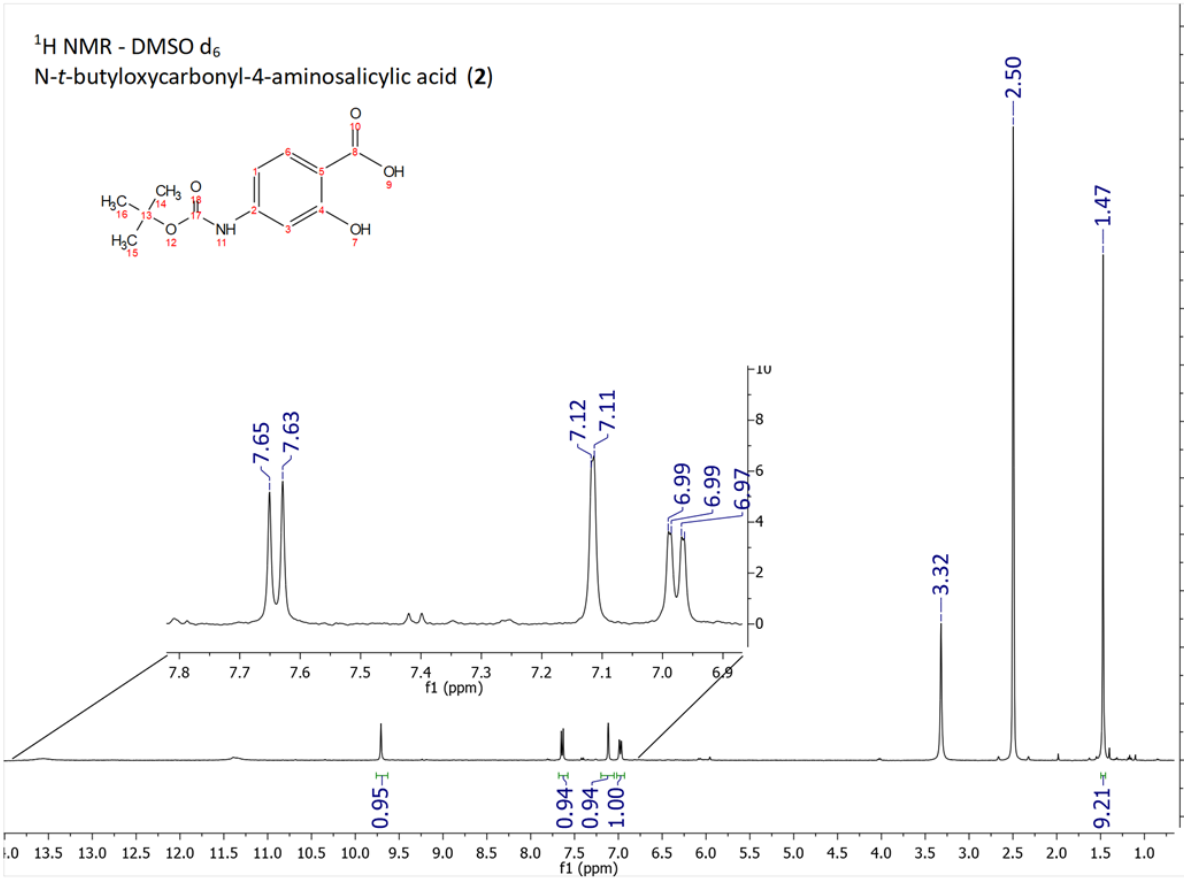

.

Figure S5

^{1}H NMR of N-t-butyloxycarbonyl-4-aminosalicyl-O-benzylhydroxamate (**3**) collected in DMSO-d_6. The * symbol shows picks of residual solvents (Ethyl Acetate, DMF).

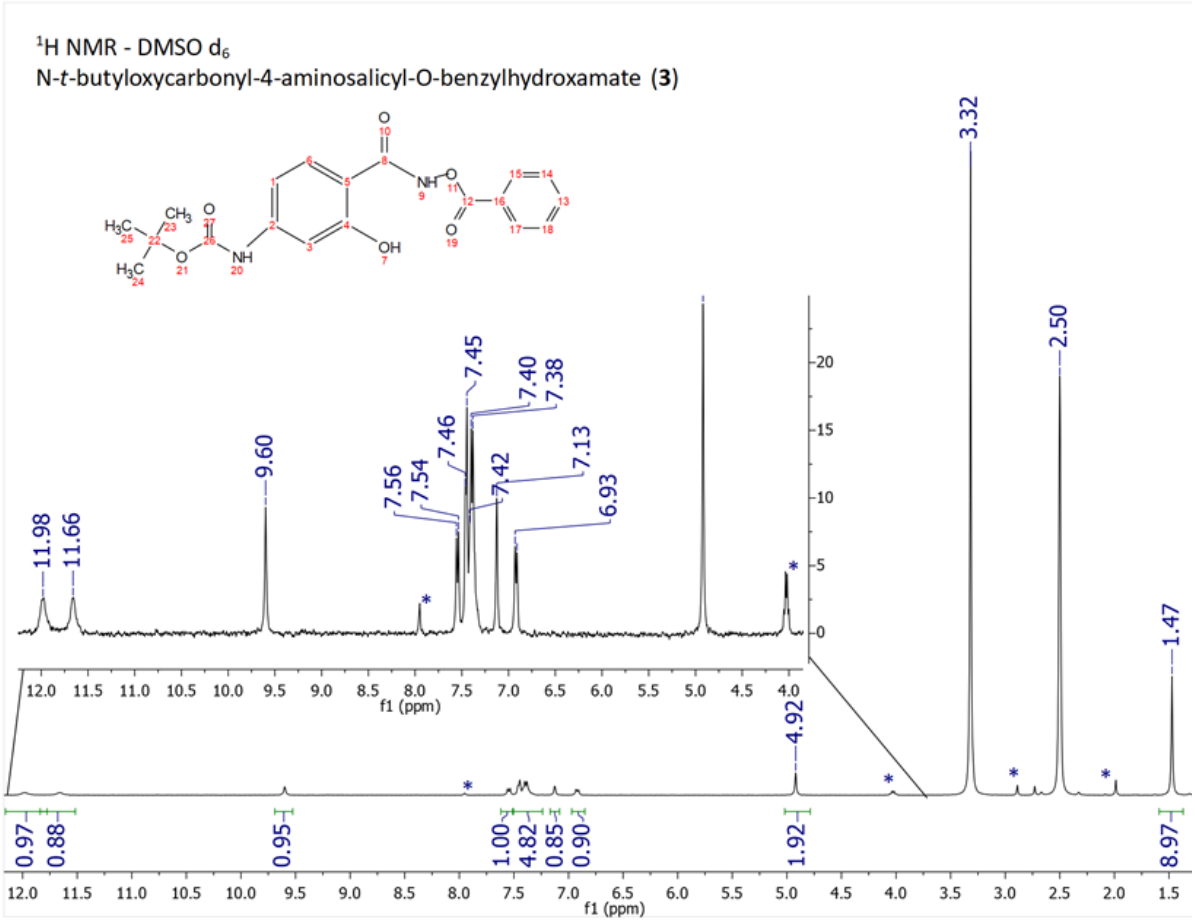

Figure S6

^{1}H NMR of 4-aminosalicyl-*O*-benzylhydroxamate (**4**) collected in DMSO-d_6, the spectra show the presence of water, which result in the absence of acids protons signals.

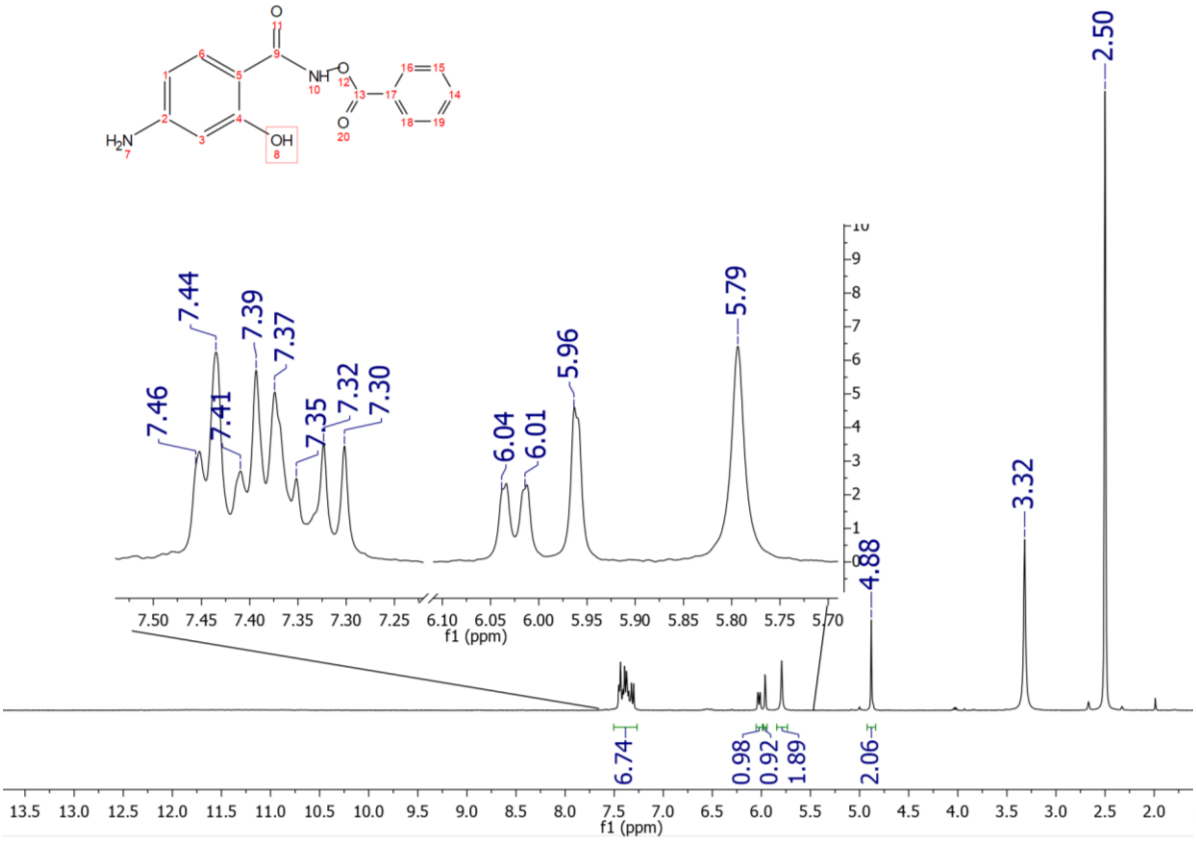

Figure S7

^{1}H NMR of 4-aminosalicylhydroxamic acid (**H_3p-aShi, 5**) collected in DMSO-d_6, the spectra show the presence of a large amount of water, which result in the absence of acids H^+ signals. The presence of residual solvents signals are highlighted by * sign.

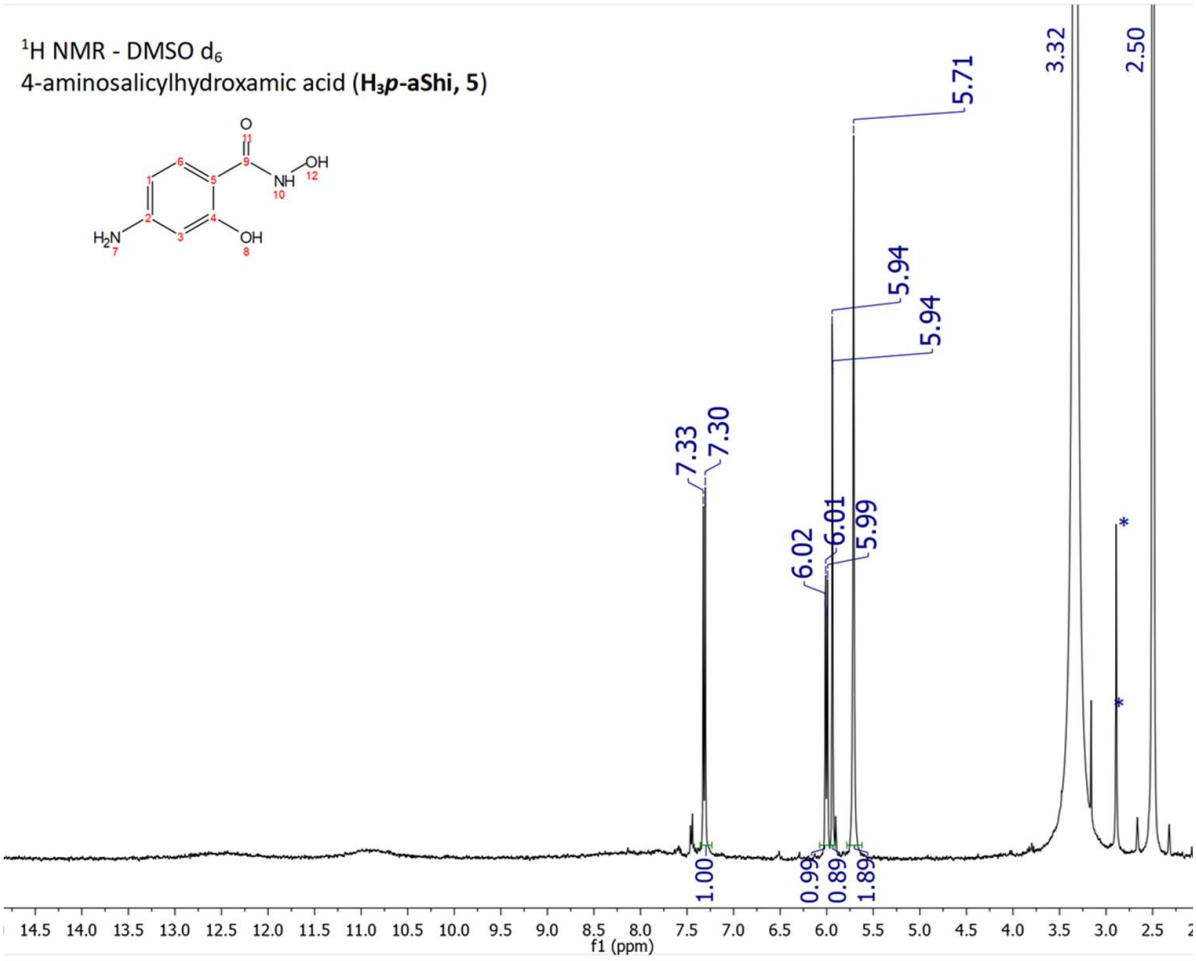

Figure S8

The novel Mn^{II}[12-$MC_{Mn^{III},(O)H3p\text{-}aShi\text{-}3H}$-4]$(OAc)_2$ species.

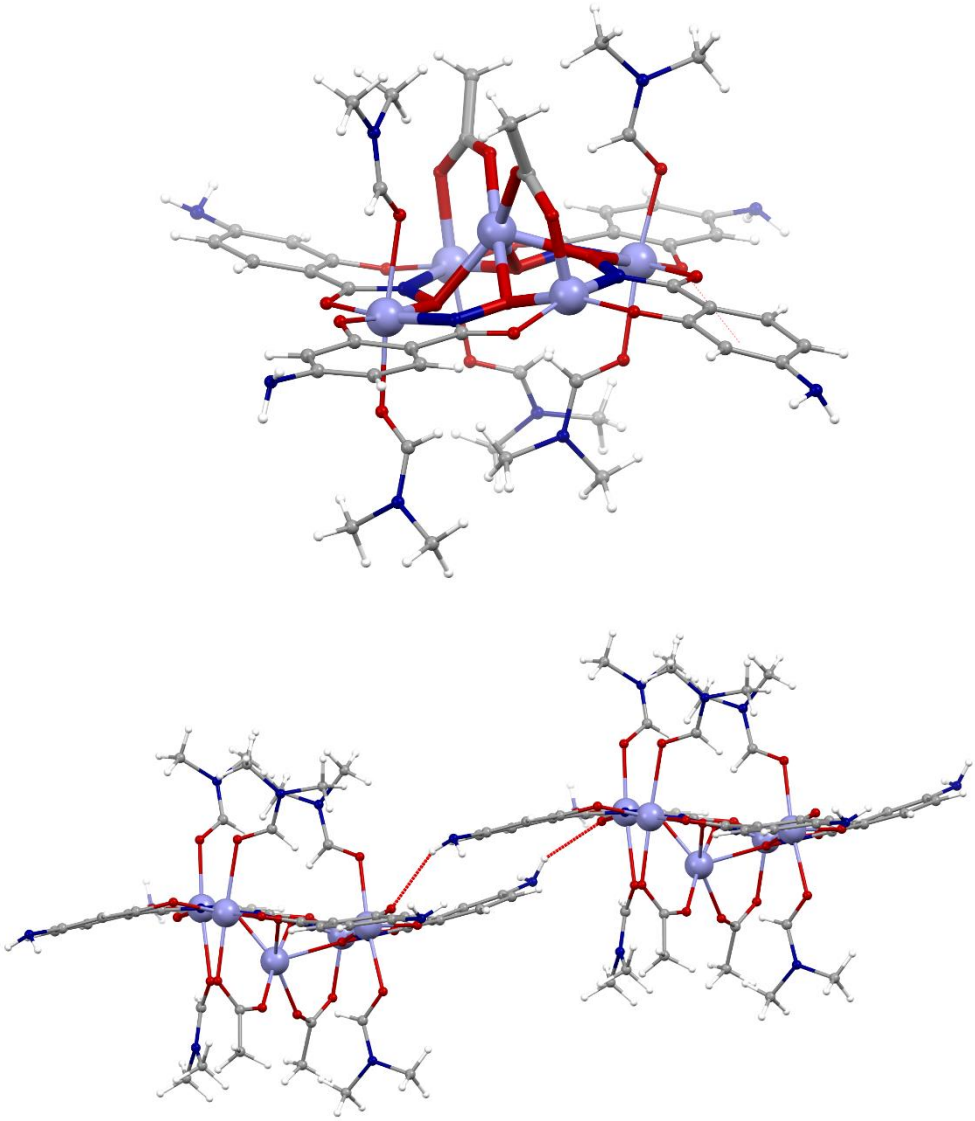

Structure of the Mn^{II}[12-$MC_{Mn^{III},(O)H3p\text{-}aShi\text{-}3H}$-4]$(OAc)_2$ species, that is often obtained instead of the Mn_{11}p-$aShi_6$ coordination polymer. This complex is isostructural with the previously reported analogous Mn^{II}[12-$MC_{Mn^{III},(O)H3Shi\text{-}3H}$-4]$(OAc)_2$.[1] The presence of the -NH_2 function, which lead to the formation of a porous and 3D network in case of the Mn_{11} cage, here form hydrogen bonds between neighbouring 12-MC-4 units.

Table S8

Summary of X-ray crystallographic data for $Mn^{II}[12\text{-}MC_{Mn^{III},\ p\text{-}aShi}\text{-}4](OAc)_2$

Empirical formula	$C_{53}H_{75}Mn_5N_{15}O_{23}$
Formula weight/gmol^{-1}	1564.98
Temperature/K	100.0
Crystal system	monoclinic
Space group	$P2_1$
a/Å	13.8033(5)
b/Å	16.9205(7)
c/Å	14.2509(6)
α/°	90
β/°	93.016(4)
γ/°	90
Volume/Å^3	3323.8(2)
Z	2
ρ_{calc}g/cm^3	1.564
μ/mm^{-1}	0.973
F(000)	1614.0
Crystal size/mm^3	0.1 × 0.1 × 0.05
Radiation/ Å	synchrotron (λ = 0.700)
2θ range for data collection/°	3.684 to 55.632
No.of rflcn/unique	50672/16415 [R_{int} = 0.1258]
Data/restraints/parameters	16415/1/874
Goodness-of-fit on F^2	1.029
R_1 [I>=2σ (I)]	R_1 = 0.0677
wR_2 [I>=2σ (I)]	wR_2 = 0.1499
Resid. Dens / e$^-$ Å^{-3}	1.12/-0.57
Flack parameter	0.35(3)

Table S9 Summary of X-Ray crystallographic data for 6, 7, 8, 9 and 10.

	6	7	8*	9	10
Empirical formula	$C_{78}H_{106.5}Mn_{11}N_{12}Na_4O_{52.75}$	$C_{75}H_{92}K_4Mn_{11}N_{11}O_{49}$	$C_{78}H_{93}Cs_4Mn_{11}N_{12}O_{54}$	$C_{82.5}H_{121.5}Mn_{11}N_{19.5}Na_{3.5}O_{53.5}$	$C_{78}H_{66}Mn_{11}N_{12}O_{37}$
Formula weight/gmol^{-1}	2752.55	2692.33	3198.62	2927.29	2367.72
Temperature/K	293	200	100	85	85
Crystal system	cubic	orthorhombic	triclinic	trigonal	hexagonal
Space group	I-43d	Pbcn	P-1	P-3c1	$P6_3/m$
a/Å	35.533(2)	17.2501(7)	17.475(2)	24.6802(2)	24.3899(6)
b/Å	35.533(2)	26.5826(9)	20.628(2)	24.6802(2)	24.3899(6)
c/Å	35.533(2)	22.9673(9)	20.6956(19)	31.1791(4)	17.5667(7)
α/°	90	90	104.638(9)	90	90
β/°	90	90	112.503(10)	90	90
γ/°	90	90	98.360(10)	120	120
Volume/Å^3	44864(8)	10531.7(7)	6419.0(13)	16447.2(3)	9049.8(6)
Z	16	4	2	4	2
ρ_{calc} g/cm^3	1.630	1.698	1.655	1.182	0.869
μ/mm^{-1}	1.305	1.525	2.163	7.338	6.431
F(000)	22392.0	5448.0	3144	5978.0	2378.0
Crystal size/mm^3	0.34 × 0.3 × 0.3	0.22 × 0.22 × 0.07	0.15 × 0.17 × 0.13	0.18 × 0.17 × 0.12	0.2 × 0.14 × 0.14
Radiation/ Å	MoKα (λ = 0.71073)	MoKα (λ = 0.71073)	syncrotron	CuKα (λ = 1.54184)	CuKα (λ = 1.54184)
2Θ range for data collection/°	2.808 to 51.338	5.168 to 51.522	3.276 to 49.248	4.134 to 139.552	6.544 to 138.574
No.of rflcn/unique	185099/7101 [R_{int} = 0.1184]	72165/10027 [R_{int} = 0.0788]	74648/21397 [Rint = 0.2173]	247003/10250 [R_{int} = 0.1198]	136453/5822 [R_{int} = 0.1314]
Data/restraints/parameters	7101/12/452	10027/1/685	21397/6/734	10250/87/611	5822/6/226
Goodness-of-fit on F^2	1.048	1.170	1.292	1.008	1.027
R_1 [I>=2σ (I)]	0.0432	0.0716	0.1765	0.0443	0.0733
wR_2 [I>=2σ (I)]	0.1113	0.1804	0.4175	0.1233	0.2029
Resid. Dens / e$^-$ Å^{-3}	0.59/-0.40	0.78/-0.76	3.81/-2.23	1.08/-0.47	0.85/-0.41
Flack parameter	0.005(8)				

*preliminary data: crystals of 8 are deliquescent, diffraction has low intensity

Conclusions

"Non esiste l' **IDEA** *e sorrido a chi considera*

l'Infinito di Leopardi, un'idea geniale.

Quello che rende un'opera,

un'opera d'arte,

sono studio, progettazione e pianificazione."

W. Xerra

Coming to the conclusions, after their discovery in 1989, metallacrowns have been studied and developed and an ever-growing number of structures, architectures, properties and general features continue to be discovered and investigated.

Despite those people that over the years could not believe much in the wide possibilities provided by this class of compounds, I found interesting and fascinating, working within this field of research, having a great opportunity to keep my creativity active and productive.

The numbers of trials, errors, serendipitous discovery and promising results, which arises from the past three years of research have produced a huge numbers of new synthetic strategies, characterization approaches, crystal structures, opening many possible routes to be pursued.

This is the substrate, from which arose the not ordinary idea to entitle the present dissertation, "*Thriving metallacrowns* …."

The experimental data were divided in two main characters, concerning:

I) the extrapolation of a considerable number of information upon the molecular structure, the behavior, features and intrinsic properties of metallacrown complexes in solution, through the cheap, fast and easy monodimensional ^{1}H NMR characterization technique.

II) the exploration of the possible strategies, which can be followed, to prepare solid state assemblies of metallacrowns whit specific characteristics, that could be predicted, to some extent.

Two series of heterotrimetallic and paramagnetic metallacrowns were studied, through ^{1}H NMR technique. The ^{1}H NMR spectra of twelve $Ln^{III}Na^{I}(OAc)_4[12\text{-}MC_{Mn^{III}(O)H3Shi\text{-}3H}\text{-}4]$ complexes (Ln^{III}-MC), and thirteen $Ln^{III}Na^{I}(OBz)_4[12\text{-}MC_{Ga^{III}(O)H3Shi\text{-}3H}\text{-}4]$ complexes (Ln = Pr-Lu, except Pm,

and Y) were collected and the experimental chemical shifts and integrals were analysed and discussed.

The YMn_4, YGa_4-2, $LaGa_4$-2 and $LuGa_4$-2, are diamagnetic compounds: the Y-derivatives have been used as diamagnetic reference, while the Lu derivative have been considered as an additional proof of the isostructural nature of the analysed compounds upon dissolution. Indeed, the ^1H NMR pattern of Y and Lu match perfectly.

Overall the other derivatives contain paramagnetic centres. The paramagnetic nature of the lanthanide center did not prevent the possibility to perform high resolution NMR, indeed, narrow and well resolved resonances were found for both the 12-MC-4 series.

In case of the $LnMn_4$ series, not only the encapsulated lanthanide gives rise to a paramagnetic behaviour, but a second paramagnetic system is in charge to the manganese(III). It was found that the main contribution to the chemical shift is determined in this case by the $[Mn]_4$ paramagnetic system, while the Ln^{III} induces only a second order perturbation.

Conversely, the chemical shift found through the analysis of the $LnGa_4$-2 series, is dominated by the lanthanides induced shift, reported as $LIS_{Ln.}$

The LIS_{Ln} values fot both the Mn and Ga derivatives of compound were calculated and then treated following the "*all lanthanides*" method. In both the series, the *plot-I* shows that the Fermi contact contribution to the chemical shift is not negligible for the lighter lanthanides. Indeed only the heavier lanthanide derivatives were completely analysed following the instructions of the "*all lanthanides*" method.

The "*all lanthanides*" calculations provided both accurate values of the δ^{FC}_{Ln} and δ^{PC}_{Ln} values for the Gd-$YbMn_4$ series and for the Tb-$YbGa_4$-2 one, thanks to the fact that both parameters were extrapolated without any *a-priori* assumption.

The results reported in the present dissertation constitutes an experimental confirmation on the stability of the MC-scaffold in solution and on the retention of the molecular structure after dissolution.

The presence of one set of resonances on the collected spectra, gives rise to the hypothesis, that minor rearrangements in the structure take place, when the complexes dissolve. Indeed, the crystal structures of such compounds do not exhibit a proper C_4 axis, whose evidence in the ^1H NMR spectra suggests, that in solution these systems average the small distortions and turn into a 4-fold symmetrical molecule.

No information is provided on the sodium ion destiny after dissolution: the investigations of the Na behavior in solution represents one of the next steps in evolving the characterization of these systems.

The availability of the crystal structures of much of the analized compounds, allowed to unambiguously assign the resonances of the Shi^{3-} protons both in case of $LnMn_4$ and $LnGa_4$-2 compounds, through the correlation of the “all lanthanides” M(i) parameters with the crystal structure geometrical terms ($G(i)^{XRD}$).

These results are unprecedented in the field of the characterization of metallacrowns and may open the future use of paramagnetic NMR methods for structural determination of these species in solution.

Moreover the presence of the $[Mn]_4$ paramagnetic system enhanced the relaxation time of the $GdMn_4$ derivative, allowing to observe the ^1H NMR signals. This is, to the best of our knowledge, the first example in literature, of the ^1H NMR characterization of small Gd derivatives.

The investigation of the magnetic properties of these compounds and the possible use of such features to develop new materials or probes based on metallacrowns constitute another possible future development of the present study.

As far as it concerns the construction of metallacrowns-based three-dimensional frameworks, the present dissertation contains unprecedent results. Indeed, if the first bidimensional metallacrown framework has been designed in 2001 by J. J. Bodwin, et al (Coord. Chem. ev., 2001, 216-217, 489–512) and was experimentally found by Atzeri et al in 2016 (Eur J. 2016; *22*(19) 6482-6486), to the best of our knowledge, no one three-dimensional MOF-like architecture has ever been found, showing the metallacrown topology within the Secondary Building Unit. Hence, the Mn_{11}*p*-pyShi_6 seems represent the first examples of a three-dimensional network, where the SBUs show the metallacrown topology and are characterized by three-dimensional endless channels, which corresponds to the 55% of empty volume, within the unit cell. This result was possible thanks to the design of the appropriate starting building blocks (i.e. metal ions, ligands and linkers).

Before the Mn_{11}*p*-pyShi_6 , four more metallacrown-based frameworks were found, having the same Mn_{11}-cages as node. The differentiation of these five networks is in charge on the periphery of the Mn_{11}-cage, which have been differently decorated. Three networks arose from the same ligand (i.e. salicylhydroxamate, shi^{3-}) and were differentiated by changing the size of the cationic linker (from Na^{I}, to K^{I} and Cs^{I}), which act as bridge between SBUs. The Na and K gave tightly packed materials, showing small interstitial cavities Whereas, the largest cationic linker (Cs^{I}) produced a 2D-networks. However, the most interesting results have been found through the functionalization of the ligand. Indeed, H_3*p*-aShi and H_3*p*-pyShi are two new derivatives of the salicylhydroxamic acid. They were designed and synthetized, by placing two

coordinative functions in para to the hydroxamic group. The first, *p*-aShi^{3-}, shows an amino hook and the second, *p*-pyShi^{3-}, a pyridyl one. Both these functionalizations were found capable to connect SBUs, forming respectively supramolecular and coordinative interactions. The first ligand formed a 3D architecture, which have monodimensional honeycomb-shaped channels, while *p*-pyShi^{3-}, as already said, allowed a break-through in the metallacrown solid-state chemistry, resulting in a MOF-like architecture, were only coordinative interactions are involved.

In addition, the Mn_{11}-polymetallic cluster, which act as SBU, may give rise to peculiar magnetic properties, since many examples of $[M_3(\mu_3\text{-}O)]^{n+}$ triangular units derivatives are found in literature as vehicle of magnetic features.

In the future it would be worth to determine the thermal stability profiles, the surface area and the magnetic properties of such compounds, considering that they seems promising for further applications as magnetic probes.

Vittoria Marzaroli

vittoria.marzaroli@gmail.com